MINISTÉRIO DA EDUCAÇÃO
UNIVERSIDADE FEDERAL DO RIO GRANDE DO SUL
PROGRAMA DE PÓS-GRADUAÇÃO EM ENGENHARIA MECÂNICA

NUMERICAL STUDY OF SOOT FORMATION IN LAMINAR ETHYLENE DIFFUSION FLAMES

por

Leonardo Zimmer

Tese para obtenção do Título de
Doutor em Engenharia

Porto Alegre, Dezembro de 2016

NUMERICAL STUDY OF SOOT FORMATION IN LAMINAR ETHYLENE DIFFUSION FLAMES

por

Leonardo Zimmer
Mestre em Engenharia Mecânica

Tese submetida ao Corpo Docente do Programa de Pós-Graduação em Engenharia Mecânica, PROMEC, da Escola de Engenharia da Universidade Federal do Rio Grande do Sul, como parte dos requisitos necessários para a obtenção do Título de

Doutor em Engenharia

Área de Concentração: Fenômenos de Transporte

Orientador: Prof. Dr. Fernando Marcelo Pereira

Aprovada por:

Prof. Dr. Guenther Carlos Krieger Filho .... PME / USP

Prof. Dr. Amir Antônio Martins Oliveira Filho .... MEC / UFSC

Prof. Dra. Thamy Cristina Hayashi .... DEMEC / UFRGS

Prof. Dr. Francis Henrique Ramos França .... PROMEC / UFRGS

Prof. Dr. Jackson Vassoler
Coordenador do PROMEC

Porto Alegre, 02, Dezembro de 2016

To my wife, Clarissa, and my son, Rafael

ACKNOWLEDGEMENT

My deepest thanks to my parents and my brother for their support, encouragement, and inspiration.

I am genuinely thankful to Professor Fernando Marcelo Pereira, my thesis supervisor, for his guidance, support, and trust, to my colleagues and friends from UFRGS, especially the ones at the Laboratory of Combustion (LC), GESTE, LETA and LabBeer.

I would like to express my sincere gratitude and appreciation to Professor Philip de Goey and Professor Jeroen van Oijen, from Eindhoven University of Technology (TU/e), for the opportunity to work with them and to learn so much from them. I also thank my colleagues and friends at TU/e.

Finally, I am very much thankful for the financial support of the Coordenação de Aperfeiçoamento de Pessoal de Nível Superior (CAPES) during my PhD thesis and also the Project No. BEX5381-13-4 that made possible the Sandwich Program in the Netherlands.

RESUMO

O objetivo desta tese é o estudo de formação de fuligem em chamas laminares de difusão. Para o modelo de formação de fuligem é escolhido um modelo semi-empírico de duas equações para prever a fração mássica de fuligem e o número de partículas de fuligem. O modelo descreve os processos de nucleação, de crescimento superficial e de oxidação das partículas. Para o modelo de radiação, a perda de calor por radiação térmica (gás e fuligem) é modelada considerando o modelo de gás cinza no limite de chama opticamente fina (OTA - *Optically Thin Approximation*). São avaliados diferentes modelos de cálculo das propriedades de transporte (detalhado e simplificado). Em relação à cinética química, tanto modelos detalhados quanto reduzidos são utilizados. No presente estudo, é explorada a técnica automática de redução conhecida como *Flamelet Generated Manifold* (FGM), sendo que esta técnica é capaz de resolver cinética química detalhada com tempos computacionais reduzidos. Para verificar o modelo de formação de fuligem foram realizados uma variedade de experimentos numéricos, desde chamas laminares unidimensionais adiabáticas de etileno em configuração tipo jatos opostos (*counterflow*) até chamas laminares bidimensionais com perda de calor de etileno em configuração tipo jato (*coflow*). Para testar a limitação do modelo os acoplamentos de massa e energia entre a fase sólida e a fase gasosa são investigados e quantificados para as chamas contra-corrente. Os resultados mostraram que os termos de radiação da fase gasosa e sólida são os termos de maior importancia para as chamas estudas. Os termos de acoplamento adicionais (massa e propriedade termodinâmicas) são geralmente termos de efeitos de segunda ordem, mas a importância destes termos aumenta conforme a quantidade de fuligem aumenta. Como uma recomendação geral o acoplamento com todos os termos deve ser levado em conta somente quando a fração mássica de fuligem, Y_S, for igual ou superior a 0.008. Na sequência a formação de fuligem foi estudada em chamas bi-dimensionais de etileno em configuração jato laminar usando cinética química detalhada e explorando os efeitos de diferentes modelos de cálculo de propriedades de transporte. Foi encontrado novamente que os termos de radiação da fase gasosa e sólida são os termos de maior importância e uma primeira aproximação para resolver a chama bidimensional de jato laminar de etileno pode ser feita usando o modelo de transporte simplificado. Finalmente, o modelo de fuligem é implementado com a técnica de redução FGM e diferentes formas de armazenar as informações sobre o modelo de fuligem nas tabelas termoquímicas (*manifold*) são testadas. A melhor opção testada neste trabalho é a de resolver todos os *flamelets* com as fases sólida e gasosa acopladas e armazenar as taxas de reação da fuligem por área de partícula no *manifold*. Nas simulações bidimensionais estas taxas são então recuperadas para resolver as equações adicionais de formação de fuligem. Os resultados mostraram uma boa concordância qualitativa entre as predições do FGM e da solução detalhada, mas a grande quantidade de fuligem no sistema ainda introduz alguns desafios para a obtenção de bons resultados quantitativos. Entretanto, este trabalho demonstrou o grande potencial do método FGM em predizer a formação de fuligem em chamas multidimensionais de difusão de etileno em tempos computacionais reduzidos.

Palavras-chave: Chama laminar de difusão; modelo de formação de fuligem; radiação; acoplamento de massa e energia; Flamelet Generated Manifold (FGM)

ABSTRACT

The objective of this thesis is to study soot formation in laminar diffusion flames. For soot modeling, a semi-empirical two equation model is chosen for predicting soot mass fraction and number density. The model describes particle nucleation, surface growth and oxidation. For flame radiation, the radiant heat losses (gas and soot) is modelled by using the grey-gas approximation with Optically Thin Approximation (OTA). Different transport models (detailed or simplified) are evaluated. For the chemical kinetics, detailed and reduced approaches are employed. In the present work, the automatic reduction technique known as Flamelet Generated Manifold (FGM) is being explored. This reduction technique is able to deal with detailed kinetic mechanisms with reduced computational times. To assess the soot formation a variety of numerical experiments were done, from one-dimensional ethylene counterflow adiabatic flames to two-dimensional coflow ethylene flames with heat loss. In order to assess modeling limitations the mass and energy coupling between soot solid particles and gas-phase species are investigated and quantified for counterflow flames. It is found that the gas and soot radiation terms are of primary importance for flame simulations. The additional coupling terms (mass and thermodynamic properties) are generally a second order effect, but their importance increase as the soot amount increases. As a general recommendation the full coupling should be taken into account only when the soot mass fraction, Y_S, is equal to or larger than 0.008. Then the simulation of soot is applied to two-dimensional ethylene co-flow flames with detailed chemical kinetics and explores the effect of different transport models on soot predictions. It is found that the gas and soot radiation terms are also of primary importance for flame simulations and that a first attempt to solve the two-dimensional ethylene co-flow flame can be done using a simplified transport model. Finally an implementation of the soot model with the FGM reduction technique is done and different forms for storing soot information in the manifold is explored. The best option tested in this work is to solve all flamelets with soot and gas-phase species in a coupled manner, and to store the soot rates in terms of specific surface area in the manifold. In the two-dimensional simulations, these soot rates are then retrieved to solve the additional equations for soot modeling. The results showed a good qualitative agreement between FGM solution and the detailed solution, but the high amount of soot in the system still imposes some challenges to obtain good quantitative results. Nevertheless, it was demonstrated the great potential of the method for predicting soot formation in multidimensional ethylene diffusion flames with reduced computational time.

Keywords: Laminar diffusion flame; soot modeling; radiation; mass and energy coupling; Flamelet Generated Manifold (FGM)

INDEX

LIST OF FIGURES

LIST OF TABLES

LIST OF ABBREVIATIONS

CFD	Computational Fluid Dynamics
CHEM1D	One-dimensional laminar flame code
CHEMKIN	Software tool for solving complex chemical kinetics problems
PROMEC	Programa de Pós-Graduação em Engenharia Mecânica
FGM	Flamelet Generated Manifold
FLUENT	CFD software
FPI	Flame Prolongation of the ILDM
FPV	Flamelet/Progress Variable Model
HACA	H-abstraction-C_2H_2-addition
ILDM	Intrinsic Low Dimensional Manifold
LES	Large Eddy Simulation
NSC	Nagle-Strickland-Constable model
OTA	Optically Thin Approximation
QSS	Quasi-Steady State
PAH	Polycyclic Aromatic Hydrocarbon
RHS	Right Hand Side
SLFM	Steady Laminar Flamelet model
SNBCK	Statistical Narrow Band Correlated-k model
UFRGS	Universidade Federal do Rio Grande do Sul
UHC	Un-Reacted Hydrocarbons

LIST OF SYMBOLS

English Symbols

a	Strain rate, s^{-1}
A	Pre-exponential factor, various units
c_p	Specific heat capacity at constant pressure of the mixture, J (kg K)$^{-1}$
$c_{p,i}$	Specific heat capacity at constant pressure of species i, J (kg K)$^{-1}$
C	Soot radiation constant, W m^{-3} K^{-5}
C_i	Thermophoretic velocity constant, -
C_{min}	Average number of carbon atoms in the incipient soot particle, -
d_p	Soot particle diameter, m
$D_{i,j}$	Ordinary binary diffusion coefficients of species i into species j, m^2 s^{-1}
D_{im}	Mixture-averaged diffusion coefficient, m^2 s^{-1}
D_s	Soot diffusion coefficient, m^2 s^{-1}
$D_{T,i}$	Thermal diffusion coefficient of species i, kg m^{-1} s^{-1}
E_a	Activation energy, J mol^{-1}
$\mathbf{f_i}$	Body force vector, m s^{-2}
f_v	Soot volume fraction, -
g	Gravity acceleration, m s^{-2}
h	Total specific enthalpy of the mixture, J kg^{-1}
h	Height above the burner exit face, m
h_i	Specific enthalpy of species i, J kg^{-1}
h_i^0	Specific enthalpy of formation of species i, J kg^{-1}
$\mathbf{I}$	Identity tensor, -
j_i	Mass diffusion flux of species i, kg m^{-2} s^{-1}
j_q	Heat flux, kJ m^{-2} s^{-1}
k	Reaction rate constant coefficient, various units
K	Stretch rate, s^{-1}
Le_i	Lewis number of species i, -
m_i	Mass of species i, kg
M	Mass, kg
Ma	Mach number, -

MW_i	Molecular weight of species i, kg kmol^{-1}
MW	Molecular weight of the mixture, kg kmol^{-1}
$\mathcal{M}_i$	Species i, -
N	Number of species, -
N_A	Avogadro number (6.022×10^{26}), particles/kmol
N_S	Soot number density, particles (kg of mixture)$^{-1}$
p	Pressure of the mixture, N m^{-1}
p_i	Partial pressure of species i, N m^{-1}
p_0	Ambient pressure, N m^{-1}
P_i	Partial pressure of species i, atm
$\dot{q}_R'''$	Radiation heat source term, W m^{-3}
$\mathbf{q}$	Heat flux vector, W m^{-2}
r	Cylindrical radial coordinate, m
$R_{1,2,...}$	Soot rates, kmol m^{-3} s^{-1}
R_u	Universal gas constant, J(mol K)$^{-1}$
S	Specific soot surface area, m^2 m^{-3}
S	Volumetric heat source term, W m^{-3}
t	Time, s
T	Temperature, K
T^{ref}	Reference temperature, K
u	Flow velocity, m s^{-1}
u, v	Cylindrical velocity components (axial and radial), m s^{-1}
$\mathbf{v}$	Flow velocity vector, m s^{-1}
V	Volume, m^3
$\mathbf{V_i}$	Molecular diffusion velocity vector of species i, m s^{-1}
V_T	Thermophoretic velocity of the soot particles, m s^{-1}
x	Cartesian coordinate, m
X_i	Molar fraction of species i, -
$\mathcal{Y}$	Progress variable, kmol kg^{-1}
Y_i	Mass fraction of species i, -
Y_S	Soot mass fraction, -
z	Cylindrical axial coordinate, m

Z	Mixture fraction, -
Z_j	Element mass fraction of element j, -

Greek Symbols

α_i	Weight factor of species i, kmol kg^{-1}
β	Temperature coefficient, -
ρ	Mixture density, kg m^{-3}
ρ_i	The partial density of species i, kg m^{-3}
ρ_C	Soot density, kg m^{-3}
τ	Stress tensor, N m^{-2}
$\dot{\omega}_i$	Reaction source term of the species i, kg m^{-3} s^{-1}
$\bar{\dot{\omega}}_i$	Molar reaction rate of the species i, mol m^{-3} s^{-1}
$\dot{w}_{Y_S}$	Source terms of soot mass fraction, kg m^{-3} s^{-1}
$\dot{w}_{N_S}$	Source terms of soot number density, particles m^{-3} s^{-1}
μ	Dynamic viscosity, kg m^{-1} s^{-1}
μ_i	Dynamic viscosity of species i, kg m^{-1} s^{-1}
ν	Stoichiometric oxidizer-to-fuel ratio, kg kg^{-1}
$\nu_{i,j}$	Stoichiometric number of moles of species i participating in the reaction j, -
λ	Thermal conductivity coefficient, W m^{-1} K^{-1}
λ	Thermal conductivity coefficient of species i, W m^{-1} K^{-1}
Φ_{kj}	Dimensionless quantity, -
χ	Scalar dissipation rate, s^{-1}
σ	Stefan-Boltzmann constant (5.669×10^{-8}), W m^{-2} K^{-4}
κ	Absorption coefficient of the mixture, m^{-1}
κ_i	Absorption coefficient of species i, Pa m^{-1}

Superscript

T	Transpose of the tensor
$'$	Reactants side
$''$	Products side

Subscript

$crit$	Critical
f	Forward
f	Flame

int	Integrated
max	Maximum
r	Reverse
s	Soot
st	Steady state
sur	Surrounding

Other Notation

$[X]$	Molar concentration of species X, kmol m^{-3}
$\prod$	Multiplication

1 INTRODUCTION

Combustion is one of the most important energy conversion process in the world. The world primary energy supply, in the year of 2014, by fuel type, was oil, 31.3%, coal/peat, 28.6%, natural gas, 21.2%, biofuels and waste, 10.3%, nuclear, 4.8%, hydro, 2.4%, and others, 1.4%, accordingly to IEA, 2016. This means that combustion processes are, directly or indirectly, responsible for around 90% of the world total energy supply. Even for countries with important renewable energy sources as Brazil (41.2%) (EPE, 2016) combustion is still the major conversion process (in Brazil it amounts up to about 80%). On the other hand combustion is responsible for the major part of human emissions of gaseous pollutants and particulate matter to the atmosphere, resulting in negative impacts to the environment and health of humans and animals. Thus, many research and development efforts are driven by the increasing need to enhance the efficiency of combustion processes and to reduce pollutant emissions. In order to achieve these goals a fundamental understanding of the major phenomena of combustion processes is required. In this scenario modelling tools that are able to predict the main characteristics of the process with low computational cost are of great interest and is one of the objectives of this work.

Combustion can be classified by the reactants mixing. The two extreme situations are premixed and non-premixed flames. In premixed flames the reactants are molecularly mixed before reaching the flame region. For non-premixed flames the reactants are separated and meet only at the flame front where reactions take place. The intermediary situation is that of a partially premixed flame where some fuel and oxidant are premixed prior to combustion, but another part is separated. Then, this situation combines characteristics of premixed and non-premixed flames. Industrially non-premixed flames are preferred due to hazard concerns since separated feeding streams of fuel and oxidant are safer.

Some devices that use combustion as the conversion energy process are internal combustion engines, gas turbines, boilers and furnaces. In these devices the flame is usually confined in a combustion chamber and/or stabilised on a burner head. In constant pressure situations (burners in general), the energy released by combustion is converted into hot gases and thermal radiation, then is through surface convection and radiation heat transfer that the energy is in fact used to heat up a charge or the walls of the confining chamber. In engines and gas turbines the gas expansion is the responsible for the work production. In all these cases the thermal radiation heat transfer may plays an important role in the energy transfer or on the device operation. Then the ability to predict the radiation emission by flames is required in order to design more efficient devices.

Apart from the main gas pollutants produced by combustion (CO, NO_x, SO_x, and un-reacted hydrocarbons, UHC), soot particles are of great concern. Soot is an agglomeration of particles, mainly formed by carbon with other elements in small quantities such as hydrogen and oxygen. It is formed especially in non-premixed flames under fuel-rich conditions at high temperatures. These particles are carcinogenic and produce deposits of solid matter that may compromise the device operation. On the other hand, for the major part of combustion devices thermal radiation is linked to the presence soot. Soot solid particles emit radiation in a broad wavelength range and frequently dominates the radiation emission in flames (gaseous species as CO_2 and H_2O emit radiation in restricted bands of the wavelength spectrum). Therefore, soot formation is an important issue in combustion both from the environmental and energy heat transfer point of views.

To address all the phenomena present in combustion process can be a major challenge either for experimental or for theoretical approaches. The scenario is further complicated by the flow turbulence that interacts with chemical reactions and thermal radiation. However, studies in laminar flames, where turbulence effects are not present, permit a detailed validation of models. For this reason the present study will be concerned with laminar non-premixed flames where soot formation and radiation emission are of interest. Those aspects are clearly found on ethylene diffusion flames, in which high amount of soot is formed and radiative heat loss plays an important role. The approach of this work is theoretical and will employ numerical simulations to study soot formation in either ethylene counterflow laminar diffusion flames and ethylene coflow laminar flames. Priority will be given for models that are capable of producing detailed information about the process with reduced computational requirements. For soot modeling, a semi-empirical model is chosen since it combines important steps for soot formation, accurate predictability of global soot variables and low computational time, specially for practical combustion systems. For flame radiation, the radiant heat losses (gas and soot) will modeled by using the grey-gas approximation, i.e., there is no dependence on the wave number, and Optically

Thin Approximation (OTA) , i.e., the medium does not scatter nor absorb radiation. For the chemical kinetics, either detailed and simplified approaches will be employed. In the present work, an automatic reduction technique known as Flamelet Generated Manifold (FGM) will be explored. This reduction technique is able to deal with detailed kinetic mechanisms with reduced computational times.

1.1 Literature review:

Soot is commonly found in diffusion flames of hydrocarbon fuels. The presence of soot particles increases the radiant heat losses, decreases the flame temperature and gives a characteristic yellowish luminosity to the flame. The increased radiant heat transfer is not desirable for devices such as gas turbines and diesel engines due to a decrease of the device performance, but may be of interest in industrial furnaces where high heat transfer rates are required. In flares of petrochemical plants or off-shore platforms the presence of soot influences the intensity of the radiant heat flux at the ground level which determines the minimum stack height to protect personnel and equipment. In all cases, emissions of soot particles to the atmosphere are limited by law due to environmental and health concerns. Therefore, the capability of predicting soot formation in flames is important for many applications.

In Kennedy, 1997, the models for soot prediction are grouped in three categories: (i) empirical correlations, (ii) semi-empirical models and (iii) models with detailed chemistry. In the first category, models rely on global rate equations for soot generation and destruction adjusted to reproduce experimental data in specific combustion devices. They are easy to implement and are computationally fast, but since they do not describe soot formation steps, their validity is restricted to the conditions and devices for which they were developed. In the second category, the models attempt to incorporate some fundamental steps of the soot formation process, i. e., precursor formation, soot inception, particle growth, coagulation and oxidation. Two typical examples of this model are the one from Leung et al., 1991, and the one from Fairweather et al., 1992. These models usually take acetylene-based nucleation, instead of the more complex Polycyclic Aromatic Hydrocarbons (PAHs)-based nucleation, since the later requires the use of large gas-phase reaction mechanisms. The soot-particle dynamics is usually simplified, with the soot particles follow a mono-disperse distribution that is described by a two-equation model, one for soot mass fraction Y_S and another for soot number density N_S. Usually the rate equations that describe the soot formation processes are still dependent on the experimental conditions used to fit the model, but they are not dependent on specific devices. These models have demonstrated good agreement with experiments on global soot characteristics, like soot volume fraction and soot number density, but they lack detailed soot properties such as aggregate structure and size distribution [Kim and Kim, 2015]. In the third category, the models are improved with detailed kinetic mechanisms that can track the evolution of PAHs and with detailed soot dynamics that take into account the soot particle size distribution. The detailed gas-phase kinetic mechanisms are required to model PAHs formation and consumption as well as their interaction with the particle surface. The nucleation process involves collisions of molecules of benzene (C_6H_6) [Violi, 2004], naphthalene ($C_{10}H_8$) [D'Anna and Kent, 2006], pyrene ($C_{16}H_{10}$) [Appel et al., 2000; Skjøth-Rasmussen et al., 2004; Chernov et al., 2014], or multiple PAHs [Wang et al., 2015]. Similarly, different species may participate in the PAHs evolution and particle surface growth process. The particle dynamics are modeled by many approaches, including the sectional method [Pope and Howard, 1997; Zhang et al., 2009], the method of moments [Pitsch et al., 2000; Frenklach, 2002] and stochastic methods [Balthasar and Frenklach, 2005; Chen et al., 2013]. Since models in this category are more fundamental, they are likely to work in different combustion situations. The drawback of this approach is the difficult implementation and high computational costs [Raj et al., 2009], and even for these accurate models it is necessary to include some tunings parameters [Chernov et al., 2014].

Special attention must be payed to the consumption and formation of some gas-phase species during soot nucleation, growth and oxidation, requiring additional reaction source terms to be included in the species mass conservation equations and correction of the mixture density. On the other hand, the presence of soot particles implies additional energy source terms in the energy equation. For example, the radiant heat loss from soot is a well know effect that reduces the flame temperature [Hall, 1994; Liu et al., 2002; Sivathanu and Gore, 1994; Liu et al., 2004], and soot particles release heat when oxidized. Some works neglect the mass and energy coupling between gas and solid phases considering that the amount of soot within the flame is so small that it does not change the flame composition and enthalpy [Moss et al., 1995; Bennett et al., 2009]. But most soot research includes mass and energy coupling terms [Sivathanu and Gore, 1994; Liu et al., 2004; D'Anna and Kent, 2006; Charest et al., 2014, 2010; Mehta et al., 2009; Zhang et al., 2009; Domenico et al., 2010; Chen et al., 2013], although the importance of this choice is not always clear and frequently the implementation of such coupling terms are not clearly described. Thus, when modeling soot formation in flames one has to decide how these interactions should be accounted for.

The interaction between soot and gas-phase species was investigated by the following authors: Kennedy et al., 1996, studied the soot formation in a laminar coflow ethylene-air diffusion flame. They used a semi-empirical model based on acetylene as the soot precursor and considered the mass coupling between the phases. Additional terms for C_2H_2, OH and CO in the gas-phase chemistry were accounted for due to soot reactions. The coupling was evaluated by comparing the solution of the gas-phase chemistry only, without radiation, against the solution of gas and soot, with mass coupling and soot radiation (no gas radiation). The authors found that the inclusion of soot in a coupled manner has a significant impact on the structure of the flame, specially near the flame tip where the soot amount was substantial. However, they did not quantify such impact on the flame. Carbonell et al., 2009, studied the soot formation in a laminar coflow methane-air diffusion flame. They chose the Leung et al., 1991, model for soot prediction based on acetylene as the soot precursor. The authors compared versions of flamelet approaches, which included or not the effect of soot on the gas-phase chemistry, against a full coupled detailed solution. The decoupled flamelet model, E-EDFM, obtained decoupling the soot mechanism from the gas-phase mechanism, over-predicted the maximum soot volume fraction, $f_{v,max}$, by 27.65% when compared with the most detailed version. According to the authors this happened because there was an excess of C_2H_2 in the flame which increases soot nucleation and growth. They conclude that the coupling was important, but, again no quantification of the differences was presented and they didn't explore their model in different conditions. Domenico et al., 2010, proposed a new soot formation model, based on a sectional approach for the description of PAHs and a two-equation model for soot. The model was validated for diffusion and partially premixed flames in a coflow burner for methane, ethylene and kerosene. They included the mass coupling between the soot and the gas-phase and soot radiative heat loss only. For the partially premixed ethylene case, they found that profiles of acetylene and benzene were slightly changed when soot radiation model was accounted for, despite the temperature variations. Wang et al., 2015, developed a PAH-based soot model based on the method of moments to simulate soot formation in ethylene counterflow diffusion flames. The soot model included thirty-six nucleation reactions from eight PAH molecules, particle surface growth from modified HACA growth mechanism, PAH condensation and particle-particle coagulation. The consumption and formation of soot related gas-phase species was accounted for as source terms to update gas-phase species concentrations. In a comparison between only gas-phase solution and a solution with soot model (with mass and radiation coupling terms) they found that the coronene (pyrene) concentration was reduced by 30.5% (10%). Nevertheless, they did not quantify the soot coupling impact on other flame scalars and did not explore their model in different conditions.

Then, the question that still remains is what are the conditions for which a full description of the gas- and solid-phase interactions is mandatory.

Another important aspect is the prediction of the thermodynamic state of the system and the gaseous species that are precursors of the soot particles. For this task usually large kinetic mechanisms are used, but they imply in high with a computational cost. For one-dimensional flames the use of such mechanisms are conceivable, but for multidimensial flames it can be a computational burden. In such conditions is important a method which reduces the complexity and therefore the time involved to predict the state of the system. Such reduction may be obtained by employing steady state and partial equilibrium assumptions, but automatic reduction techniques based on tabulated chemistry are usually preferred. Among the automatic reduction techniques, the flamelet approach is one of the most popular. In this approach, it is assumed that the flame may be represented by one-dimensional flames (flamelets) whose solutions are stored in a look up table for further use in the solution of multidimensional flames. Such approaches include the Flame-Prolongation of ILDM (FPI) [Gicquel et al., 2000], Flamelet Generated Manifold (FGM) [van Oijen and de Goey, 2000] and the Flamelet/Progress Variable Model (FPV) [Pierce and Moin, 2004]. The first two approaches are quite similar, all of them based on the mixture fraction and progress variable as the controlling parameters. More details about these models will be given in Chapter 2.

In this thesis the FGM reduction technique will be employed. According to van Oijen and de Goey, 2000, for multidimensional simulations this approach is able to reduce computational the time of up to 100 times with good quality results. The FGM method was created first to solve premixed flames (e.g. van Oijen and de Goey, 2000, 2002; van Oijen et al., 2001) and has been extended to to partially premixed and non-premixed laminar flames with success (e.g. Fiorina et al., 2005; Delhaye et al., 2008; Verhoeven, 2011; Verhoeven et al., 2012; van Oijen and de Goey, 2004).

The steady flamelet approach relies on the assumption that the unsteady terms are much smaller than the other terms in the species transport equations. For slow process as NO and soot formation this assumption may not be accurate. For the NO it has been shown [van Oijen et al., 2016] that improved results are obtained with the inclusion of an additional transport equation for NO with the source term being retrieved from the manifold. For modeling soot with FGM approach it is expected that a similar approach have to be employed.

Few works have been done combining soot modeling and flamelet approach and most have done on slightly sooting flames (e.g. Steward et al., 1991; Balthasar et al., 1996; Pitsch et al., 2000; Carbonell et al., 2009; Mueller and Pitsch, 2012; Demarco et al., 2013; Kim and Kim, 2015) and even less specifically in the FGM/FPI framework (e.g. Strik, 2010; Lecocq et al., 2014). Also, it has been found a lack of studies in soot modeling using tabulated chemistry for cases with a high production of soot, like ethylene flames, and frequently the available models are poorly described.

Steward et al., 1991, studied soot formation in non-premixed kerosine/air flames employing the flamelet combustion model. A simplified soot model was used and incorporated the influences of nucleation, surface growth and coagulation on soot volume fraction and number density. Experimental measurements were compared with detailed flowfield predictions to fit the parameters of the soot model and then good agreements were obtained. In this work the soot was treated as a small perturbation on the gas-phase composition ($f_v < 10\ ppm$) and decoupled the mixture fraction from the soot solid phase. However, the authors suggested that for higher soot amounts the mixture fraction should not be decoupled from the soot. Balthasar et al., 1996, studied soot formation in a acetylene/nitrogen-air laminar diffusion flame employing the flamelet concept. The fuel stream of the chosen flame consisted of 68.25 mol % N_2 and 31.75 mol % acetylene and the oxidizer was air. The soot mass fraction was post-processed from the gas-phase solution flamelets. Then the rates for particle inception, surface growth (normalized with

f_v) and oxidation (also normalized with f_v) were stored in the flamelet library. So in the two-dimensional flow, an additional equation for soot volume fraction was solved, which source term was reconstructed by these rates stored in the library. The authors declared that this approach was limited to flames in which soot formation has only little effect on flame structure, such as the one investigated. Their simulation found a $f_{v,max} = 4\ ppm$. They only compared their f_v at the centerline results to experimental data, i.e., no evaluation to a more detailed solution. Pitsch et al., 2000, studied the influence of preferential diffusion of soot particle on a turbulent ethylene-air diffusion flame employing the flamelet concept. The equation for soot was derived considering preferential diffusion of soot in the mixture fraction space. Comparison with experimental data showed good agreement. The two phases were coupled only by radiation heat loss (soot and gas). Their simulation found a $f_{v,max} = 1.7\ ppm$. Carbonell et al., 2009, studied the soot formation in a laminar coflow methane-air diffusion flame employing a variation of the unsteady flamelet model (Pitsch et al., 1998, and derived approaches). The authors tested some methods for storing and retrieving the soot information from the flamelet table. The best option was solving each flamelet coupling both phases (gas and soot), storing in the database the soot rates divided by the specific area and then solving the soot equations retrieving those specific soot rates from the database. It is important to note that methane flame produced small amounts of soot ($f_{v,max} = 0.5\ ppm$), rendering the coupling effects less problematic. Strik, 2010, studied the application of FGM in a engine model with turbulence and chemical kinetics of high order hydrocarbons in combination with a complex geometry. The author focused in the auto-ignition behavior, adapting the model for EGR conditions and extending it with NOx and soot predictions, employing an empirical soot model. No description is given about the influence of soot in the tabulated chemistry. The soot model was not be able to predict quantitative correct results without tuning the pre-exponential constants of the model. Mueller and Pitsch, 2012, studied soot formation in a turbulent non premixed flame. They used Large Eddy Simulation (LES) with the Flamelet/Progress Variable combustion model. For soot modeling a Hybrid Method of Moments was used. In this work the authors included a source term in the element fraction based mixture fraction Z to account the removal of PAH from the gas-phase to the soot formation. The comparison with experimental data showed good agreement with the temperature profile, nevertheless the soot volume fraction was not able to reproduce the experimental data. The maximum soot volume fraction reported was less then 0.1 *ppm*. Demarco et al., 2013, studied the influence of thermal radiation on soot production in laminar axisymmetric diffusion flames. They used the Steady Laminar Flamelet (SLF) of Peters, 1984, method, with a semi-empirical soot model and two radiation models, a more detailed Statistical Narrow Band Correlated-k model (SNBCK) and optically thin approximation (OTA). In this work the authors tested the numerical model in a wide range of flames, from low (methane flames) to high (propane flames) production of soot. Nevertheless they did not provide details about the coupling method between the flamelet table and the soot modeling. Additionally, they only compared their numerical results to experimental data, i.e., no evaluation relative to a reference solution is presented. Lecocq et al., 2014, used the FPI approach to studied soot prediction and radiation in complex industrial burners. The authors used a semi-empirical two-equation soot model to predict soot mass fraction and number density. They performed a Large Eddy Simulation of a combustion chamber of a helicopter engine with kerosene being the fuel of interest. Their main focus was in the radiative coupling effect of soot and gas, neglecting the mass coupling of soot and the gas-phase species. Therefore the flamelets only accounted for the gas-phase species and the heat loss from gas and soot emission. The tridimensional soot field was then reconstructed from the gas-phase species stored in the flamelet library. Also, neither comparison with experimental data nor detailed simulation were performed to assess the validity of the FPI approach with soot and radiation effects. Kim and Kim, 2015, improved the model of Carbonell et al., 2009, with an approach which simultaneously considers gaseous radiation and soot radiation in the same mixture fraction space while it circumvents the unphysical diffusion of soot distribution by treating the diffusivity of soot particles as practically zero. Its flamelet approach was then compared to detailed chemistry solution and experimental data of an atmospheric methane/air laminar non-premixed flame and good agreements were found. Here again the interaction of soot was mild, with $f_{v,max} = 0.55$ *ppm*.

The modeling of soot with flamelet approaches allows different forms of implementation and no method is widely recognised as the best one. Particularly, there is little information about the implementation of soot models with the FGM approach or other flamelet approaches based on mixture fraction and progress variable. The importance of the coupling terms between gas and solid phases are also not totally clear. This thesis will explore these aspects in one-dimensional and in multidimensional flame simulations.

1.2 Objectives

The objective of the present thesis is to study the implementation of a semi-empirical soot formation model with detailed kinetic mechanisms and with the Flamelet Generated Manifold reduction technique.

Some basic questions that will be addressed along the thesis are:

1. To find the conditions for which a full description of the gas- and solid-phase interactions is mandatory.
2. To find the best method for storing soot information in the FGM tables to appropriately simulate high soot loads.
3. To quantitatively show the impact of different transport models in soot predictions.

1.3 Outline

After the Introduction chapter, the present thesis is organised in more five chapters. Chapter 2 presents the basic formulation for modeling laminar diffusion flames. Chapter 3 explores the coupling terms between the gas and solid phases in one-dimensional counterflow flames. This chapter was published in 14 Oct 2016 in the Combustion Theory and Modelling (DOI:10.1080/13647830.2016.1238512). Chapter 4 shows the simulation of soot in two-dimensional co-flow flames with detailed chemical kinetics and explores the effect of different transport models on soot predictions. Chapter 5 brings an implementation of the soot model with the FGM reduction technique, were different forms for storing soot information in the flamelet table are explored. Finally, in Chapter 6, the general conclusions are summarised and ideas for future works are suggested.

2 MODELING DIFFUSION FLAMES

2.1 Conservation equations

In this section the equations describing chemically reacting flows are presented. The main approximations used for the case of laminar atmospheric diffusion flames are highlighted. The reacting flow is governed by a set of equations that account for the conservation of total mass, mass of species, momentum and energy. Mixture properties and closure equation are also required. The derivation of the conservation equations for a reacting gas mixture can be found in Williams, 1985, Poinsot and Veynante, 2005, and in Law, 2006. This section only presents the resulting equations.

Continuity equation

The overall mass conservation (continuity) for a system in the vector form can be expressed as

$$\frac{\partial \rho}{\partial t} + \nabla \cdot (\rho \mathbf{v}) = 0, \tag{2.1}$$

where ρ is the mixture density and $\mathbf{v}$ is the flow velocity.

Momentum transport equation

The momentum conservation for the flow is represented by the compressible form of the Navier-Stokes equations

$$\frac{\partial (\rho \mathbf{v})}{\partial t} + \nabla \cdot (\rho \mathbf{v}\mathbf{v}) = -\nabla p - \nabla \cdot \tau + \rho \sum Y_i \mathbf{f_i}, \tag{2.2}$$

where p is the pressure, τ is the stress tensor, Y_i is the mass fraction of species i defined as $Y_i = \rho_i/\rho$, with ρ_i the partial density of species i, and $\mathbf{f_i}$ is the body force.

Species transport equation

In a reacting flow the transport equation for the mass fraction of species i, Y_i, is expressed as

$$\frac{\partial (\rho Y_i)}{\partial t} + \nabla \cdot [\rho(\mathbf{v} + \mathbf{V_i})Y_i] = \dot{\omega}_i, \quad i = 1, ..., N, \tag{2.3}$$

where $\mathbf{V_i}$ is molecular diffusion velocity of species i and $\dot{\omega}_i$ is reaction source term, which represents the net chemical production/destruction of the species i. The species transport equation is solved from $i = 1$ to N, with N being the total number of chemical species.

Energy transport equation

The energy conservation equation can be written in terms of the total specific enthalpy of the mixture, h, as

$$\frac{\partial(\rho h)}{\partial t} + \nabla \cdot (\rho \mathbf{v} h) = -\nabla \cdot \mathbf{q} + \tau : \nabla \mathbf{v} + \frac{Dp}{Dt} + S \tag{2.4}$$

where $\mathbf{q}$ is the heat flux vector, $\tau : \nabla \mathbf{v}$ represents the enthalpy production due to viscous effects, $\frac{Dp}{Dt}$ is the pressure material derivative and S is the volumetric heat source, which in this thesis accounts for the radiation heat loss. The radiation model is explained in the Section 3.1.2.

2.1.1 Constitutive relations

In order to solve the equation system, the stress tensor τ, the diffusion velocity $\mathbf{V_i}$, the chemical source term $\dot{\omega}_i$ and the heat flux vector $\mathbf{q}$ must be defined. The chemical source term $\dot{\omega}_i$ is defined in the Section 2.2 and the remainings terms are now presented:

Stress tensor: For a Newtonian fluid, assuming the Stokes hypothesis, the viscous stress tensor τ has the following form:

$$\tau = -\mu \left[\nabla \mathbf{v} + (\nabla \mathbf{v})^{\mathrm{T}} \right] + \frac{2}{3} \mu (\nabla \cdot \mathbf{v}) \mathbf{I}, \tag{2.5}$$

where $\mathbf{I}$ is the identity tensor , μ is the dynamic viscosity. This term accounts for diffusion of linear momentum.

Diffusion velocity: The multi-component equation for mass diffusion in ideal gas mixtures, derived from the kinetic theory, is given by

$$
\begin{aligned}
\nabla X_i = & \sum_{j=1}^{N} \frac{X_i X_j}{D_{i,j}} (\mathbf{V_j} - \mathbf{V_i}) \\
& + (Y_i - X_j) \left(\frac{\nabla p}{p} \right) \\
& + \left(\frac{\rho}{p} \right) \sum_{j=1}^{N} Y_i Y_j (\mathbf{f_i} - \mathbf{f_j}) \\
& + \sum_{j=1}^{N} \left[\left(\frac{X_i X_j}{\rho D_{i,j}} \right) \left(\frac{D_{T,j}}{Y_j} - \frac{D_{T,i}}{Y_i} \right) \right] \left(\frac{\nabla T}{T} \right), \quad i = 1, ..., N,
\end{aligned}
\tag{2.6}
$$

where $X_i = Y_i MW/MW_i$ is the molar fraction (where MW is the molecular weight of the mixture and MW_i is the molecular weight of the species i), $D_{i,j}$ is the ordinary binary diffusion coefficient and $D_{T,i}$ is the thermal diffusion coefficient. The multicomponent diffuson equation asserts that the concentration gradients are supported by diffusion velocities (the first term in the Right Hand Side (RHS)), the mass diffusion due to the pressure gradient (second term), the mass diffusion due to the body force $\mathbf{f_i}$ (third term) and the mass diffusion due to gradient temperature (Soret effect)(fourth term). Nonetheless, in most of cases the concentration gradient term dominates [Law, 2006].

Heat flux: The heat flux vector can be expressed as:

$$
\begin{aligned}
\mathbf{q} = & - \lambda \nabla T \\
& + \sum_{i=1}^{N} \rho \mathbf{V_i} Y_i h_i \\
& + R_u T \sum_{i=1}^{N} \sum_{j=1}^{N} \left(\frac{X_j D_{T,i}}{MW_i D_{i,j}} \right) (\mathbf{V_i} - \mathbf{V_j}),
\end{aligned}
\tag{2.7}
$$

where λ is the thermal conductivity, h_i is the specific enthalpy of species i and R_u is the universal gas constant. The heat flux vector $\mathbf{q}$ is composed of three terms, the first term is the heat conduction flux, ruled by Fourier law, and caused by temperature gradient. The second term is the heat diffusion due to species mass diffusion. And the third term accounts for the Dufour effect, a second-order diffusion, which represents the heat flux caused by concentration gradients.

2.1.2 Auxiliary Relations

The system of $N+5$ variables (Y_i, ρ,$\mathbf{v}$ and T) through the conservation equations (Equations 2.1 - 2.4) is only completed with the following auxiliary relations:

Mixture Enthalpy:

$$h = \sum_{i=1}^{N} Y_i h_i, \quad h_i = h_i^0 + \int_{T^{ref}}^{T} c_{pi}(T)dT \tag{2.8}$$

where h_i, h_i^0 and $c_{p,i}$ are the specific enthalpy, specific enthalpy of formation at reference temperature T^{ref} and specific heat capacity at constant pressure of species i, respectively. Note that the effect of chemical reactions is accounted for in the energy conservation, Equation 2.4, through the changes of the mixture composition in Equation 2.8.

Ideal Gas Equation of State:

$$p = \frac{\rho R_u T}{MW}, \quad MW = \left(\sum_{i=1}^{N} \frac{Y_i}{MW_i} \right)^{-1}. \tag{2.9}$$

Thermodynamic and transport properties:

The thermodynamic properties, e.g., h_i or $c_{p,i}$, mixture transport properties of viscosity μ and thermal conductivity λ and transport properties of species i, e.g. $D_{i,j}$ or $D_{T,i}$, are not yet defined. These quantities are derived from molecular theory and can be found in Hirschfelder et al., 1954, Chapman and Cowling, 1970, Williams, 1985, and in Bird et al., 2002. The thermodynamic properties are well correlated to temperature in polynomial form and are usually presented in tabulated-format, for example in CHEMKIN format [Kee et al., 1990]. In contrast, the transport properties depend on temperature and mixture composition in a very complex way, making their evaluation very expensive. There are many formulations to deal with these evaluations. In the present work it is used the semi-empirical formula of Wilke, 1950, for viscosity

$$\begin{aligned} \mu &= \sum_{k=1}^{N} \frac{\mu_k}{1 + 1/X_k \sum_{j=1, j\neq k}^{N} X_j \Phi_{kj}}, \\ with \quad \Phi_{kj} &= \frac{1}{\sqrt{8}} \left(1 + \frac{MW_k}{MW_j} \right)^{-1/2} \left(1 + \left(\frac{\mu_j}{\mu_k} \right)^{1/2} \left(\frac{MW_j}{MW_k} \right)^{1/4} \right)^2, \end{aligned} \tag{2.10}$$

which μ_i is the viscosity of species i and Φ_{kj} is a dimensionless quantity.

The mixture averaged thermal conductivity λ, can also be written with the semi-empirical formula of Mason and Saxena, 1958:

$$\lambda = \sum_{k=1}^{N} \frac{\lambda_k}{1 + 1/X_k \sum_{j=1, j\neq k}^{N} X_j \Phi_{kj}}, \qquad (2.11)$$
$$with \quad \Phi_{kj} = \frac{1.065}{\sqrt{8}} \left(1 + \frac{MW_k}{MW_j}\right)^{-1/2} \left(1 + \left(\frac{\lambda_j}{\lambda_k}\right)^{1/2} \left(\frac{MW_j}{MW_k}\right)^{1/4}\right)^2,$$

which λ_i is the thermal conductivity of species i and Φ_{kj} is a dimensionless quantity. The previous equation for λ is not usually used in numerical combustion, instead most combustion studies used the semi-empirical combination-averaging formula of Mathur et al., 1967:

$$\lambda = \frac{1}{2} \left(\sum_{i=1}^{N} X_i \lambda_i + \left(\sum_{i=1}^{N} \frac{X_i}{\lambda_i} \right)^{-1} \right). \qquad (2.12)$$

The binary diffusion coefficients, the viscosity and thermal conductivity of a species i depend on the Lennard-Jones molecular potentials. These properties may be written in terms of the Lennard-Jones parameters for each species, leading to the complex expressions, or can be written in polynomial form with temperature dependency [Kee et al., 1986]. The benefit of the later strategy, is that only comparatively simple fits need to be evaluated instead of complex expressions.

2.1.3 Approximations:

In this subsection the assumptions considered for modeling atmospheric laminar diffusion flames are presented together with the final form of the conservation equations. At this point we have a complete set of equations (Equations 2.1 - 2.4, 2.8 - 2.9) which describes the evolution of $N + 7$ variables (Y_i, ρ,$\mathbf{v}$, T, h and p). Some considerations are needed to close the problem and they are presented below.

The flames simulated in this thesis take place in low-speed subsonic flow, in other words, they have very low velocity when compared to the speed of sound (the Mach number $Ma^2 << 1$), and therefore the low-Mach number approximation can be applied. With this approximation the pressure is considered approximately constant throughout the domain and is a function of time only ($p \approx p(t)$). The flames considered here are in open ambient, thus the temporal pressure variation is neglected. With this assumption the state equation for an ideal gas, considering the low Mach approximation now reads

$$\rho = \frac{pMW}{R_u T} \simeq \frac{p_0 MW}{R_u T}, \tag{2.13}$$

where p_0 is the ambient pressure (assumed to be constant). In this way the gas density varies only with mixture composition and temperature. Additionally, the pressure material derivative term in the Energy Equation 2.4 can be neglected. With low Mach number flows, the viscous dissipation is also negligible in the energy equation. It is important to note that pressure gradient in the Momentum Equation 2.2 must be retained, since this pressure gradient drives the flow. The mass diffusion caused by the pressure gradient is usually very small and can be neglected (second term in RHS of Equation 2.6). The mass diffusion due to the second-order, thermal diffusion (Soret effect), is also neglected (fourth term in RHS of Equation 2.6), since this effect is only important for small molecular weigh species (H, H_2, He) [Coelho and Costa, 2007]. Also the second-order heat diffusion, the Dufour effect, in the heat flux Equation 2.7 is usually neglected in combustion processes. Finally, in the present work the gravitational force is the only body force to be considered, so that $\rho \sum Y_i \mathbf{f_i} = \rho \mathbf{g}$ in Equation 2.2 and $\mathbf{f_i} = \mathbf{f_j} = \mathbf{g}$ in Equation 2.6. Thus the influence in the diffusion velocity by the body force term vanishes.

With the previous assumptions we arrive at the diffusion velocity $\mathbf{V_i}$ described by the Stefan-Maxwell equation:

$$\nabla X_i = \sum_{j=1}^{N} \frac{X_i X_j}{D_{i,j}} (\mathbf{V_j} - \mathbf{V_i}), \quad i = 1, ..., N. \tag{2.14}$$

This expression is numerically-expensive, since the diffusion velocity of one species $\mathbf{V_i}$ depends on the concentration gradients and the diffusion velocity $\mathbf{V_j}$s of the remaining species. In the present work a frequent approximation is employed to describe the diffusion velocities, which uses a Fick's Law-like expression,

$$\mathbf{V_i} Y_i = -D_{im} \nabla Y_i, \tag{2.15}$$

were D_{im} is an averaged mass diffusion coefficient of the i species into the mixture, also known as mixture-averaged diffusion coefficient. The D_{im} may be obtained by employing the Hirschfelder and Curtiss approximation [Hirschfelder et al., 1954]:

$$D_{im} = \frac{1 - Y_i}{\sum_{i=1, i \neq j}^{N} \frac{X_j}{D_{i,j}}}. \tag{2.16}$$

By definition, these diffusion fluxes should sum to zero, but they do not because of the mixture-averaged approach. Equation 2.15 with Equation 2.16 is an approximation to Stefan-Maxwell equation and a correction on the velocity is needed to all species to guarantee mass conservation. A standard method for this correction is to define a "conservation diffusion velocity" as recommended by Coffee and Heimerl, 1981, and justified by Giovangigli, 1991, by proving that these diffusion velocities correspond to the first term of a convergent series for full matrix diffusion. The diffusion velocity correction $\mathbf{V_c} = -\sum Y_i \mathbf{V_i}$ is then applied to $\mathbf{V_i} = \mathbf{V_i} + \mathbf{V_c}$ so that the summation of all diffusion velocity is null ($\sum_{i=1}^{N} \mathbf{V_i} Y_i = 0$). Another way to overcome the non-conservation of mass is to solve the species transport quation (Equation 2.3) for $i = 1$ until $N - 1$ and the remaining species is found by mass conservation, .i. e., $Y_{N_2} = 1 - \sum_{i=1}^{N-1} Y_i$.

Using the previous considerations we can rewrite the set of transport equation as:

$$\frac{\partial \rho}{\partial t} + \nabla \cdot (\rho \mathbf{v}) = 0, \tag{2.17}$$

$$\frac{\partial (\rho \mathbf{v})}{\partial t} + \nabla \cdot (\rho \mathbf{v}\mathbf{v}) = -\nabla p - \nabla \cdot \tau + \rho \mathbf{g}, \tag{2.18}$$

$$\frac{\partial (\rho Y_i)}{\partial t} + \nabla \cdot (\rho \mathbf{v} Y_i) = \nabla \cdot (\rho D_{im} \nabla Y_i) + \dot{\omega}_i, \quad i = 1, ..., N-1, \tag{2.19}$$

$$\frac{\partial (\rho h)}{\partial t} + \nabla \cdot (\rho \mathbf{v} h) = \nabla \cdot \left(\lambda \nabla T + \sum_{i=1}^{N} \rho D_{im} h_i \nabla Y_i \right) + S. \tag{2.20}$$

Further approximations:

The D_{im} can also be obtained by assuming a constant Lewis number for each species along the combustion process. The Lewis number compares the thermal diffusivity of the mixture to the mass diffusivity of species i and is defined as

$$Le_i = \frac{\lambda}{\rho c_p D_{im}}, \tag{2.21}$$

were c_p is heat capacity at constant pressure of the mixture ($c_p = \sum_{i=1}^{N} c_{p,i} Y_i$). With this approximation the diffusion velocity is neither dependent on the molar fraction gradients of other species i nor on the remaining diffusion coefficients as in Equation 2.14, but only on the given Lewis number. This results in a significant reduction in time to evaluate the multicomponent diffusion velocity, but with some loss in accuracy.

And last, in order to reduce the time to evaluate the multicomponent dynamic viscosity, μ, and thermal conductivity, λ, it is possible to use temperature based functions such as,

$$\frac{\mu}{c_p} = A\left(\frac{T}{298}\right)^B, \tag{2.22}$$

$$\frac{\lambda}{c_p} = C\left(\frac{T}{298}\right)^D, \tag{2.23}$$

where A, B, C and D are constant values obtained by comparing to experimental data or by comparing to more detailed numerical solution. Also, this approach results in a significant reduction in computational time, again with some drawback on the accuracy of the result.

2.2 Chemical kinetics modeling

2.2.1 Reaction Rates

In flames, the reaction region is characterised by the existence of several simultaneous elementary reactions. As an example consider the reaction

$$O_2 + H \underset{k_r}{\overset{k_f}{\rightleftharpoons}} OH + O, \tag{2.24}$$

where the oxygen molecule O_2 reacts with the atomic hydrogen radical H forming two new radicals, the hydroxyl OH and the atomic oxygen O, in what is known as a branching step, i.e., one radical forming two radicals. k_f is the reaction rate coefficient for the forward reaction and k_r is the reaction rate coefficient for the reverse reaction. By the Law of Mass Action, the forward reaction rate for OH formation is proportional to the reagents concentrations

$$\bar{\dot{\omega}}_{OH,f} = k_f\left[O_2\right]\left[H\right], \tag{2.25}$$

where k_f is the rate constant and can be usually modeled in Arrhenius form as,

$$k = AT^\beta \exp\left(\frac{-E_a}{R_u T}\right), \tag{2.26}$$

where A is the pre-exponential factor, β is a temperature coefficient dependency and E_a is the activation energy. These three last parameters are listed in oxidation kinetic mechanisms. In general, the reactions are reversible and the reverse reaction rate is also included. Thus, the net reaction rate for the elementary step under analysis is

$$\bar{\dot{\omega}}_{OH} = \bar{\dot{\omega}}_{OH,f} - \bar{\dot{\omega}}_{OH,r} = k_f \left[O_2\right]\left[H\right] - k_r \left[OH\right]\left[O\right], \tag{2.27}$$

where the reverse reaction rate k_r is found through the equilibrium constant K_c, as

$$K_c = k_f / k_r, \tag{2.28}$$

which can be tabulated as function of temperature.

In a general form, each elementary reaction can be written as

$$\sum_{i=1}^{N} \nu_{i,j}^{'} \mathcal{M}_i \leftrightarrows \sum_{i=1}^{N} \nu_{i,j}^{''} \mathcal{M}_i, \tag{2.29}$$

where $\nu_{i,j}$ is the number of moles of species i participating in the reaction j, N is the number of chemical species, the upper indexes $'$ and $''$ indicate the reactants side and the products side, respectively, and $\mathcal{M}_i$ represents the species i. So, the reaction rate of the j^{th} reaction can be written as

$$\bar{\dot{\omega}}_{i,j} = k_{f,j} \prod_{i=1}^{N} \left[\mathcal{M}_i\right]^{\nu_{i,j}^{'}} - k_{r,j} \prod_{i=1}^{N} \left[\mathcal{M}_i\right]^{\nu_{i,j}^{''}}. \tag{2.30}$$

Finally, the reaction source term, $\dot{\omega}_i$, appearing in species transport equation (Equation 2.3), which includes the contribution of all N_r elementary reaction steps in the mechanism, reads

$$\dot{\omega}_i = MW_i \sum_{j=1}^{N_r} \left(\nu_{i,j}^{''} - \nu_{i,j}^{'}\right) \bar{\dot{\omega}}_{i,j}. \tag{2.31}$$

2.3 Chemical Kinetic Reduction Techniques

An important effort is required to solve the full set of conservation equations for a reactive flow due to the non linearities introduced by the reaction rate terms. This is more critical when a detailed mechanism is employed since one additional conservation equation has to be solved for each one of the $N-1$ species present in the mechanism. Since mechanisms to predict soot usually consider more than 30 species for semi-empirical soot models, and more than 100 species for detailed soot models, the inclusion of such number of conservation equations is still forbidden for the major part of standard computational resources available for engineering applications. Then, a reduction technique is demanded to deal with this problem. These techniques has been studied for some time (for example Bodenstein, 1913, introduced the idea of separating the quasi-steady state species from the fast species), with several variations, but here the most common reduction techniques are shortly explained with the purpose of contextualise the FGM method only. Further details can be found on original articles or in books, e.g. Law, 2006 and Battin-Leclerc et al., 2013.

2.3.1 Conventional Reduction Technique:

In conventional reduction techniques the reaction mechanism is analyzed to identify species for which the steady state approximation may be applied and reactions for which the partial equilibrium may be assumed.

In the case of quasi-steady state (QSS) approximation, it is assumed that the rates of formation and consumption of a certain species are equal. Then, for a homogeneous system this implies that $\dot{w}_i = \dot{w}_{i,formation} - \dot{w}_{i,consumption} \sim 0$ and, consequently, $dY_i/dt \sim 0$, where the steady state name comes from. Then, a balance between these reaction terms is achieved and an algebraic expression that relates the species in steady state and other species of the system is obtained. This idea was introduced by Bodenstein, 1913. This approximation means that this species evolution is a very fast process that responds immediately to a change of the state of the system. The advantage of this approximation is that the conservation equation for this fast species does not have to be solved anymore, instead it is replaced by the non-linear algebraic expression obtained. For a non-homogeneous system, where convection and diffusion terms are important, this approximation results in

$$0 = \dot{w}_i, \tag{2.32}$$

$$\frac{\partial \rho Y_i}{\partial t} + \nabla \cdot (\rho \mathbf{v} Y_i) - \nabla \cdot \left(\frac{1}{Le_i} \frac{\lambda}{c_p} \nabla Y_i \right) = \dot{w}_i \tag{2.33}$$

where the first equation holds for the N_{st} species assumed in steady state and the second equation holds for the remaining $N - N_{st} - 1$ species in the system.

In the case of partial equilibrium assumption, a reaction of the mechanism is assumed to be fast in both forward and backward directions. The result is that this reaction is in equilibrium and, instead of using an Arrhenius model, an algebraic equation is obtained relating the species in this reaction.

With these techniques the mechanism may be reduced indefinitely until an effective one-step mechanism is reached as one assumes additional species to be in steady state. This is done, of course, at the expense of the fidelity of the mechanism. On the other hand the obtained algebraic equations are highly non-linear and not easly solved. Additionally, the selection of species and reactions to be eliminated depends on the experience of the user and requires a thorough analysis of the chemical kinetics mechanism.

To overcome the drawbacks of the conventional technique some approaches have been presented in literature. In next subsection three automatic reduction techniques are reviewed: the Intrinsic Low Dimensional Manifold (ILDM), the Steady Laminar Flamelet Model (SLFM) and the Flamelet Generated Manifold (FGM).

2.3.2 Intrinsic Low Dimensional Manifold (ILDM)

The Intrinsic Low Dimensional Manifold approach, proposed by Maas and Pope, 1992, circumvents the drawbacks of the conventional reduction technique by proposing a method that automatically determines the fast and slow reactions. The method relies on the fact that not every point in composition space is accessible for a given system subjected to some initial constraints. Reactions are allowed to proceed only if they lead the system to move on a defined subspace of the composition space. This subspace is called a manifold. Then, if a chemical systems is represented as a point on this manifold, for all times the state of this system is given by a point that is also a point on the same manifold. The analysis of the trajectories of the system within the manifold allows one to identify an attracting trajectory that is preferentially followed by the system. All fast reactions are attracted to this trajectory, and the motion along the attracting manifold is controlled by the slower reactions. This attracting trajectory is called a low dimensional manifold.

The mathematical method for identifying such low dimensional manifold is based on the analysis of the eigenvectors and eigenvalues of the source term of an homogeneous, adiabatic, isobaric system. The number of controlling variables is proportional to the number of species that are not considered to be in steady state (slow processes) and is imposed arbitrarily. The remaining species are assumed to be in equilibrium with the system. The fidelity of the reduced scheme increases with increasing the number of controlling variables until the full mechanism is recovered. An additional advantage of this method over the QSS technique is that the steady state species may not be the same for the entire progress of reaction. Instead, the steady state species change according to the fast and slow reactions for each state of the system.

For a given reactive system it is possible to parameterize the low dimensional manifold (the accessible region in composition space) as a function of a reduced group of coordinates (corresponding to the number of controlling variables). This is done by building a table that stores the mixture composition and temperature (the state of the system) as function of the concentration of chosen progress variables (species that have a monotonic behavior during the reaction progress). This table is, then, used in subsequent simulations. A drawback of the method is that it relies on the analysis of an homogeneous system, i.e., it is assumed that the reactions are fast phenomena compared to diffusion and convection. For the low temperature regions of a flame this assumption may not be valid and the ILDM approach may give poor results.

2.3.3 Steady Laminar Flamelet Model (SLFM)

The SFLM is an alternative method for reducing the computational effort required in simulating combustion processes. It relies on the idea that the inner flame structure (preheating and reaction regions) is not affected by the flow, thus remaining essentially equal to a one-dimensional flame. This means that the characteristic length scale of the flow (hydrodynamic length scale) is much larger than the flame length scale (flame thickness) so that the flow may distort the flame front, but the flame inner structure remains the same to a first approximation (the parameter that accounts for the effect of the flow field on the flame structure is the scalar dissipation rate to be defined next). In this way it is possible to decouple the flow problem (mixing) from the reaction problem (flame structure).

For diffusion flames the flame structure is parameterized by the mixture fraction

$$Z = \frac{m_1}{m_1 + m_2} = \frac{\nu Y_F - Y_{O_2} + Y_{O_2,2}}{\nu Y_{F,1} + Y_{O_2,2}}, \tag{2.34}$$

where m_1 is the mass of the fuel stream, m_2 is the mass of the oxidizer stream, and ν is the stoichiometric oxidizer-to-fuel ratio. The mixture fraction is a conserved scalar that represents the mass fraction of material originated at the fuel stream. It is a parameter that varies from 1 at the fuel stream to 0 at the oxidizer stream. The inner structure of a flame, i.e., the species mass fraction Y_i and the mixture temperature T are assumed to be dependent on the mixture fraction and time only, $Y_k = Y_k(Z,t)$ and $T = T(Z,t)$. Peters, 1984, showed that species and energy transport equations may be rewritten using the mixture fraction as the independent variable, (see e.g. Poinsot and Veynante, 2005), as

$$\rho\frac{\partial Y_i}{\partial t} = \dot{w}_i + \frac{1}{2}\rho\chi\frac{\partial^2 Y_i}{\partial Z^2} \tag{2.35}$$

$$\rho\frac{\partial T}{\partial t} = \dot{w}_T + \frac{1}{2}\rho\chi\frac{\partial^2 T}{\partial Z^2} \tag{2.36}$$

where χ is the scalar dissipation rate, a parameter that accounts for the local gradient on the physical space of the mixture fraction defined by

$$\chi = 2\frac{\lambda}{\rho c_p}\left(\nabla Z\right)^2 \tag{2.37}$$

where the diffusion coefficient of the mixture fraction was chosen to be the same as the thermal diffusivity of the mixture. This assumption can be justified by remembering that under certain simplifying conditions the energy and mixture fraction transport equations have the same form and boundary conditions [Turns, 2000]. Equations 2.35 and 2.36 are called flamelet equations. The scalar dissipation rate χ is the link between the local flow field and the inner flame structure.

To simulate a multidimensional flame, first the flame structure problem is solved. Several one-dimensional steady counter-flow flames (with prescribed χ) are solved and the results are stored in a table as a function of the mixture fraction and the scalar dissipation rate, i.e., $Y_i = Y_i(Z,\chi)$ and $T = T(Z,\chi)$. Although χ varies along the flame, usually a characteristic value is chosen to parameterize the results, for example the value at the stoichiometric mixture fraction χ_{st}. Then, the three-dimensional flow problem is solved (conservation equations for the total mass and momentum) with an additional conservation equation for the mixture fraction Z. At each point of the domain the state of the system be retrieved from the table based on the local value of Z and χ. The evaluation of χ in multidimensional simulations can be accomplished based on the local flow and Z fields through algebraic approximations.

2.3.4 Flamelet Generated Manifold (FGM)

The FGM was independently proposed by van Oijen and de Goey, 2000, and Gicquel et al., 2000 (the last authors called the method a Flame Prolongation of the ILDM (FPI)). The method combines characteristics of the ILDM and Flamelet methods.

In the FGM method a low dimensional manifold is created from solutions of flamelet equations. Since the reactive system is naturally confined to a sub-region in composition space (as shown by Maas and Pope, 1992), then, in the FGM method the low dimensional manifold is built by following the path in composition space that is covered by the system in an one-dimensional laminar flame. Then, the flamelet equations (for premixed or non-premixed flames) are solved and stored in a table (a manifold) as a function of some controlling variables.

For the controlling variables there is not an unique choice. However, a necessary characteristic is the choice has to result in a unique mapping of the dependent variables. A convenient choice in many situations is a progress variable $\mathcal{Y}$ formed by the combination of some variables, for example

$$\mathcal{Y} = \alpha_{CO_2} Y_{CO_2} + \alpha_{H_2O} Y_{H_2O} + \alpha_{H_2} Y_{H_2}, \tag{2.38}$$

where the weighting factors α_i are given by $\alpha_i = 1/MW_i$. In this way all species in the progress variable have comparable contribution. Since H_2 has a high diffusivity its inclusion in the $\mathcal{Y}$ definition guarantees that $\mathcal{Y}$ has a non-zero value everywhere in the flame.

Here another definition for the mixture fraction is used, which its expressed in terms of the element mass fractions Z_C, Z_H and Z_O as follows [Bilger, 1989]:

$$Z = \frac{Z^* - Z^*_{ox}}{Z^*_{fu} - Z^*_{ox}} \quad with \quad Z^* = 2\frac{Z_C}{M_C} + \frac{1}{2}\frac{Z_H}{M_H} - \frac{Z_O}{M_O} \tag{2.39}$$

where Z_j is the element mass fraction of element j, defined as the mass of element j divided by the total mass, and the subscripts fu and ox denote pure fuel and oxidizer quantities, respectively. The mixture fraction is scaled such that $Z = 1$ in the fuel stream and $Z = 0$ in the oxidizer stream.

As in the ILDM method, the number of controlling variables may be chosen arbitrarily and the fidelity of the reduction technique increases as the number of controlling variables is increased. For example: for laminar premixed adiabatic flames one controlling variable (progress variable $\mathcal{Y}$) is usually sufficient to describe the flame, whereas for non-premixed non-adiabatic flames three controlling variables are needed (progress variable $\mathcal{Y}$, a mixture fraction Z and enthalpy h). In subsequent simulations it is assumed that the thermodynamic state of the system in each point is defined by the controlling variables only and all other parameters can be retrieved from the manifold. For each controlling variable a corresponding conservation equation must be solved in the multidimensional problem.

An advantage of the FGM over the ILDM is that the manifold naturally takes into account convection and diffusion effects (unsteady effects may be included by solving unsteady flamelets). For high temperature regions, where the reactions terms are dominant, the FGM and ILDM have similar behavior. On low temperature regions, however, where diffusion and convection terms may be as important as the reactive terms, the FGM is expected to give a better approximation of the state of the system. Relative to the SLFM approach the FGM method can be improved by including additional controlling variables to the manifold. In Jha and Groth, 2011, it is shown that important improvements are achieved when the FGM is used instead of the SLFM.

2.3.4.1 Flamelet Equations

In de Goey and ten Thije Boonkkamp, 1999, a set of flamelet equations for a flame adapted coordinate system has been derived from the full set of three-dimensional transport equations. Then, the steady one dimensional transport equations for the total mass, the mass of species and enthalpy, for constant Lewis number Le_i, read

$$\frac{\partial(\rho u)}{\partial x} = -\rho K, \tag{2.40}$$

$$\frac{\partial(\rho u Y_i)}{\partial x} = \frac{1}{Le_i}\frac{\partial}{\partial x}\left(\frac{\lambda}{c_p}\frac{\partial Y_i}{\partial x}\right) + \dot{w}_i - \rho K Y_i, \tag{2.41}$$

$$\frac{\partial(\rho u h)}{\partial x} = \frac{\partial}{\partial x}\left(\frac{\lambda}{c_p}\frac{\partial h}{\partial x} + \sum_{i=1}^{N_s} h_i \frac{\lambda}{c_p}\left(\frac{1}{Le_i} - 1\right)\frac{\partial Y_i}{\partial x}\right) - \rho K h, \tag{2.42}$$

where x is the normal coordinate relative to the flame surface, ρ is the mixture density, u is the velocity component normal to the flame surface, K is the stretch rate, Y_i is the mass fraction of species i, λ is the mixture thermal conductivity, c_p is the mixture heat capacity, $\dot{w}_i$ is the reaction rate of species i and h is the mixture enthalpy.

The stretch rate K accounts for the deviations from the one-dimensional condition. In van Oijen and de Goey, 2000, the stretch rate K is defined as the relative rate of change of the mass $M(t)$, defined as

$$M(t) = \int_{V(t)} \rho dV \tag{2.43}$$

contained in an infinitesimal volume $V(t)$ in the flame, moving with the local flame surface velocity u_f, then,

$$K = \frac{1}{M}\frac{dM}{dt}. \tag{2.44}$$

A transport equation for the stretch field $K(x)$ derived from the momentum equation in transverse direction and reads [van Oijen and de Goey, 2000]

$$\frac{\partial(\rho u K)}{\partial x} = \frac{\partial}{\partial x}\left(\mu \frac{\partial K}{\partial x}\right) - \rho K^2 + 2\rho_2 a^2, \tag{2.45}$$

where a and ρ_2 are respectively the applied strain rate and the density at the oxidizer stream. The strain rate a (s^{-1}) is proportional to the local velocity gradient at the oxidizer inlet $(a = -\partial u/\partial x)$. Then, at the oxidizer stream the stretch and strain rates are equal $(K = a)$. The applied strain rate a can be interpreted as the inverse of a residence time scale since for large values of a the species resides less time within the flame and the conversion to saturated products is less complete. For a critical value of the strain rate the flame extinguishes. On the other hand, for small values of a the residence time increases and larger amounts of saturated products are formed. In the limit $a \to 0$ the residence time is infinite and the flame reaches equilibrium.

2.3.4.2 Manifold construction and multidimensional simulations

To build the manifold, the set of conservation Equations 2.40 to 2.45 is solved with proper boundary conditions. The FGM method was first introduced for the solution of multidimensional premixed flames, where a premixed flamelet was the natural choice to build the manifold, since it connects the system initial condition (frozen flow region of a premixed flame) to the equilibrium condition (equilibrium region of a premixed flame). In this case, flame stretch may be included $(K \neq 0)$ or may be neglected $(K = 0)$ when building the manifold.

For diffusion flames both premixed and non-premixed flamelets have been used to create the manifold, Verhoeven, 2011, but the results with the former option has been shown to be superior. A non-premixed flamelet is built from the solutions of laminar counterflow diffusion flames. Then, the stretch rate must be included, since unstretched flames in this configuration are intrinsically unstable [Poinsot and Veynante, 2005]. This is done by varying the applied strain rate a from very low values until the highest value where the extinction limit is achieved. All these solutions are stored in a single table as a function of the controlling variables $\mathcal{Y}$ and Z, forming a 2D manifold. To cover the region between the extinction limit and the mixing limit (when there is no reaction), a series of unsteady flamelets may be used with increasingly higher values of the applied strain rate a.

Usually the flamelet equations are solved for a set of variables that do not change with chemical reactions and are called conserved variables. In general these variables are the pressure (low Mach number approximation) and the element mass fractions Z_j. For the case of adiabatic flames, the enthalpy of the system is another conserved variable. However, one or more of these conserved variables may vary in space or time due to mixing or cooling/heating (i.e., other process than chemical reactions). When the variation of one of the conserved variables is large it has to be included in the manifold as an additional controlling variable.

For multidimensional flame simulations the equations to be solved are the continuity equation, Equation 2.17, the momentum equation, Equation 2.18, and the transport equations for the controlling variables. Then, for the case of a diffusion flame with two controlling variables $\mathcal{Y}$ and Z the following additional transport equations are solved

$$\nabla \cdot (\rho \mathbf{v} Z) = \nabla \cdot \left(\frac{\lambda}{c_p} \nabla Z \right), \tag{2.46}$$

$$\nabla \cdot (\rho \mathbf{v} \mathcal{Y}) = \nabla \cdot \left(\frac{1}{Le_{\mathcal{Y}}} \frac{\lambda}{c_p} \nabla \mathcal{Y} \right) + \dot{w}_{\mathcal{Y}}, \tag{2.47}$$

where $Le_{\mathcal{Y}}$ is and $\dot{w}_{\mathcal{Y}}$ are the Lewis number and source term for the progress variable and both are composed from the Lewis numbers and source terms of the selected species that form $\mathcal{Y}$. Note that the diffusion transport of mixture fraction is considered as $Le_Z = 1$. When building the manifold these parameters may also be tabulated, i.e., $Le_{\mathcal{Y}} = Le_{\mathcal{Y}}(\mathcal{Y}, Z)$ and $\dot{w}_{\mathcal{Y}} = \dot{w}_{\mathcal{Y}}(\mathcal{Y}, Z)$.

For each point in the computational domain the local values of $\mathcal{Y}$ and Z are used to retrieve the the state of the system, i.e., $Y_i = Y_i(\mathcal{Y}, Z)$ and $T = T(\mathcal{Y}, Z)$. This is done by a bilinear interpolation procedure. One efficient option for this procedure is described in van Oijen, 2002. For non-adiabatic flames the enthalpy of the system is not conserved and the multidimensional energy equation, Equation 2.20, must also be solved to account for the heat loss effects. In this case the enthalpy is an additional controlling variable (forming a 3D manifold, i.e., $Y_i = Y_i(\mathcal{Y}, Z, h)$ and $T = T(\mathcal{Y}, Z, h)$). Note that the inclusion of additional controlling variables increases the computational time for the retrieval process as the interpolation procedure becomes more complex. Since for each controlling variable an additional transport equation must be solved, it is expected that the FGM may become slower than the direct integration of the conservation equations for a large number of controlling variables.

2.3.4.3 Progress Variable choice:

The definition of the progress variable is of extreme importance since its choice determines how well the mixture thermodynamic state is mapped. For methane-air premixed and non-premixed flames the choice of $\mathcal{Y} = \alpha_{CO_2} Y_{CO_2} + \alpha_{H_2O} Y_{H_2O} + \alpha_{H_2} Y_{H_2}$ usually renders good results, Nevertheless, when the fuel or oxidant composition are different, a new choice for the progress variable must be made. The choice is arbitrary, usually based on previous experience, or it can be made using automatised methods, like the works of Ihme et al., 2012 , Najafi-Yazdi et al., 2012 and Prüfert et al., 2015. All these works have the same goal: to create a method where the reaction progress variable can be optimised by mathematical optimisation tools, removing the expert knowledge previously required in identifying the optimal $\mathcal{Y}$ [Ihme et al., 2012]. Even though each achieved the goal with different mathematical approach, they shared similar principles as the one suggested by Ihme et al., 2012:

- The definition of $\mathcal{Y}$ should result in a transport equation that can be conveniently solved in a combustion simulation.
- The reactive scalars from which $\mathcal{Y}$ is constructed should all evolve on comparable time scales.
- All parameters that define the manifold should be independent of one another.

- The set of parameters from which the manifold is formed should uniquely characterize each point in the thermochemical state-space.

Since the application of such optimisation procedures is not straightforward, in the present thesis it is chosen just to use the principles presented above to find one arbitrary progress variable that can recover the thermodynamic/chemistry-state with reasonable results and work on the methodology to include high load of soot inside the FGM method.

3 INVESTIGATION OF MASS AND ENERGY COUPLING BETWEEN SOOT PARTICLES AND GAS SPECIES IN MODELING ETHYLENE COUNTERFLOW DIFFUSION FLAMES

In this chapter the mass and energy coupling between the soot particles and the gas-phase species is investigated for ethylene counterflow flames using a semi-empirical model. The semi-empirical model is chosen since it combines important steps for soot formation, good predictability of global soot variables and low computational time, specially for practical combustion systems. In order to determine whether the coupling effect is important, the model is explored in conditions that produce low and high amounts of soot by changing the strain rate imposed to the flow field, by increasing the oxygen concentration of the oxidizer and by increasing the pressure. Adiabatic and non-adiabatic (with radiation losses) simulations are investigated. Additionally, the effect of simplified transport properties modeling is analyzed.

3.1 Numerical model

Combustion problems are modeled with a set of partial differential equations that describes conservation of total mass, mass of species, momentum, and energy. For counterflow flames an one-dimensional approximation can be employed. The derivation of this set of equations can be found in de Goey and ten Thije Boonkkamp, 1999.

3.1.1 Soot model

The soot model used in this study is based on Leung et al., 1991 and Liu et al., 2004. This model is a semi-empirical acetylene based model that describes soot particle nucleation, surface growth and oxidation. Two additional equations are included in the system of conservation equations, one for soot mass fraction, Y_S, and another for soot number density, N_S (*particles* (*kg of mixture*)$^{-1}$). These two equations written for a stagnation flow read

$$\frac{\partial\left(\rho Y_S\right)}{\partial t}+\frac{\partial\left(\rho u Y_S\right)}{\partial x}=-\frac{\partial\left(\rho V_T Y_S\right)}{\partial x}+\frac{\partial}{\partial x}\left(\rho D_s\frac{\partial Y_S}{\partial x}\right)+\dot{w}_{Y_S}-\rho K Y_S, \tag{3.1}$$

$$\frac{\partial\left(\rho N_S\right)}{\partial t}+\frac{\partial\left(\rho u N_S\right)}{\partial x}=-\frac{\partial\left(\rho V_T N_S\right)}{\partial x}+\frac{\partial}{\partial x}\left(\rho D_s\frac{\partial N_S}{\partial x}\right)+\dot{w}_{N_S}-\rho K N_S, \tag{3.2}$$

where ρ is the mixture density ($kg\ m^{-3}$), u is the fluid velocity ($m\ s^{-1}$), V_T is the thermophoretic velocity of the soot particles ($m\ s^{-1}$), D_s is the soot diffusion coefficient ($m^2\ s^{-1}$), $\dot{w}_{Y_S}$ and $\dot{w}_{N_S}$ are the source terms of soot mass fraction ($kg\ m^{-3}s^{-1}$) and soot number density ($particles\ m^{-3}s^{-1}$), respectively, and K is the stretch rate (s^{-1}). The stretch rate K accounts for the deviations from the one-dimensional condition [de Goey and ten Thije Boonkkamp, 1999]. Many researches [Liu et al., 2002, 2004; Leung et al., 1991; Fairweather et al., 1992; Zhang et al., 2008] neglect the Brownian motion of soot particles since soot transport is usually dominated by convective and thermophoretic effects. A small soot diffusion term is retained in this study to enhance numerical stability. In the same manner as in Kennedy et al., 1990, who used a soot diffusivity of 1% of the average gas diffusivity, the value of D_s is set to 1×10^{-6} ($m^2\ s^{-1}$). The thermophoretic velocity of soot, V_T, is modeled as

$$V_T = -0.50 \frac{\mu}{\rho} \frac{1}{T} \frac{\partial T}{\partial x}. \tag{3.3}$$

where μ is the mixture dynamic viscosity ($kg\ m^{-1}s^{-1}$) and T is the mixture temperature (K).

The soot related reactions are presented in Table 3.1. It is a simplified mechanism that neglects many phenomena involved in soot formation. The destruction of particles by coagulation was neglected as sugested in Ezekoye and Zhang, 1997, Liu et al., 2002, and Liu et al., 2004. There is only one species responsible for soot nucleation and surface growth, neglecting the role of many PAHs. Also, the aerosol of particles is assumed to be mono-disperse. Nevertheless, this model is good enough for the purposes of the present work, i.e., to evaluate the importance of the coupling terms between the gas-phase and soot particles.

In this model the first reaction for soot formation is the nucleation of the first particle, which employs acetylene as a representative species of the soot precursors. The soot particle is represented as solid carbon, C_S. The second reaction is the surface growth due to adsorption and reaction of C_2H_2 on the surface of the particle. The third, fourth and fifth reactions model soot mass consumption by surface oxidation by O_2, OH and O, respectively.

The source terms for soot mass fraction, Equation 3.1, and soot number density,

Table 3.1: Soot reactions

Reaction		Rate n.
Nucleation	$C_2H_2 \rightarrow 2C_S + H_2$	R_1
Surf. Growth	$C_2H_2 + nC_S \rightarrow (n+2)\,C_S + H_2$	R_2
Oxid. by O_2	$C_S + \frac{1}{2}O_2 \rightarrow CO$	R_3
Oxid. by OH	$C_S + OH \rightarrow CO + H$	R_4
Oxid. by O	$C_S + O \rightarrow CO$	R_5

Equation 3.2, are:

$$\dot{w}_{Y_S} = M_S\left(2R_1 + 2R_2 - R_3 - R_4 - R_5\right), \tag{3.4}$$

$$\dot{w}_{N_S} = \frac{2}{C_{min}} N_A R_1, \tag{3.5}$$

where $M_S = 12.011$ ($kg\ kmol^{-1}$) is the carbon molar mass, $C_{min} = 700$ is the average number of carbon atoms in the incipient soot particle and $N_A = 6.022 \times 10^{26}$ ($particles\ kmol^{-1}$) is Avogadro's number. Equation 3.4 takes into account soot nucleation, surface growth and oxidation by O_2, OH and O. Equation 3.5 takes into account the production of particles by soot nucleation only.

The nucleation rate R_1 ($kmol\ m^{-3}\ s^{-1}$), and its rate constant k_1 are written as

$$R_1 = k_1(T)[C_2H_2], \quad k_1 = 1.0 \times 10^3 \exp\left(\frac{-16,103}{T}\right) \tag{3.6}$$

where $[C_2H_2]$ is the acetylene concentration ($kmol\ m^{-3}$).

The surface growth rate, R_2 ($kmol\ m^{-3}\ s^{-1}$), and its rate constant k_2 are written as

$$R_2 = k_2(T)f(S)[C_2H_2], \quad k_2 = 7.0 \times 10^2 \exp\left(\frac{-10,064}{T}\right), \tag{3.7}$$

where $f(S)$ is a function that expresses the dependence of the surface growth term on the specific soot surface area, S ($m^2\ m^{-3}$). In this model $f(S) = \sqrt{S}$ and $S = \pi d_p^2\,(\rho N_S)$. The soot particle diameter, d_p (m), can be obtained as

$$d_p = \left(\frac{6Y_S}{\pi \rho_C N_S}\right)^{1/3}, \tag{3.8}$$

where $\rho_C = 1,900$ ($kg\ m^{-3}$) is the soot density.

The oxidation by O_2 is based on the Nagle-Strickland-Constable model (NSC) [Nagle and Strickland-Constable, 1962]. In this model, it is assumed that there are two types of sites, one more reactive (A) and another less reactive (B), on the carbon surface. The oxidation rate, R_3 ($kmol\ m^{-3}\ s^{-1}$), and its rate constant k_3 are written as

$$R_3 = k_3 S, \quad k_3 = \left(\frac{k_A P_{O_2}}{1 + k_Z P_{O_2}} \right) x_A + k_B P_{O_2} (1 - x_A), \tag{3.9}$$

where P_{O_2} is the partial pressure of O_2 in atm, and the intrinsic constant rates of the model, k_A, k_Z, k_B and k_T, and the fraction of the surfaces x_A that is covered by the sites A are

$$k_A = 200 \exp(-15,098/T), \tag{3.10}$$

$$k_Z = 21.3 \exp(2,063/T), \tag{3.11}$$

$$k_B = 4.46 \times 10^{-2} \exp(-7,650/T), \tag{3.12}$$

$$k_T = 1.51 \times 10^{6} \exp(-48817/T), \tag{3.13}$$

$$x_A = \left(1 + \frac{k_T}{k_B P_{O_2}} \right)^{-1}. \tag{3.14}$$

The oxidation rate by the OH radical R_4 ($kmol\ m^{-3}\ s^{-1}$) and its rate constant k_4, taken from Moss et al., 1995, are written as

$$R_4 = k_4 S, \quad k_4 = 1.044 \times 10^{-3} \varphi_{OH} T^{-1/2} p_{OH} \tag{3.15}$$

where φ_{OH} is the collision efficiency for OH and p_{OH} is the OH partial pressure in Pa. The collision efficiency is assumed to be equal to 0.2.

The oxidation rate R_5 by the O radical and its rate constant k_5, taken from Bradley et al., 1984, are written as:

$$R_5 = k_5 S, \quad k_5 = 1.094 \times 10^{-3} \varphi_O T^{-1/2} p_O \tag{3.16}$$

where φ_O is the collision efficiency for O and p_O is the O partial pressure in Pa. The collision efficiency is also assumes to be equal to 0.2.

The soot volume fraction, f_v, is found from the computed soot mass fraction as

$$f_v = \frac{\rho Y_S}{\rho_C}. \tag{3.17}$$

The soot model described above is not valid for very large residence times, i.e., for extreme low strain rates. Since the model does not consider reversible reactions, it is not able to reach the equilibrium conditions and very large quantities of soot are predicted. This limitation was also pointed out in Kennedy, 1997, and Eaves et al., 2015. Eaves et al., 2015, showed that considering the reversibility in modeling soot nucleation and condensation processes the agreement of numerical studies with experimental data of ethylene laminar coflow flames improved.

3.1.2 Radiation model

The radiant heat losses are modeled by using the grey-gas approximation, i.e., there is no dependence on the wave number, and the optical thin limit, i.e., the medium does not scatter nor absorb radiation. Then, the heat source in the energy conservation equation due to gas and soot radiant heat losses [Smooke et al., 1999; Barlow et al., 2001; Carbonell et al., 2009; Domenico et al., 2010] is:

$$\dot{q_R'''} = \dot{q_{R,gas}'''} + \dot{q_{R,soot}'''}, \tag{3.18}$$

$$\dot{q_{R,gas}'''} = -4\sigma\kappa(T^4 - T_{sur}^4), \tag{3.19}$$

$$\dot{q_{R,soot}'''} = -Cf_vT^5, \tag{3.20}$$

where T_{sur} is the surrounding temperature, σ is the Stefan-Boltzmann constant ($5.669 \times 10^{-8}\ W\ m^{-2}K^{-4}$) and the constant $C = 4.243 \times 10^{-4}$ ($W\ m^{-3}K^{-5}$) is taken from Smooke et al., 1999. $\kappa = \sum p_{i,atm}\kappa_i$ denotes the Planck mean absorption coefficient of the mixture (m^{-1}), and $p_{i,atm}$ and κ_i are respectively the partial pressure (atm) and Planck mean absorption coefficient of species i ($atm^{-1}\ m^{-1}$). The participant gas species are H_2O, CO_2, CO and CH_4. The Plank mean absorption coefficient for H_2O and CO_2 are taken from Chen et al., 1993, and for CO and CH_4 are taken from in TNF, 2016. Both set of Plank mean absorption coefficient are presented in the Appendix A. In the Equation 3.20 it is considered that the absorption term is negligible when compared to the emission term. Since in our results there is no soot in low temperature regions, this approximation is accurate enough for the present study.

3.1.3 Coupling of soot and gas-phase species

The solid phase is modeled as an additional species, the $(N + 1)th$ species in the mixture ($Y_{N+1} = Y_S$). The interaction between the soot chemistry and the gas-phase chemistry was accounted for in the transport equations for the total mass, for the mass of species and for energy. This means that additional source terms for species related to soot formation and oxidation (C_2H_2, H_2, CO, H, O_2, OH and O) are added to the system of equations. Thus, the elements are conserved, the summation of species mass fractions is equal to one ($\sum_{i=1}^{N+1} Y_i = 1$) and the summation of species source terms (in mass basis) is equal to zero ($\sum_{i=1}^{N+1} \dot{w}_i = 0$). To guarantee mass conservation the correction of diffusion fluxes is applied to all species, including soot. Additional soot terms in the mixture enthalpy and heat capacity are added as $h = \sum_{i=1}^{N+1} Y_i h_i$ and $c_p = \sum_{i=1}^{N+1} Y_i c_{p_i}$. The thermodynamic properties for soot (h_i and c_{p_i}) are approximated using the properties of solid carbon (graphite) and the data are taken from the NIST-JANAF database [Chase Jr., 1998]. For simplicity it is assumed that soot does not affect the mixture viscosity and thermal conductivity. An additional term in the energy flux, j_q ($kJ\ m^{-2}\ s^{-1}$), due to the soot thermophoretic diffusion flux, the $(N+1)th$ species, is added:

$$j_q = -\lambda \nabla T + \sum_{i=1}^{N+1} h_i j_i, \tag{3.21}$$

where, λ is the thermal conductivity ($kW\ m^{-1} K^{-1}$), j_i is the species i mass diffusion flux ($kg\ m^{-2}\ s^{-1}$). The mixture density, ρ, is calculated as the density for multiphase flows according to Crowe, 2006:

$$\rho = f_v \rho_C + (1 - f_v)\rho_{gas}, \tag{3.22}$$

where the density of the gas phase, ρ_{gas}, is calculated by the ideal-gas equation of state using low-Mach number approximation

$$\rho_{gas} = \frac{pMW_{gas}}{RT}, \quad MW_{gas} = \left(\sum_{i=1}^{N} \frac{Y_i^*}{MW_i} \right)^{-1}, \tag{3.23}$$

where $p = p_{amb}$ is the ambient pressure (Pa), R is the universal gas constant (8.3144 $J\ mol^{-1}\ K^{-1}$), MW_{gas} is the molar mass of the gas-phase only ($kg\ kmol^{-1}$) and MW_i is the species i molar mass. To calculate MW_{gas} it is necessary to rescale the species mass fraction according to $Y_i^* = Y_i/(1 - Y_S)$.

3.1.4 Numerical Method

The system of equations was solved with the code CHEM1D, 2016, for steady state conditions. The chemical kinetic mechanism of Blanquart et al., 2009, was used. This chemical mechanism, consisting of 148 species and 928 reactions, was developed for the high temperature combustion of a wide range of pressures for hydrocarbon fuels ranging from methane to iso-octane. The diffusion coefficients are calculated through the mixture-average approach in which the diffusion velocity of each individual gas species is computed assuming Fick-like diffusion with correction of diffusion fluxes for all species. Viscosity is calculated through Wilke's approximation (Equation 2.10) and thermal conductivity is calculated through combination-averaging approach of Mathur et al., 1967 (Equation 2.12).

The fuel stream is pure ethylene and the oxidizer stream has the simplified composition of standard dry air ($Y_{O_2} = 0.233$ and $Y_{N_2} = 0.767$). All cases converged using a convergence criteria of 1×10^{-10}. Adaptive mesh refinement was used according to the gradients of the following variables: temperature, density, heat release, Y_S, N_S, $Y_{C_2H_2}$, Y_O and Y_H. The distance of both boundaries to the stagnation plane are set as $x_{left} = -2$ cm and $x_{right} = 2$ cm, sufficiently large for all gradients near the boundaries to become zero, except for velocity, that follows a potential flow. It was found that the results for all variables analyzed in the current work became grid independent for 400 points.

An assessment of the current model was done and the results of three non-adiabatic cases were compared to the experimental work of Hwang and Chung, 2001, and Vandsburger et al., 1984, and the numerical work of Liu et al., 2004. The chemical kinetic mechanism used for this assessment was GRI v3.0 [Smith et al., 2000], the same as for the reference. Figure 3.1 shows the comparison of f_v for three levels of oxygen concentration at the oxidant stream. The comparison with experiments was in good qualitative agreement and the differences observed in the numerical comparison are due to the different reacting flow codes that were used (the reference used the code described in Smooke et al., 1988).

3.2 Results and Discussion

The impact of the mass and energy coupling terms on the flame simulation are evaluated for ethylene/air counterflow flames in a variety of conditions. Results are presented in four parts. In the first part some basic aspects of the flame structure are presented for low and high values of strain rate. In the second part different radiation models are compared and discussed, highlighting the importance of this coupling term for soot predictions.

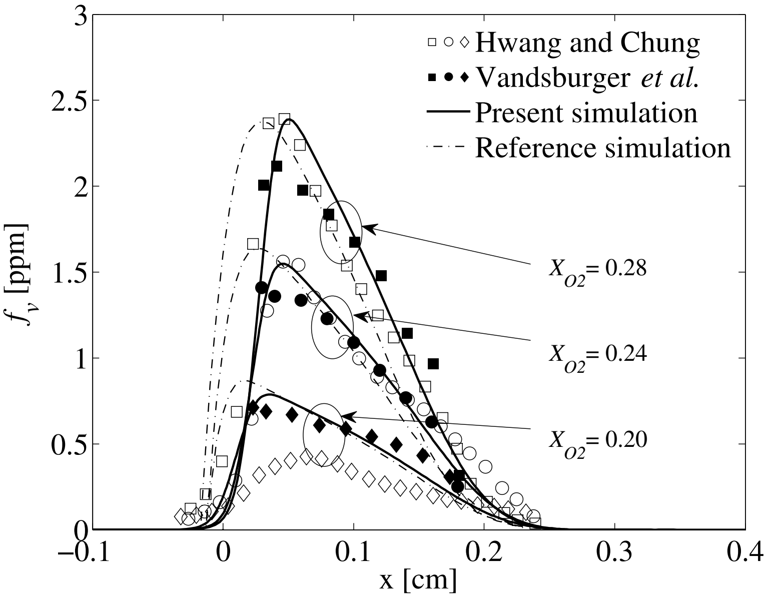

Figure 3.1: Comparison of f_v results for three levels of oxygen molar fraction at the oxidizer stream, X_{O_2}; Open symbols: Hwang and Chung, 2001, Close Symbols: Vandsburger et al., 1984; Solid line: Present simulation; and Dash-dot line: Reference simulation [Liu et al., 2004].

In the third part, additional coupling terms for mass and thermodynamic properties are explored in detailed in order to determine the conditions for which the full coupled model is necessary. Numerical simulations were conducted for four different situations. Two simulations were adiabatic and two were non-adiabatic (i.e., with radiant heat losses, Equation 3.18). Within each heat loss condition two different cases were tested. In the first case, here called "coupled", the gas-phase composition and thermodynamic properties are influenced by the soot formation and oxidation, with the additional terms presented in the Section 3.1.3. In the second case, here called "non-coupled", the gas-phase composition and thermodynamic properties are not influenced by the soot formation and oxidation (none of the additional terms presented in the Section 3.1.3 are used), and the only coupling effect that is kept is the radiant heat losses from soot in the energy equation. Therefore, there are no conservation of mass and energy and that the mixture density is evaluated only by the gas-phase.

In the last part, the effect of different transport models on the flame simulation is presented and compared to the effect of coupling terms.

3.2.1 Flame Structure

The impact of flow field on the flame structure for two different values of strain rate, $a = (-du/dx)_{x\to\infty}$, applied at the oxidizer side, is presented. One flame has $a = 100\ s^{-1}$, i.e., a small residence time that leads to a low f_v, and the other has $a = 10\ s^{-1}$, i.e., a long residence time that leads to a high f_v.

The flame structure for $a = 100\ s^{-1}$ for the adiabatic and coupled case is presented in Figure 3.2. Species related to soot production and oxidation and temperature profiles are presented in physical space. The gas stagnation plane is located at $x = 0\ cm$ and the reaction zone is located in the oxidizer side. Soot particles are present in the region where high temperatures and high acetylene concentrations are found. For this condition, the maximum f_v is equal to 0.225 ppm (corresponding to a maximum Y_S of 0.0013).

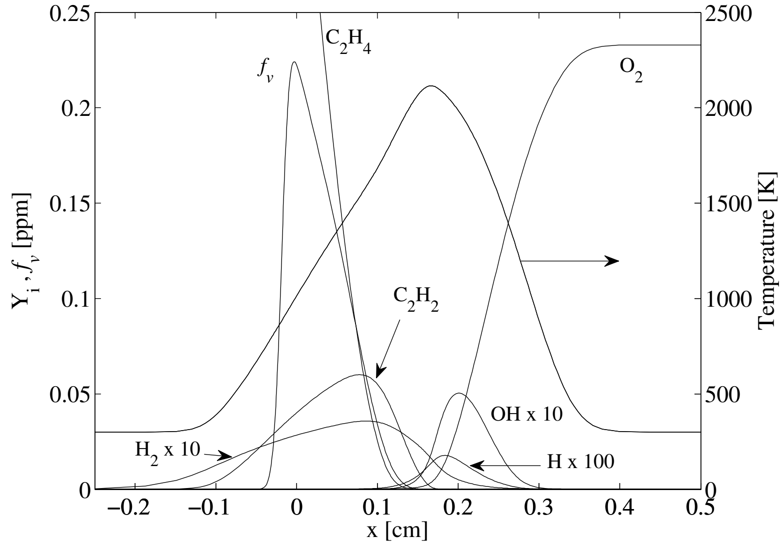

Figure 3.2: Flame structure for $a = 100\ s^{-1}$ for coupled, adiabatic case.

As the residence time is increased the flame thickness and the amount of soot produced are also increased. The f_v and the temperature profiles for $a = 10\ s^{-1}$ for the four situations under investigation are plotted in Figure 3.3. In this figure it is possible to observe that the inclusion of the radiation model is important for the flame simulations while the additional coupling terms have a lower impact. Qualitatively the profiles are similar for the four situations under investigation. The largest differences are usually found close to the maximum value of each variable. Thus, in the discussions that follow, only the differences in the peak values of each variable of interest will be presented.

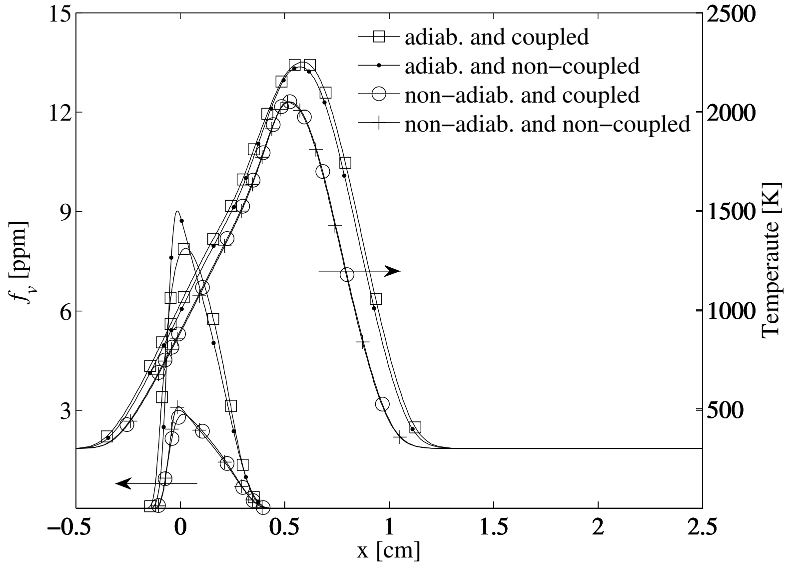

Figure 3.3: f_v and temperature for $a = 10\ s^{-1}$.

3.2.2 Coupling through radiative heat losses

From the previous section it was found that the coupling of radiative heat loss had a large impact on the flame structure. Therefore, in this section, the heat loss by soot and gas radiation is discussed in more detailed. Numerical simulations were conducted for four different radiation models. One simulation was adiabatic, one with soot radiation only, another with gas radiation only and the last with both soot and gas radiation (previously referred to as the non-adiabatic condition). All simulations were done using the coupled approach, with the terms presented in the Section 3.1.3. To explore a large range of soot volume fractions the strain rate, a, is varied from 1 s^{-1} to 200 s^{-1}.

Figure 3.4 presents the maximum temperature as a function of the strain rate a. As the residence time increases (a decreases) the effect of radiative heat loss becomes so significant that the flame is eventually extinguished. It is also possible to see that as the amount of soot increases (see Figure 3.5) the soot radiation becomes important and generates a similar decrease of the flame temperature as that observed for the gas-phase radiation model. An important aspect is that soot radiation source term is concentrated in the region of high soot volume fraction (close to the stagnation plane). In this region the predicted temperature is lower for the model considering only soot radiation when

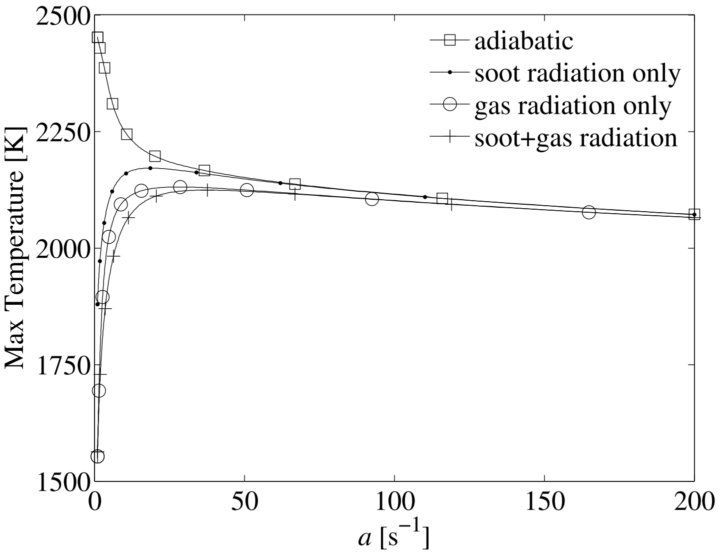

Figure 3.4: Comparison of maximum temperature for different radiative heat losses as a function of the strain rate a.

compared to that considering only gas radiation. The opposite is observed for the maximum flame temperature as seen in Figure 3.4, since the gas radiation source term is important in a much wider region.

In the Figure 3.5 it is possible to see that the maximum soot volume fraction is differently affected by each heat loss condition. The maximum values of f_v are 5.74, 8.28, and 3.15 ppm, for the soot radiation only, gas radiation only and the combined soot and gas radiation conditions, respectively. This is due to the fact that each condition distinctly affects the flame structure, resulting in unique temperature and gas species fields, which consequently produces a unique soot distribution. If no radiation is accounted for, the model predicts huge amounts of soot that are not realistic as will be seen in the next section.

In general, the importance of the radiation heat loss on soot predictions shown here agrees with others works in the literature. For example, in the work of Kennedy et al., 1996, the comparison between adiabatic and non-adiabatic solutions showed that the concentration drop of OH and other gas species was due to temperature decrease (due to soot radiation) and mass coupling terms. The same conclusion is reached with the present results. Domenico et al., 2010, found small differences in C_2H_2 and C_6H_6 when the soot radiation was accounted for, for partially premixed ethylene case. For the present

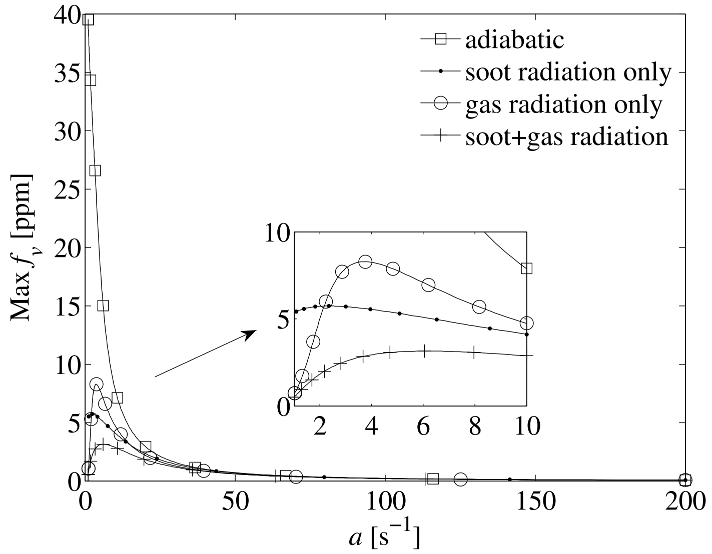

Figure 3.5: Comparison of maximum f_v for different radiative heat losses as a function of the strain rate a.

ethylene diffusion flame differences were found for C_2H_2 and C_6H_6, equal to 2.5% and 5%, respectively, for similar soot amounts. Wang et al., 2015, studied ethylene counterflow with the oxidizer stream composed of 25% O_2 and 75% N_2 by volume and the fuel stream of pure ethylene. In a comparison between a gas-phase model and a model with soot (mass and radiation coupling terms) they found that the coronene (pyrene) concentration was reduced by 30.5% (10%). For the same level of soot, $f_{v,max} = 0.6\ ppm$, but with oxidizer being dry air, the present results showed that the pyrene concentration was reduced by 10.8% (the employed mechanism does not have coronene).

3.2.3 Coupling through mass terms and thermodynamic properties

In this section additional coupling efffects including mass and thermodynamic properties, presented in Section 3.1.3, are investigated. The effects of strain rate, oxygen content of the oxidizer stream, and pressure are also evaluated.

Strain rate effect

In order to determine whether the full coupling is important, the error between coupled and non-coupled models is analysed. It was found that this error becomes notice-able mostly in the range $10 < a < 100\ s^{-1}$. Therefore, this range is used for discussing the following results.

As shown in Figure 3.6, within the range of strain rate values explored in this section, only small differences in temperature predictions are found when the coupling terms are not included in the model. The largest absolute temperature difference is only 24 K for the adiabatic condition while for the non-adiabatic condition it is 5 K. In terms of relative difference (with the coupled case as the reference and values presented in modulus) it is 1.09 % and 0.25 % for the adiabatic and non-adiabatic conditions, respectively. The effect of radiative heat losses, on the other hand, is very important and this effect is larger for the lower strain rates with the difference reaching approximately 200 K at $a = 10\ s^{-1}$.

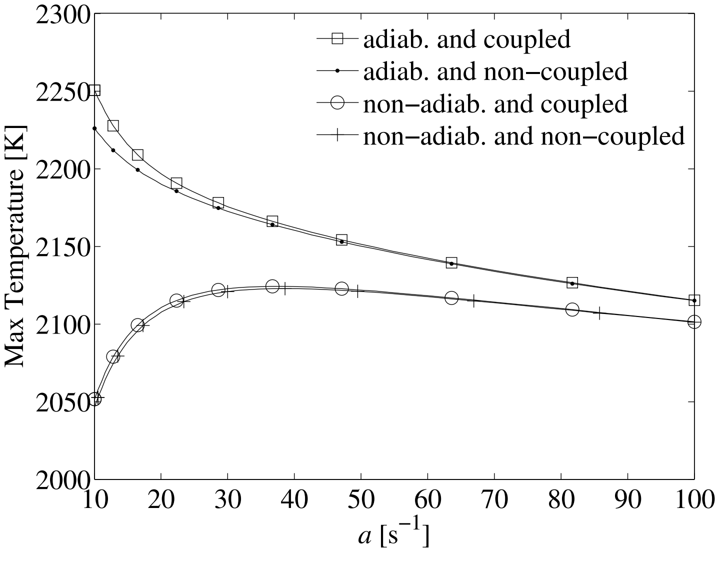

Figure 3.6: Maximum temperature as a function of the strain rate a.

The maximum f_v as function of strain rate is shown in Figure 3.7. As the residence time is increased (lower a) more soot is produced, reaching maximum values of f_v equal to 7.89 ppm and 2.88 ppm for the adiabatic and non-adiabatic conditions, respectively, at $a = 10\ s^{-1}$. The coupling effect becomes more significant for lower a values due to the higher amounts of soot formed. To evaluate the mass and energy coupling between both phases, only the relative difference between the non-coupled and coupled cases is discussed. For the adiabatic condition the relative difference for the maximum f_v steadily increases from 0.1 % for the highest a value to 14.3 % for the lowest a value. One can define a threshold for errors larger than 1% (5%), which is found at $a = 60.5\ s^{-1}$ ($23.3\ s^{-1}$), corresponding to a maximum f_v of 0.51 *ppm* (2.34 *ppm*). For the non-adiabatic condition the relative difference increases from 0.1 % for the highest a to 8.2 % for the lowest a value. Relative differences larger than 1%(5%) are found for 0.51 *ppm* (1.9 *ppm*). Figures 3.6 and 3.7 show again that the flame radiation is very important for soot modeling if low strain rate are achieved. For the present study the adiabatic condition overpredicted f_v approximately by a factor of three.

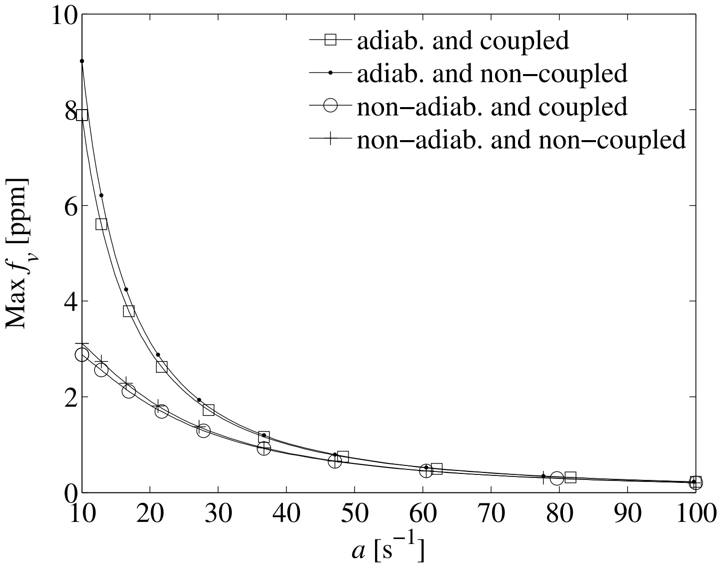

Figure 3.7: Maximum f_v as a function of the strain rate a.

In the Figure 3.8 the soot prediction, in terms of mass fraction, is extended to lower strain rates to show some limitations of different modeling approaches. As the residence time increases, the soot mass presents a steep increase for the adiabatic case, reaching unphysical values for the non-coupled case, which is a severe limitation of this case. When the mass coupling is correctly accounted for, the results are more consistent even for the high soot loads achieved in adiabatic calculations. For the non-adiabatic solution, soot formation is limited by the resulting lower temperatures. For large residence times Y_S even decreases due to the intense radiative heat losses (T decreases) and both coupled and non-coupled models present similar results. However, for large residence times, tending to equilibrium, the employed soot model is not valid since reverse reactions are neglected. A critical point if one decides not to take into account the mass coupling is that the total mass conservation will not be satisfied and the resulting error is equal to the mass of soot formed. For example, for $a = 10\ s^{-1}$, Y_S is 0.051 for the adiabatic condition and 0.016 for non-adiabatic condition, i.e., errors of 5.1% and 1.6%, respectively, in the local mass conservation.

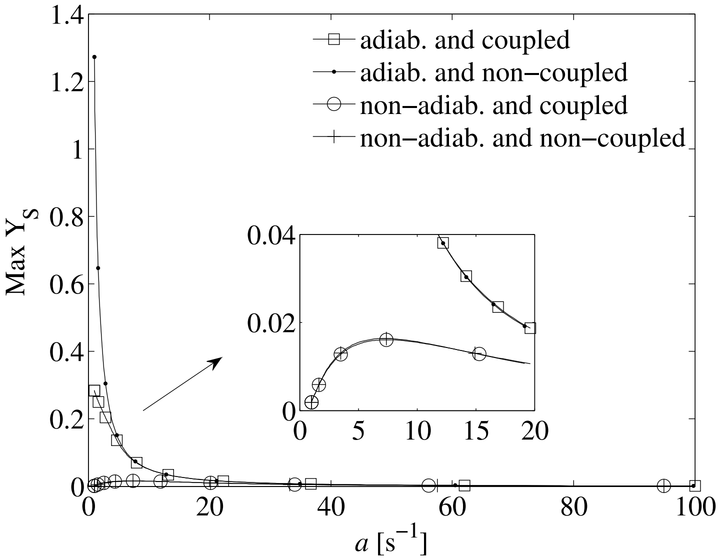

Figure 3.8: Maximum Y_S as a function of the strain rate a.

The impact of the coupling terms on the gas-phase species is also investigated. Only the species responsible for soot nucleation (R_1) and surface growth (R_2), C_2H_2, and the gas-phase product of these reactions, H_2, are presented in detail.

Figure 3.9 presents the maximum C_2H_2 mass fraction. The relative difference varies from small values at the highest a, 0.2% for both adiabatic and non-adiabatic conditions, to significant values for the lowest a, 6.7% for adiabatic and 4.2% non-adiabatic conditions, with the non-coupled cases always presenting higher amounts of C_2H_2. These results are expected, since C_2H_2 is not consumed in reactions R_1 and R_2 for the non-coupled cases. The behavior of C_2H_2, the soot precursor species in the present model, is defined by a balance between the gas-phase reactions forming and consuming acetylene and, for the coupled cases, the consumption by soot nucleation and surface growth. This balance depends on temperature and residence time. For strain rates larger than 170 s^{-1} (not shown in the figure), the acetylene mass fraction is reduced until the flame reaches the extinction limit. The behavior for large strain rates is controlled by the small residence times of these flames. For small strain rates, the acetylene mass fraction is also reduced for all cases, even for the adiabatic and non-coupled case for which the C_2H_2 starts to decrease at a strain rate equal to 7.4 s^{-1} (not shown in the figure). In this circumstance, tending to the adiabatic equilibrium, the C_2H_2 is more consumed than formed as the strain rate is decreased. For non-adiabatic flames, the radiative heat losses become increasingly important for small strain rates, reducing the flame temperature, which also affects the C_2H_2 formation. For intermediary strain rates shown in Figure 3.9, temperature and residence time effects are important for all cases, while soot nucleation and surface growth are also important for the coupled cases.

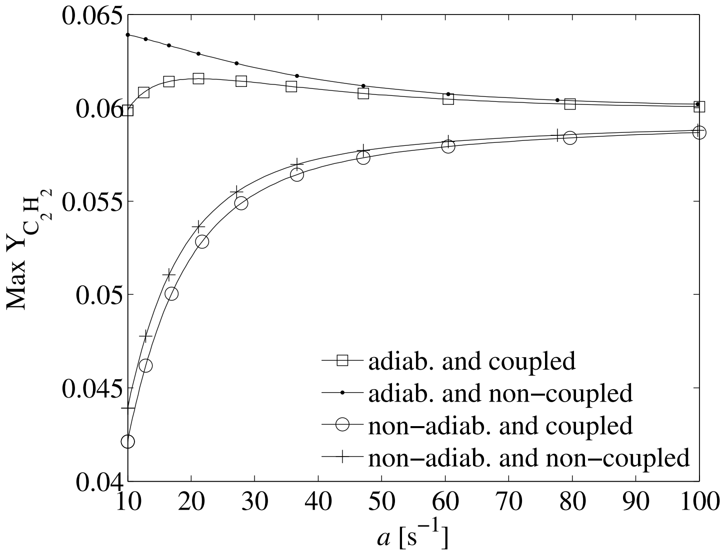

Figure 3.9: Maximum C_2H_2 mass fraction as a function of the strain rate a.

In terms of maximum H_2 mass fraction, shown in Figure 3.10, the relative difference varies from small values for the highest a, 0.7% for both adiabatic and non-adiabatic conditions, to large values for the lowest a, 21.6% for adiabatic and 9.6% non-adiabatic conditions. A consequence of this result is that, since H_2 diffuses faster than the other species, the coupling may imply an increase of preferential diffusion effects.

A summary of the above results is presented in Table 3.2. It shows critical soot volume fraction, and the corresponding critical soot mass fraction, above which a certain level of error is reached (1% and 5%) for some variables when the mass/thermodynamic property coupling effect is not taken into account for the non-adiabatic condition, only. The outcome of changing the oxidant composition and system pressure are also reported in the table and will be discussed later.

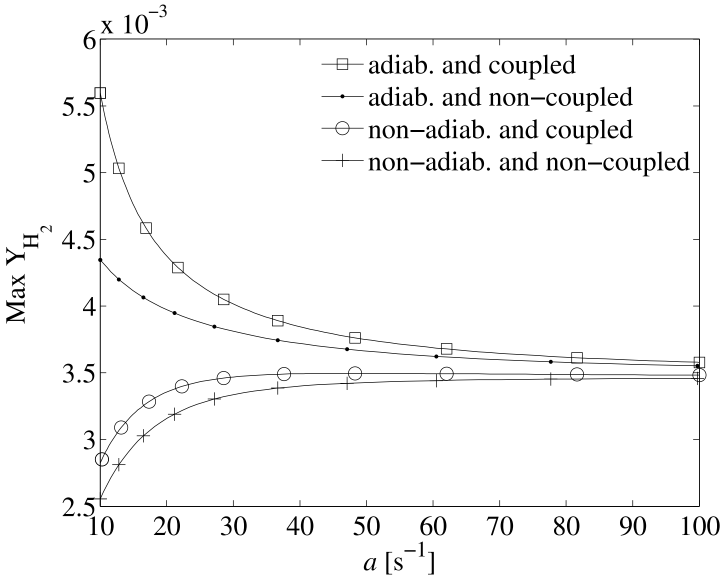

Figure 3.10: Maximum H_2 mass fraction as a function of the strain rate a.

The results, for the strain rate effect, presented in Table 3.2 show that, within the explored limits of soot, the error between coupled and non-coupled did not reach 1% for the the predictions of flame temperature, N_S, O, CO and $Y_{C_6H_6}$. Nonetheless, the coupling changes the prediction of f_v, Y_S and other gas species. The most sensitive gas species identified was H_2, with the lower threshold of 1% found in $f_{v,crit} = 0.31\ ppm$ ($Y_{S,crit} = 0.0017$). The non-coupled model could not represent the correct soot mass fraction with an error lower than 1%. However, when the higher threshold of 5% is analyzed, the discrepancy of most of the variables does not reach that limit, except for f_v, H_2 and H_2O, with H_2 being the most sensitive with the lower threshold found in $f_{v,crit} = 1.64\ ppm$ ($Y_{S,crit} = 0.0089$).

Oxygen and pressure effect

Even for small residence times (high a) the soot production may be large if the oxygen content of the oxidant stream is increased due to the higher temperatures found in such flames. Thus, a new set of simulations is carried out for $a = 80\ s^{-1}$ with the oxygen content in the oxidant stream varying from 21% to 45% on volume basis. This range of oxygen content was choose in order to achieve comparable amounts of soot as the ones found in the strain rate effect study ($0.0016 < Y_{S,max} < 0.016$). The main results

Table 3.2: Critical soot volume fraction, $f_{v,crit}$ in *ppm*, and the corresponding critical soot mass fraction, $(Y_{S,crit})$, found for $0.0016 < Y_{S,max} < 0.016$, for errors equal to or larger than 1% and 5% in the non-adiabatic non-coupled case according to strain rate, oxygen content and pressure effects. The dash indicates that the error is bellow the respective threshold.

	Strain rate effect		Oxygen content effect		Pressure effect	
Variable	1%	5%	1%	5%	1%	5%
f_v	0.51 (0.0029)	1.90 (0.0108)	0.49(0.0030)	1.11(0.0079)	-	-
Y_S	all range > 1%	-	all range > 1%	1.59(0.0125)	all range > 1%	-
N_S	-	-	-	-	-	-
T	-	-	-	-	-	-
$Y_{C_2H_2}$	1.07 (0.0059)	-	1.46(0.0112)	-	2.80(0.0060)	-
Y_{H_2}	0.31 (0.0017)	1.64 (0.0089)	0.32 (0.0018)	-	0.21 (0.0018)	6.54 (0.0083)
Y_H	1.03 (0.0057)	-	-	-	4.20(0.0071)	-
Y_O	-	-	-	-	-	-
Y_{OH}	0.96 (0.0053)	-	-	-	3.05(0.0062)	-
Y_{CO}	-	-	-	-	-	-
Y_{CO_2}	0.91(0.0053)	-	-	-	1.85(0.0050)	-
Y_{H_2O}	0.65(0.0038)	3.06 (0.0154)	0.96(0.0067)	-	0.85(0.0035)	-
$Y_{C_6H_6}$	-	-	1.21(0.0089)	-	12.65(0.0109)	-

are presented in Table 3.2. As for the strain the rate effect, the interaction between both phases does not alter the predictions of flame temperature, N_S, H, O, OH, CO and CO_2. For all gas-species the discrepancies for not coupling the mass and thermodynamic properties between the two phases are below 5%, but for soot mass and volume fraction. Here again, the H_2 is the most sensitive gas species, with the lower threshold of 1% found in $f_{v,crit} = 0.32$ *ppm* ($Y_{S,crit} = 0.0018$). The error for maximum Y_S non-coupled predictions is also larger than 1%. f_v was the first parameter to deviate more than 5% ($Y_{S,crit} = 0.0079$) from the coupled case. Note that changing the oxidant composition resulted in a change on the threshold limits, leading to the conclusion that the importance of the coupling effect is composition dependent.

The pressure effect is also investigated and the same method is applied for finding the limit values for pressure. Thus a new set of simulations was carried out for $a = 60$ s^{-1}, where the pressure was varied from 0.5 *atm* to 30 *atm*. With the increase of pressure the maximum temperature and therefore the soot being formed increased. Results for the pressure effect are to some extend similar to those obtained for the strain rate effect when compared in mass basis ($Y_{S,crit}$). Comparisons for f_v were affected by variations in density (see Equation 3.17). Thus, in this case, it is preferable to use Y_S for evaluating the coupling effect. Note that f_v does not reach errors greater than 1%, and that now benzene is affected by the soot mass coupling. As in the strain rate effect, the lowest threshold for coupling the soot terms are based on the H_2 species, with values of $Y_{S,crit}$ equal to 0.0018(0.0083) for errors larger than 1%(5%).

From the results presented above it is possible to see that there is a certain coherence among $Y_{S,crit}$ among the explored effects. Thus, within the limits of the present study, one can propose that Y_S close to 0.002 could be a reference value for the choice of the full coupling model. For $Y_S \geq 0.002$ local errors larger than 1% will be present if the mass coupling is not taken into account. For a 5% threshold a similar reference would be $Y_S \geq 0.008$. However, these reference values are not universal, but depend on the fuel type, oxidant composition, and, possibly, two-dimensional effects.

3.2.4 Transport properties effect

A common approach to reduce the time required to evaluate multicomponent transport properties in flames is to calculate the diffusion coefficients for the gas species as-

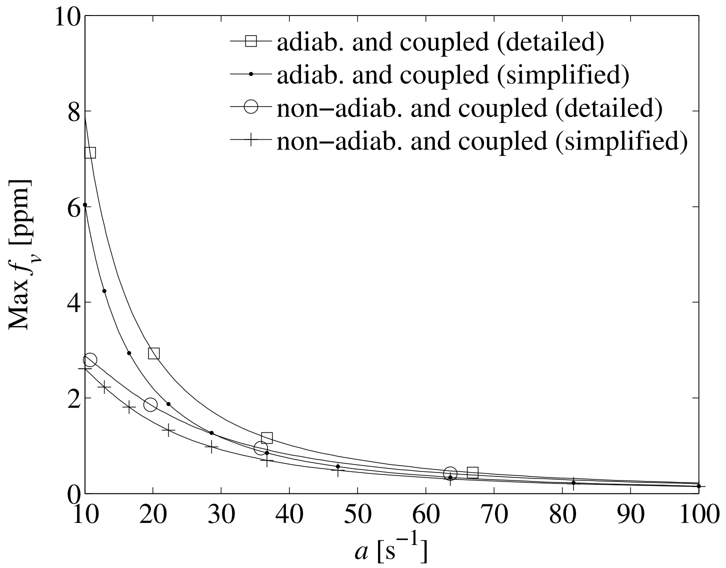

Figure 3.11: Comparison of maximum f_v for different transport properties approaches as a function of the strain rate a.

suming unitary Lewis Number ($Le_i = {}^{\lambda}/_{\rho c_p D_i^M} = 1$). Additionally, simplified formulations are frequently used for other properties. In this section, those proposed in Smooke and Giovangigli, 1991 are employed: $\lambda/c_p = 2.58 \times 10^{-5}\,(T/298)^{0.69}$ (W m^{-1} K^{-1}) and $\mu/c_p = 1.67 \times 10^{-8}\,(T/298)^{0.51}$ (kg m^{-1} s^{-1}). The effect of such simplifications are evaluated and compared to the coupling effects. The strain rate was varied (from 10 s^{-1} to 100 s^{-1}), at atmospheric conditions, and the maximum values for some variables were analyzed.

With these simplifications the flame and the soot coupling effect presented a qualitatively similar behavior when compared to the simulation using the more detailed approach. The H_2 still is the most sensitive gas species with $Y_{S,crit} = 0.0013$ (0.0067) for 1% (5%) of relative error. However the prediction of soot formation is lower for the simplified model. A comparison with the detailed transport model is shown in Figure 3.11 for the coupled cases, only. Notice that at the lowest strain rate the soot formation is reduced by 1.85 *ppm* (23.5%) in the adiabatic condition and by 0.18 *ppm* (6.5%) in the non-adiabatic condition, when the simplified approach is employed.

For maximum temperature profiles the relative difference due to coupling effects also did not reach 1% for both heat loss conditions. Nevertheless the temperature of the flames significantly increased for all cases when using the simplified transport approach

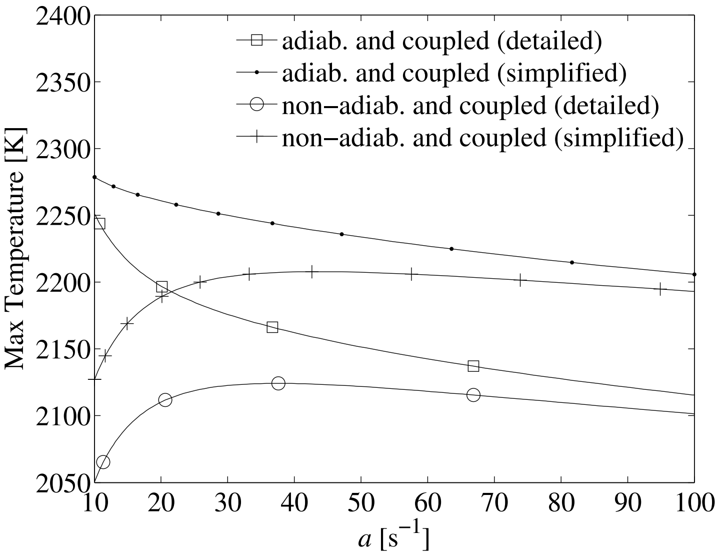

Figure 3.12: Comparison of maximum temperature for different transport properties approaches as a function of the strain rate a.

when compared to the detailed transport model as can be seen in Figure 3.12. Notice that at the highest a the temperature is increased by 90 K (4.3%) for both heat loss conditions, while at the lowest a the temperature is increased by 28 K (1.2%) for the adiabatic condition and by 76 K (3.7%) for the non-adiabatic condition.

The comparison between the simplified and the detailed transport models showed that discrepancies in the predictions of temperature, species and soot, were larger than those found by not taking the mass and thermodynamic properties coupling effects into account. Thus, the choice of the transport model has a more important impact on soot predictions then the full coupling between the phases.

3.3 Conclusions

In this study a numerical model was developed aiming at investigating soot formation in different conditions for an ethylene counterflow diffusion flame. In order to assess modeling limitations the mass and energy coupling between soot solid particles and gas-phase species are investigated and quantified. A semi-empirical two equation model is chosen for predicting soot mass fraction and number density. The model describes particle nucleation, surface growth and oxidation. For the gas-phase a detailed kinetic mechanism is considered. Additionally the effect of considering gas and soot radiation heat losses is evaluated in the optically thin limit approximation.

Simulations were done for a range of conditions that produce low to significant amounts of soot. To achieve these conditions three strategies were adopted. First, at atmospheric pressure, the strain rate, was varied from low to high values, with the lower values resulting in larger residence times and, consequently, in higher soot formation. Second, for a particular strain rate and atmospheric pressure, the oxygen content in the oxidizer stream was increased, which leads to higher flame temperatures and, consequently, higher soot production. Third, for a specific strain rate, the pressure was increased, also resulting in higher soot production. Additionally, the effect of simplified transport properties model was analyzed.

It was found that the gas and soot radiation terms are of primary importance for flame simulations. The importance of the radiation heat loss on soot predictions shown here is consistent with the literature, even though some studies consider different configurations. The additional coupling terms (mass and thermodynamic properties) are generally a second order effect, but their importance increase as the soot amount increases.

As a general recommendation the full coupling should be taken into account only when the soot mass fraction, Y_S, is equal to or larger than 0.008. However, if a higher precision is required, with errors lower than 1%, the full coupling should be taken into account when $Y_S \geq 0.002$, which is the lower threshold of the most sensitive gas species, H_2. The non-coupled model could not represent the soot mass fraction predicted by the coupled model with errors lower than 1%. For lower soot amount, the coupling through soot mass and thermodynamic properties may be neglected as a first approximation, remembering that an error on the local mass conservation will be present.

The results also showed that discrepancies from choosing different transport models (detailed or simplified) are larger than those found from not fully coupling the phases.

4 EFFECT OF ADIABATIC AND UNITY LEWIS NUMBER APPROXIMATIONS IN SOOT PREDICTIONS FOR ETHYLENE COFLOW LAMINAR FLAMES

In this chapter the soot modeling on a sooting non-smoking atmospheric ethylene coflow laminar flame is assessed using a semi-empirical model. A semi-empirical model is chosen since it combines important steps for soot formation, good predictability of global soot variables and low computational time, specially for practical combustion systems. In the first part of the chapter the soot model is explained as well as the numerical method to solve the target flame. In the second part the numerical result is assessed against experimental data from the literature. In the last part some modeling approximations are explored and discussed.

4.1 Numerical model

For the coflow flame simulations, the conservation equations for total mass (Equation 2.17), momentum (Equation 2.18), mass of species (Equation 2.19) and energy (Equation 2.20) are used in cylindrical coordinates along with the respective constitutive relations. Also the radiation model is describe in the Section 3.1.2 and will not be repeated here. For soot prediction, it is employed the same model already presented in Chapter 3. The main differences are detailed below.

4.1.1 Soot model

The soot model used in this section is based on Liu et al., 2002. This model is similar to the already presented in Chapter 3 and only differs in the surface growth rate $k_2 = 1.75 \times 10^3 \exp\left(\frac{-10{,}064}{T}\right)$ and in the thermophoretic velocity constant $C_i = 0.65$ in order to improve the accuracy of the model for a multi-dimensional configuration. The two-dimensional conservation equations for soot mass fraction and soot number density in cylindrical coordinates reads

$$\begin{aligned}\frac{\partial\left(\rho Y_S\right)}{\partial t}+\rho u\frac{\partial\left(Y_S\right)}{\partial z}+\rho v\frac{\partial\left(Y_S\right)}{\partial r}=&-\frac{\partial\left(\rho V_{T,z}Y_S\right)}{\partial z}-\frac{1}{r}\frac{\partial\left(r\rho V_{T,r}Y_S\right)}{\partial r}\\&+\frac{\partial}{\partial z}\left(\rho D_p\frac{\partial Y_S}{\partial z}\right)+\frac{1}{r}\frac{\partial}{\partial r}\left(r\rho D_p\frac{\partial Y_S}{\partial r}\right)\\&+\dot{w}_{Y_S},\end{aligned}\tag{4.1}$$

$$\begin{aligned}\frac{\partial\left(\rho N_S\right)}{\partial t}+\rho u\frac{\partial\left(N_S\right)}{\partial z}+\rho v\frac{\partial\left(N_S\right)}{\partial r}=&-\frac{\partial\left(\rho V_{T,z}N_S\right)}{\partial z}-\frac{1}{r}\frac{\partial\left(r\rho V_{T,r}N_S\right)}{\partial r}\\&+\frac{\partial}{\partial z}\left(\rho D_p\frac{\partial N_S}{\partial z}\right)+\frac{1}{r}\frac{\partial}{\partial r}\left(r\rho D_p\frac{\partial N_S}{\partial r}\right)\\&+\dot{w}_{N_S},\end{aligned}\tag{4.2}$$

The thermophoretic velocity now reads

$$V_{T,x_i}=-C_i\frac{\mu}{\rho}\frac{1}{T}\frac{\partial T}{\partial x_i},\quad (x_i=z,r)\tag{4.3}$$

4.1.2 Coupling of soot and gas-phase species

The results of the soot model are taken into account by creating a new gas species C_{soot} and imposing $Y_{C_{soot}}=Y_S$. Thus, in the mixture properties calculations, soot is accounted for as an additional gas-phase. Also additional source terms for species related to soot formation and oxidation (C_2H_2, H_2, CO, H, O_2, OH and O) are added to the system of equations. Thus, the elements are conserved, the summation of species mass fractions is equal to one ($\sum_{i=1}^{N}Y_i=1$) and the summation of species source terms (in mass basis) is equal to zero ($\sum_{i=1}^{N}\dot{w}_i=0$). Therefore the interaction between the soot chemistry and the gas-phase chemistry was accounted for in the transport equations for the total mass, for the mass of species and for energy. The transport and thermodynamic properties from the C_{soot} species are modelled as the ones from a solid carbon (graphite).

4.2 Description of the problem

The target flame in this work is the atmospheric pressure, non-smoking ethylene/air coflow diffusion flame of Santoro et al., 1983. There is a significant experimental data available for this flame and it has been widely studied by many researchers in experimental works (e.g. Santoro et al., 1983, Santoro et al., 1987, Kennedy et al., 1996, Arana et al., 2004, and Iyer et al., 2007) and numerical modelling works (e.g. Liu et al., 2003, Zhang et al., 2009, Dworkin et al., 2011, Eaves et al., 2013, Eaves et al., 2015, Khosousi and Dworkin, 2015). This flame is also recommended as one of the soot study cases by *International Sooting Flame (ISF) Workshop* (see at ISF, 2016).

According to the description of Santoro et al., 1983, the burner consists of two concentric tubes of internal dimeters of 11.1 mm and 101.6 mm, with the fuel flowing through the central tube and air through the outer passage. Also, the fuel tube extends 4 mm beyond the exit plane of the air tube. The mean velocity of the fuel stream is 3.98 $cm\ s^{-1}$ (flow rate 3.85 $cm^3\ s^{-1}$) and of the air stream is 8.9 $cm\ s^{-1}$ (flow rate 713.3 $cm^3\ s^{-1}$).

4.3 Numerical method

Figure 4.1 shows the laminar diffusion coflow and the axisymmetrical cylindrical coordinate system. The computational domain is covered in z direction from 0 to 15 cm (with $z = 0$ at the exit plane of the fuel tube) and in the r direction from 0 to 4.75 cm. Non-uniform mesh is used to save computational time while solving large spatial gradients. The mesh is refined in the flame region with maximum resolution of $dr = 0.1\ mm$ and $dz = 0.2\ mm$ between $r = 0.0\ cm$ to 0.555 cm and $z = 0.0\ cm$ to 10.0 cm. From $r = 0.0\ cm$ - 1.0 cm the refinement in the r direction was set to increase with a growth ratio of 1.1. It was found that further refinement did not change the variables analyzed in the present work. Therefore the total number of volumes for the current domain was 47,241 volumes. The fuel stream is pure ethylene and the oxidizer stream has the simplified composition of standard dry air ($Y_{O_2} = 0.233$ and $Y_{N_2} = 0.767$). Fully develop flow velocity profile was assumed to the fuel stream and a boundary layer type velocity profile for the air stream at the inlet boundary. The inlet temperature for both streams are set to 300 K. The inlet gas preheating was not considered in this work. The wall was treated as a free-slip wall condition and the exit of the domain as treated as an outflow boundary condition.

The system of equations described by Equations 2.17 - 2.20 for axisymmetrical coordinate system, was solved with the commercial CFD software ANSYS FLUENT v.16.1 for steady state conditions. Instead of the energy equation (Equation 2.20), described here in terms of enthalpy, h, FLUENT software uses the energy equation in terms of total Energy ($e = h - p/\rho + v^2/2$), for further details see Fluent, 2015. It was used a

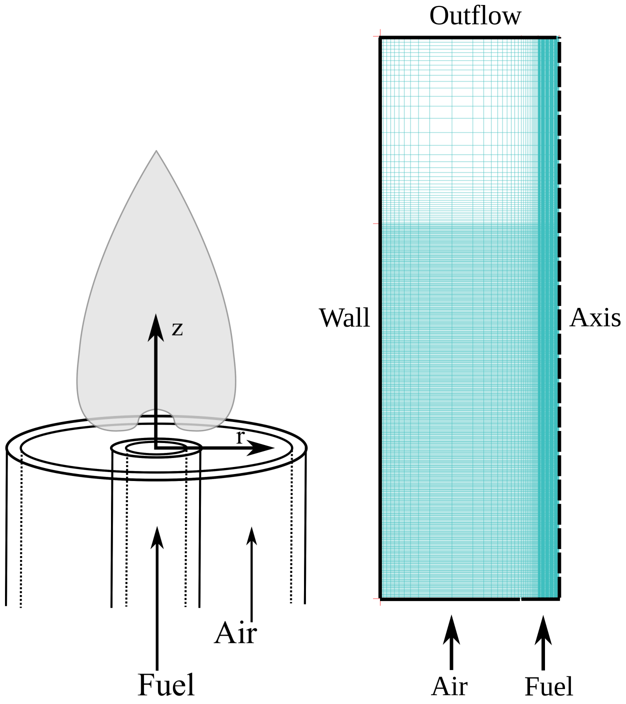

Figure 4.1: Laminar diffusion coflow representation; a) Axisymmetrical coordinate system; b) Axisymmetrical numerical domain with an example of mesh distribution.

segregated Pressure-based solver with the SIMPLE algorithm to treat the pressure and velocity coupling. The advective terms were discretised by second order upwind while the diffusion terms were discretised by second order central differencing.

The soot equations (Equation 4.1 and 4.2) are introduced through a User Defined Function (UDF) in FLUENT and are solved for each iteration along with the remaining conservation equations. The results of the soot model are taken into account by creating a new gas species C_{soot} and imposing $Y_{C_{soot}} = Y_S$. Thus, in the mixture properties calculations, soot is accounted for as an additional gas-phase. The soot advective term was discretised by second order upwind and the diffusion terms, including the additional thermophoretic term, were also discretised by second order central differencing. The additional thermophoretic diffusion term was lumped into the source term.

The numerical results are sensitive to the choice of kinetic mechanism. A study with different mechanisms can be found in the Appendix B. Nonetheless, the current work follows the choice of the reference work [Liu et al., 2002], employing a modified version of the kinetic mechanism GRI3.0 [Smith et al., 2000], without all NOx species and reactions. In addition, an species is added to the kinetic mechanism in order to account the soot species. With this mechanism a total of 37 species and 219 reactions was considered. Thermodynamic and transport properties were taken from kinetic mechanism GRI3.0. In this simulation the diffusion coefficients are calculated through the mixture-average approach, Equation 2.16. Viscosity and thermal conductivity are calculated through the Equation 2.10 and 2.11, respectively.

According to Liu et al., 2003, the use of OTA radiation model on the target flame (non-smoking flame) resulted in a slightly under-prediction of the peak centreline flame temperature, when compared to discrete-ordinates method (DOM) with a statistical narrow-band correlated-k (SNBCK) model for the absorption coefficients. Nonetheless extreme attention must be paid when using OTA for smoking flames, since of radiation absorption and strong coupling between temperature and soot oxidation in the upper portion of the flame are important. Thus the present sutdy uses the OTA radiation model, described the Section 3.1.2, with the soot constant of $C = 3.337 \times 10^{-4}$ ($W\ m^{-3} K^{-5}$), similar as Liu et al., 2002.

4.4 Results

In this section an assessment to the soot model was done in order to verify soot predictions of the present work against experimental data. The numerical results of this set of models are compared to experimental axial velocities, temperature, C_2H_2 mole fraction and soot volume fractions. Later the structure of simulated ethylene coflow flame is presented and discussed, as well as the effect of heat loss due to radiation and the choice of transport properties evaluation.

4.4.1 Comparison with experimental data

Figure 4.2 show the comparison between experimental data from Santoro et al., 1987, and the present simulation for the axial velocity as function of the radius for four heights above the burner exit face. It is possible to see that the present simulation have a good agreement with the axial velocity measurements. A small deviation can be seen at the lower height ($z = 10\ mm$) near the tube exit ($r = 0$). This deviation can be attributed to the tube and fuel preheating effect (not considered in this simulation), which can modify the inlet velocities profiles. It is possible to see that the axial velocity increases with the high above the burner. This is due to the gas expansion and buoyancy effects as will be show later.

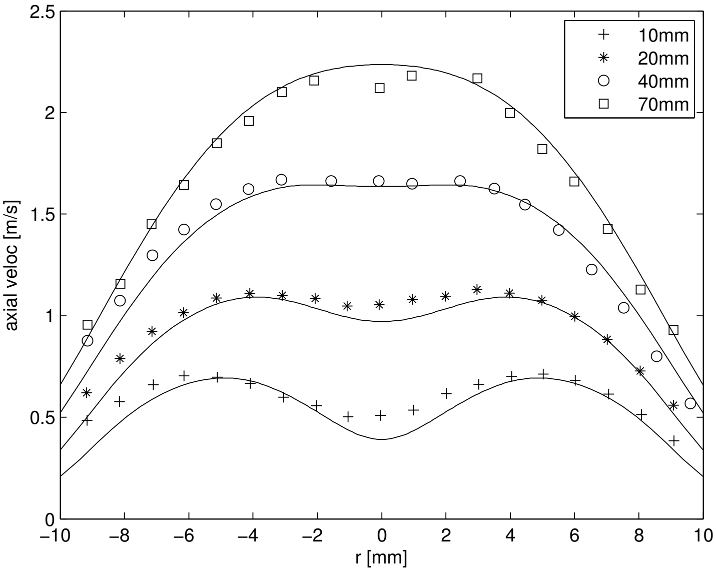

Figure 4.2: Axial velocity comparison for four heights; Symbols: experimental data Santoro et al., 1987; solid line: present simulation

The predicted radial temperatures at four heights above the burner exit face, $h =$ 10, 20, 50 and 70 mm are shown in Figure 4.3. The comparison with the experimental data shows good agreement at the outer part of the flame, but could not predict the measured temperatures near the tube centerline. This discrepancy can be attributed to either the choice of kinetic mechanism or the preheating effect of the fuel tube and fuel stream, which were not accounted for in this work. Guo et al., 2002, Charest, 2011, and Eaves et al., 2013, simulated ethylene coflow flames, in similar configuration to this target flame, and analysed the influence of wall boundary condition of fuel tube on the flame. Guo et al., 2002, assumed a fuel tube temperature profile, Charest, 2011, assumed isothermal and adiabatic wall treatments, while Eaves et al., 2013, used Conjugate Heat Transfer (CHT), isothermal and adiabatic wall treatments. The main result of all these works is that the flame preheating effect has a significant influence on the prediction of flame temperature and species, including soot, specially in the centreline. According to Eaves et al., 2013, when CHT is used, the soot formation predictions on the centerline is improved, since the model is able to capture the fuel pyrolysis that occurs inside the fuel tube. Results from Guo et al., 2002, showed that the velocity profiles of both streams at the nozzle exit are neither fully developed nor uniform profiles. Therefore, from the result

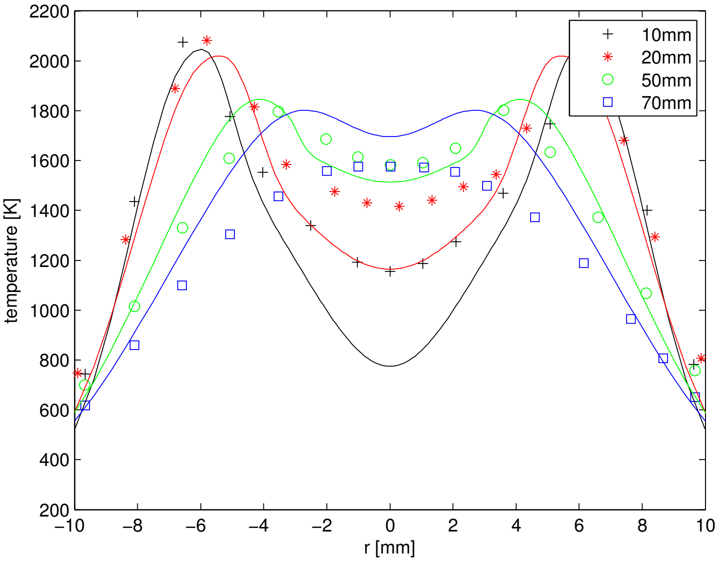

Figure 4.3: Temperature comparison; Symbols: experimental data Santoro et al., 1987; solid line: present simulation

presented above it is expected some discrepancies in temperature, gas-phase species and therefore in the amount of soot predicted by the current simulation.

The Figure 4.4 shows the comparison for C_2H_2 mole fraction radial profile at two heights. The correct prediction of acetylene field is important in the current modelling since the nucleation (R1) and surface growth (R2) are directly dependent on it. The model can capture the position of C_2H_2 mole fraction, but not the amplitude. For example, close to the fuel tube ($r = 5.55\ mm$ and $h = 7\ mm$) the model over-predict the acetylene concentration in 1.85 times, $X_{C_2H_2,sim} = 0.054$ instead of $X_{C_2H_2,exp} = 0.029$. Since this particular region is extremely important to soot formation (in this region the first particles are nucleated and start to grow) the prediction of soot formation will be directly affected and deviations are already expected.

The soot amount predicted by the set of model is then compared to experimental data in two ways. First, the soot volume fraction radial profiles at two heights above the burner are compared and shown in the Figure 4.5, and second, the total amount of soot produced along the height of the flame is compared and shown in the Figure 4.6. Figure 4.5 shows that the model can predict the behaviour of soot formation in the radial direction, with values in the same order as the experimental data. Nevertheless, the exact values of f_v are not found for the heights presented in the figure. While the model overpredicts the soot production at $h = 15\ mm$ it also underpredicts the soot production

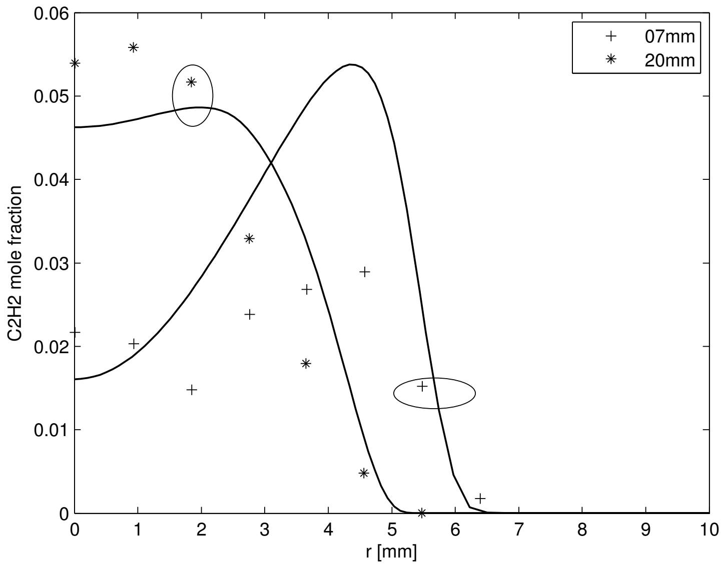

Figure 4.4: C_2H_2 mole fraction comparison; Symbols: experimental data Kennedy et al., 1996; solid line: present simulation

at $h = 50\ mm$.

This second comparison is done in terms of integrated soot volume fraction

$$f_{v,int}(h) = 2\pi \sum_{r=0}^{R} r f_v(r,h) dr, \tag{4.4}$$

where h is the height above the fuel tube exit. The comparison of f_v integrated along the height of the flame (Figure 4.6) shows that the amount of soot predicted by the model follows the same pattern of formation and oxidation as both expermintal works of Santoro et al., 1987, and Arana et al., 2004. The simulated soot formation reached the same maximum integrated value, but in a lower position (29 mm instead of 40 mm). The soot is being formed earlier and consequently it is being oxidized earlier. Based on the decay of the f_v integrated it is possible to estimate the flame length of the current simulation is around 70 mm, again a lower value than the experimental of Santoro et al., 1987, which reported a flame length of 88 mm.

4.4.2 Flame structure

Figure 4.7 brings two-dimensional details of the flame structure, including temperature and soot fields and flow stream lines. It is interesting to see the effect of the heat loss by gas and soot radiation in the temperature field (left part), specially downstream,

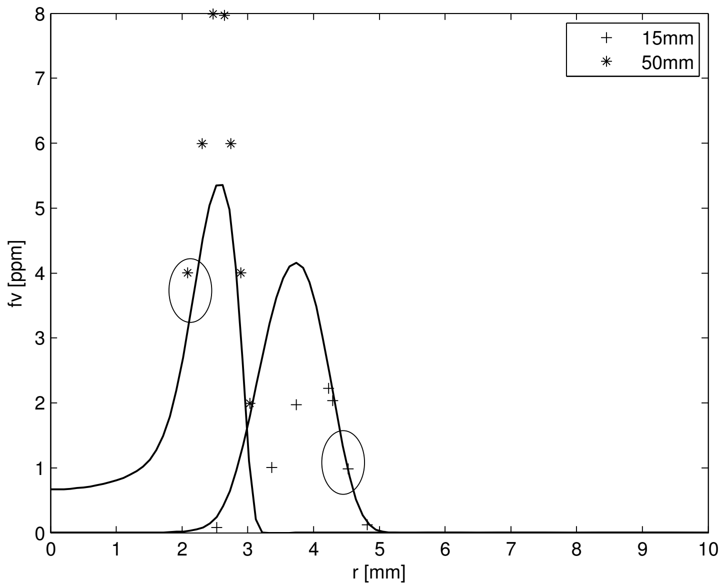

Figure 4.5: Radial f_v comparison; Symbols: experimental data Santoro et al., 1987; solid line: present simulation

making the high temperature region limited in a small "wing" area near the fuel tube region. The maximum temperature predicted was 2050 K. In the right part of the figure it is presented the f_v field. The soot field is kept in a very narrow area when compared to the flame area shown in the left part. It is interesting to see that the region where the maximum soot volume fractions are found starts at coflow side. The same result was presented by Santoro et al., 1987. The f_v field follows the flow flied and is slightly influenced towards the center of the flame by the thermophoretic diffusion. The maximum soot volume fraction predicted by the present simulation is $f_{v,max} = 7.1$ ppm while the experiment of Santoro et al., 1983 reported $f_{v,max} = 9$ ppm. The stream lines show that the flow accelerates as it moves upwards entraining the coflow air. This behaviour is due to the expansion of the gas mixture as the temperature increases and it is also influenced by buoyancy effects. As a result, there is a large residence time for soot formation, since soot particles are transported towards the center of the flame.

The Figure 4.8 shows the predicted soot in f_v [-] and how the soot reactions are spatially distributed along the flame. It is possible to notice some aspects of the soot formation process. First, the reactions of soot formation are spatially wider than the reactions of oxidation. Second, the surface growth reaction dominates the soot formation and the oxidation by OH dominates the soot consumption. Third, the nucleation of the

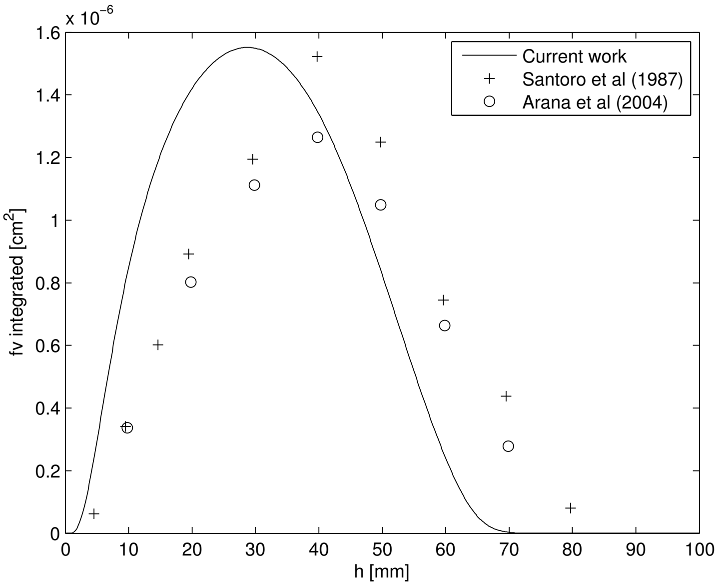

Figure 4.6: f_v integrated comparison; Symbols: experimental data Santoro et al., 1987 and Arana et al., 2004; solid line: present simulation

first particles start to occur in the coflow side ($r > 0.5\ mm$), but in the inner part of the flame close to the temperature peak and where the C_2H_2 is present.

The flame is also affected by the heat loss due to the radiation of gas and soot, which is shown in the Figure 4.9. The Figure shows the comparison of the temperature profile with the main components of heat loss by radiation. It is possible to see that the contribution of the soot on heat loss is one order of magnitude higher than the gas contribution. From all gas-phase species which participate in the gas radiation (H_2O, CO_2, CO and CH_4) CO_2 contribution is dominant. While the soot radiation source term is located in the inner part of the flame, the total gas-phase radiation source term is more important in the upper part of the flame. The combination of both solid and gas-phase radiation alter significantly the temperature profile, making the peak temperature to appear at the "wings" of the flame, instead of the centerline when no heat loss is accounted for (see Figure 4.10).

4.4.3 Radiation and Transport properties effect:

A common approach to reduce the time required to evaluate multicomponent transport properties in flames is to calculate the diffusion coefficients for the gas species assuming unitary Lewis Number ($Le_i = {}^{\lambda}/_{\rho c_p D_i^M} = 1$). Additionally, simplified formula-

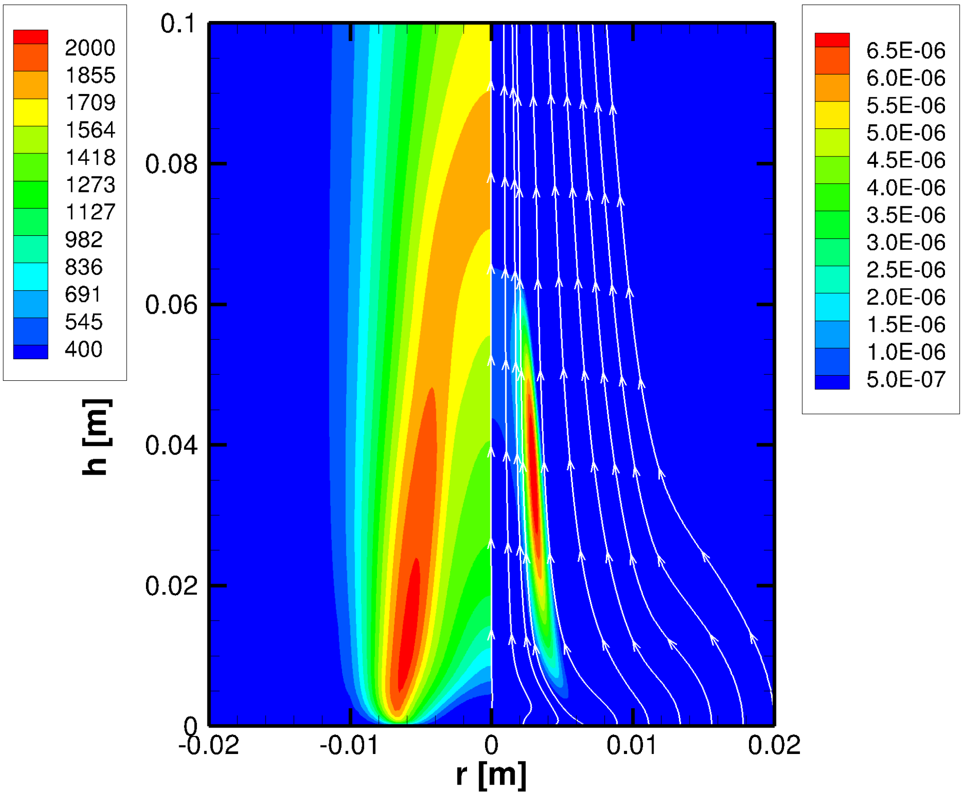

Figure 4.7: Left: Temperature [K] contour; Right: f_v [-] contour with velocity streamlines

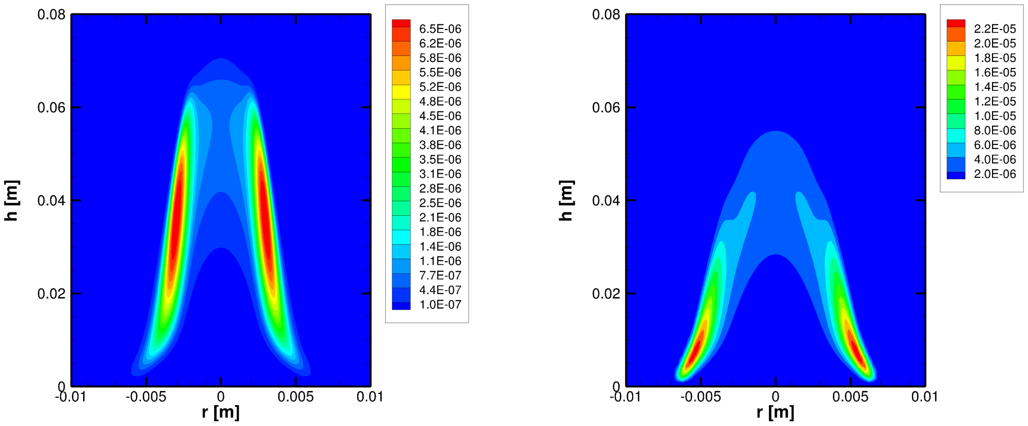

(a) Soot f_v

(b) Nucleation rate

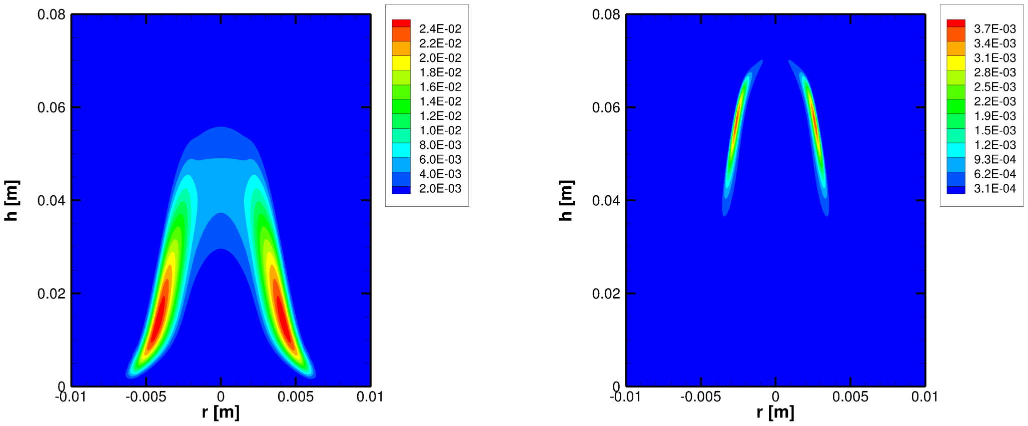

(c) Surface growth rate

(d) Oxidation by O_2 rate

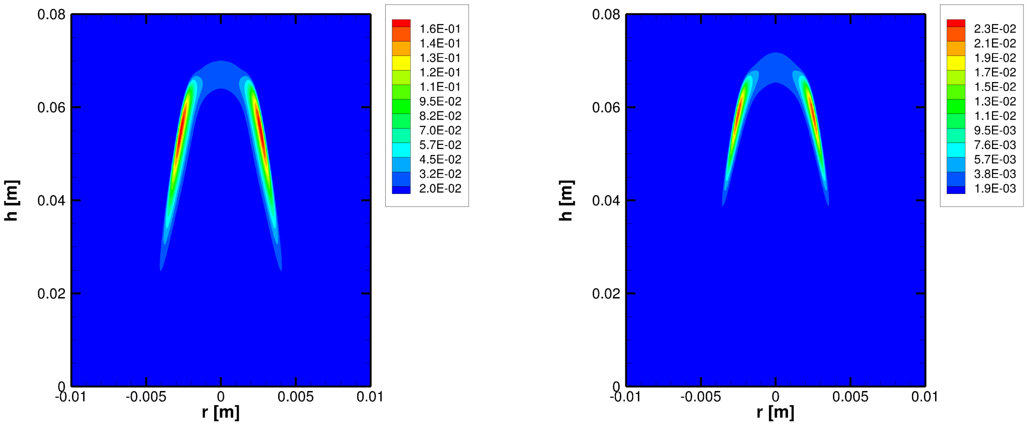

(e) Oxidation by OH rate

(f) Oxidation by O rate

Figure 4.8: Soot f_v [-] and rates $[kmol/m^3s]$

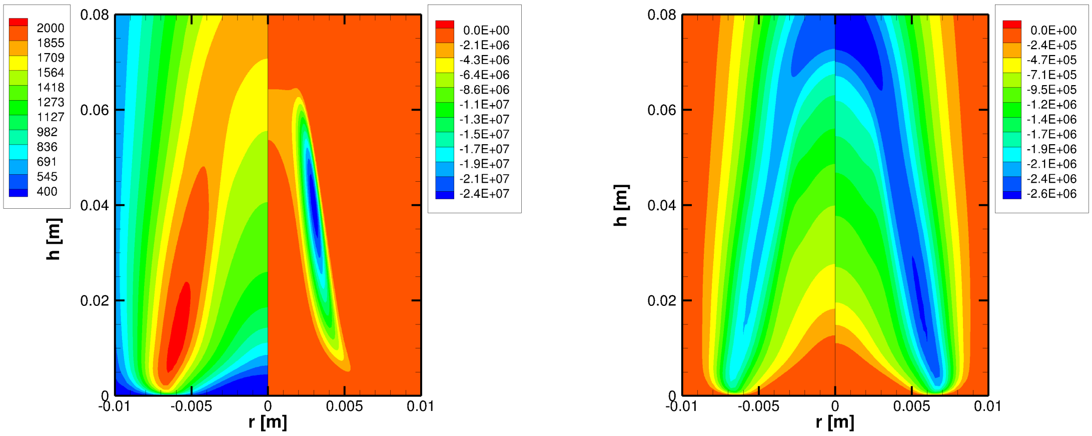

(a) (b)

Figure 4.9: Comparison of temperature and radiation components; a) Left: Temperature [K] contour; Right: soot radiation source term [W/m^3]; b) Left: CO_2 radiation component in the source term [W/m^3]; Right: total gas source term [W/m^3]

tions are frequently used for other properties. In this section, those proposed in Smooke and Giovangigli, 1991 are employed: $\lambda/c_p = 2.58 \times 10^{-5}\,(T/298)^{0.69}$ (W m^{-1} K^{-1}) and $\mu/c_p = 1.67 \times 10^{-8}\,(T/298)^{0.51}$ (kg m^{-1} s^{-1}). The effect of such simplifications are evaluated and compared to the most detailed solution. Also the effect of heat loss by radiation is evaluated.

The comparison of temperature fields is shown in Figure 4.10 and the comparison of f_v fields is shown in Figure 4.11. The temperature contours for the same heat loss condition are very similar. For the adiabatic conditions the maximum temperature is found in the centerline while for the non-adiabatic conditions is found in the flame "wings". The maximum temperature found are 2243, 2050, 2301 and 2065 K, for the 4 cases presented in Fig. 4.10, respectively. Also the relative difference between the simplified and the detailed transport approach within the same heat loss condition ($(\phi_{simplified,max} - \phi_{detailed,max})/\phi_{detailed,max}$) are low 2.59% and 0.73%, for adiabatic condition and non-adiabatic condition, respectively. Thus, it can be anticipated that the approximate 200K temperature difference between adiabatic and non-adiabatica cases probably have an important impact on species fields and, consequently, on soot production and destruction. On the other hand, it is not clear the possible effects due to the

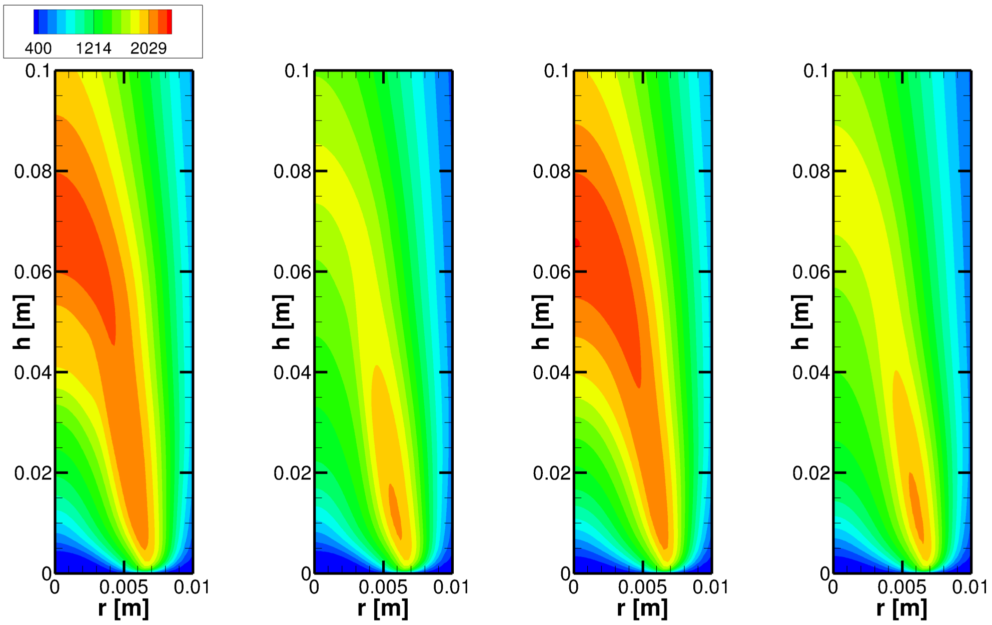

Adibatic Non-adibatic
Detailed transport

Adibatic Non-adibatic
Simplified transport

Figure 4.10: Radiation and transport properties comparison on the temperartue field [K].

smaller differences due to transport models.

In Fig. 4.11 we see the same results for f_v. The similarity of the f_v contours for the same heat loss condition are also found, but now the maximum values are more influenced by the transport properties choice. The $f_{v,max}$ found are 8.65, 7.09, 6.68 and 5.63 *ppm*, for the four cases shown, respectively. The relative difference between the simplified and the detailed transport approach within the same heat loss condition are -22.77% and -20.59%, for adiabatic condition and non-adiabatic condition, respectively.

Nevertheless, the analysis of soot formation is only complete when compared all four cases in terms of integrated soot volume fraction $f_{v,int}$, which is shown in the Figure 4.12.

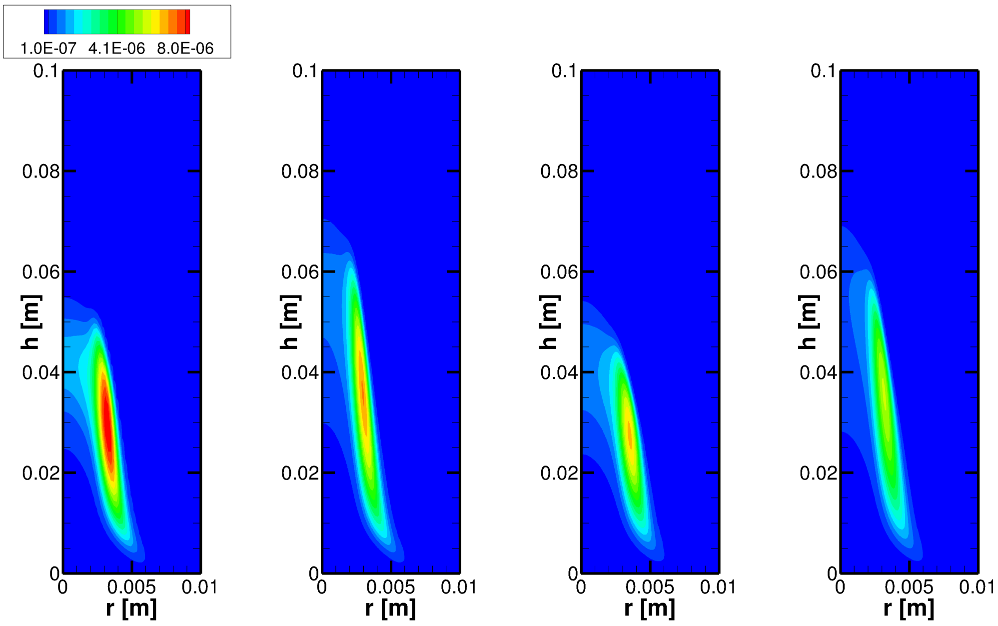

Adibatic Non-adibatic Adibatic Non-adibatic
Detailed transport Simplified transport

Figure 4.11: Radiation and transport properties comparison on the f_v field [-].

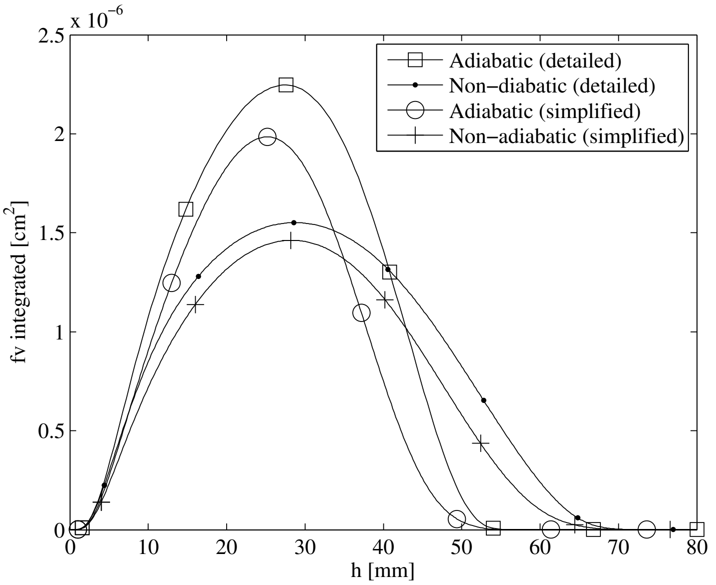

Figure 4.12: Heat loss and transport properties comparison on the $f_{v,int}$

It is possible to see some additional aspects. First, the soot formation and destruction rates for the same the loss condition are similar. Second, the simplified transport approach was less able to reproduce the total amount of soot in the adiabatic case than in the non-adiabatic case. Thus, the heat loss condition reduced the deviation associated to the simplification on the evaluation of multicomponent transport properties.

4.5 Conclusions:

In this chapter soot formation on atmospheric ethylene coflow flame was numerically analysed. A semi-empirical two equation model was chosen for predicting soot mass fraction and number density. The model describes particle nucleation, surface growth and oxidation. For the gas-phase a detailed kinetic mechanism was considered. The model was implemented in a commercial CFD and assessed against experimental data from the literature. Additionally the effect of choosing different transport models (detailed or simplified), considering gas and soot radiation heat losses, were evaluated in the optically thin limit approximation.

The target flame in this work was the atmospheric pressure, non-smoking ethylene-air coflow diffusion flame of Santoro et al., 1983. The comparison with experimental data showed that the model could predicted the behaviour of soot formation, with values in the same order as the experimental data, but the exact values of f_v were not found. It was also found that some aspects in numerical modeling can have important impact on soot predictions and should be more investigated. Here follows the main aspects found in this study that can bring uncertainties to soot modeling:

- The preheating of the fuel tube and, consequently, the fuel stream can change the temperature and velocity fields at the fuel tube exit were not accounted for in the present model.
- The choice of the kinetic mechanism can have an influence in the soot predictions. See the Appendix B, for further discussion.
- There are some intrinsic limitations of the chosen soot model (semi-empirical) and the parameters of the soot reactions. An example of the influence of the soot parameters can be found in the Appendix C.

Additionally, it was found that the gas and soot radiation terms are of primary importance for flame simulations and that a first attempt to solve the target flame can be done using a simplified transport model. If a more accurate solution is needed the solution can be resumed with detailed transport properties.

5 MODELING SOOT FORMATION WITH FLAMELET-GENERATED-MANIFOLD

In this chapter the reduction kinetic technique FGM is used for simulating a sooting non-smoking ethylene flame. A great challenged is imposed when a large amount of soot is formed, since it might change the thermodynamic and kinetic state as it interact with the gas-phase species. Previously, it had been shown that the adiabatic condition has a higher production of soot than a non-adiabatic condition and that simplified approaches for transport processes also change soot predictions. Although less precise, the adiabatic condition with unity Lewis number will be used in the present chapter to validate the soot implementation in the FGM technique. This strategy allows the inclusion of soot in the manifold without the need to take heat losses or preferential diffusion effects into account. For the model validation, the FGM results are assessed against detailed chemistry solutions with the same simplifications.

Thus the FGM method is applied to the adiabatic ethylene diffusion flame in two main different conditions. In the first the FGM method is applied to solution without the soot model and assessed against a detailed solution in order to validate its implementation. In the second part soot formation is included in the FGM method and is assessed against a detailed solution which also includes the soot formation.

5.1 Numerical method:

In this chapter numerous methods are applied to solve an adiabatic ethylene coflow flame either using detailed chemistry or the FGM reduction technique.

One-dimensional ethylene counterflow flames

The system of equations is solved with the code CHEM1D, 2016, for steady state conditions. The chemical kinetic mechanism GRI 3.0 without all NOx species and reaction is used. The diffusion coefficients are calculated using Unity Lewis number approach. Additionally, simplified formulations are used for thermal conductivity, proposed in Smooke and Giovangigli, 1991, $\lambda/c_p = 2.58 \times 10^{-5} \left(T/298\right)^{0.69}$ (W m^{-1} K^{-1}) and for viscosity $\mu/c_p = 1.67 \times 10^{-8} \left(T/298\right)^{0.51}$ (kg m^{-1} s^{-1}).

Detailed solution: When the full set of equation (Equations 2.40 - 2.45) are solved using detailed chemistry, it will be referred as detailed solution. The fuel stream is pure ethylene and the oxidizer stream has the simplified composition of standard dry air ($Y_{O_2} = 0.233$ and $Y_{N_2} = 0.767$). All cases converged using a convergence criteria of 1×10^{-10}. An adaptive mesh refinement was used according to the gradients of the following variables: temperature, density, heat release, $Y_{C_2H_4}$, $Y_{C_2H_2}$, Y_O and Y_H. The distance of both boundaries to the stagnation plane is different for each strain rate, a, but it was guaranteed to be sufficiently large for all gradients near the boundaries to become zero, except for velocity, that follows a potential flow. It was found that the results for all variables analysed in the current work became grid independent for 300 points.

FGM solution: When the FGM method is used, the following set of equations is solved: the continuity transport equation in flamelet format (Equation 2.40), the stretch field K transport equation (Equation 2.45) and two controling variables in flamelet format, which reads

$$\frac{\partial(\rho u Z)}{\partial x} = \frac{\partial}{\partial x}\left(\frac{\lambda}{c_p}\frac{\partial Z}{\partial x}\right) - \rho K Z, \tag{5.1}$$

$$\frac{\partial(\rho u \mathcal{Y})}{\partial x} = \frac{\partial}{\partial x}\left(\frac{\lambda}{c_p}\frac{\partial \mathcal{Y}}{\partial x}\right) - \rho K \mathcal{Y}. \tag{5.2}$$

As all flames here are in adiabatic condition only two controlling variables are need ($\mathcal{Y}$ and Z), forming a 2D manifold. This solution will be referred as FGM solution. FGM data is retrieved from the manifold using bilinear interpolation. The fuel side boundary condition is set as $Z = 1$ and $\mathcal{Y} = 0$ and the for the oxidizer side boundary condition as $Z = 0$ and $\mathcal{Y} = 0$. All cases converged using a convergence criteria of 1×10^{-10}. Adaptive mesh refinement was used according to the gradients of the following variables: temperature, density, heat release, $\mathcal{Y}$ and Z. Again, zero gradients are guaranteed near the boundaries, except for velocity, and 300 points are sufficient to achieve grid independence.

Two-dimensional ethylene flame

The system of equations for axisymmetrical coordinate system, was solved with the commercial CFD software ANSYS FLUENT v.16.1 for steady state conditions. The chemical kinetic mechanism and transport properties are the same as the one-dimensional ethylene counterflow flames. The target flame in this chapter is similar to the one employed in the later chapter, which is an atmospheric pressure, non-smoking ethylene/air coflow diffusion flame of Santoro et al., 1983, nonetheless in adiabatic condition.

Detailed solution: When the set full set of equation, described by Equations 2.17 - 2.20, are solved using detailed chemistry, it will be referred to as detailed solution. The boundary conditions are the same as the ones presented in the later Chapter in the Section 4.3.

FGM solution: When the FGM method is used, the following set of equations is solved: the continuity transport (Equation 2.17), the momentum equation (Equation 2.18) and two controling variables Equations 2.46 and 2.47. For this adibatic flame only two controlling variables are need ($\mathcal{Y}$ and Z). This solution will be referred as FGM solution. The fuel side boundary condition is set as $Z = 1$ and $\mathcal{Y} = 0$ and the for the oxidizer side boundary condition as $Z = 0$ and $\mathcal{Y} = 0$. In respect to inlet velocities, the same approach as the detailed solution is taken here, where velocity profiles are prescribed. The wall was treated as a free-slip wall condition and set zero flux for all variables. The exit of the domain as treated as an outflow boundary condition.

Boundary conditions

Previous results with the same domain presented in Chapter 4 (Figure 4.1) showed an important discrepancy between the FGM approach and the detailed solution as can be seen in Figure 5.1 for the temperature field. An investigation of the problem revealed that the domain used in Chapter 4 makes the solution to adapt itself to the prescribed inlet boundary conditions. As will be shown in the following results, the temperature gradient extends below the air/fuel injection plane, a solution that cannot be captured with the model presented in Chapter 4. In order to capture such gradients, the domain was extended 10 mm below the injection plane. With this change comparisons between FGM and detailed results are in good agreement as will be shown next. The new computational domain is then covered in z direction from -0.10 to 15.00 cm (with $z = 0$ at the exit plane of the fuel tube) and in the r direction from 0 to 4.75 cm. The fuel tube (at $r = 0.555\ cm$) is set as an infinitesimal shell and its set to adiabatic condition without any kind of flux. All the others boundary conditions were kept the same as previous sections stated.

5.2 FGM results:

In this section the FGM method is applied to the adiabatic ethylene diffusion flame. This section is divided in two main parts. In the first the FGM method is applied

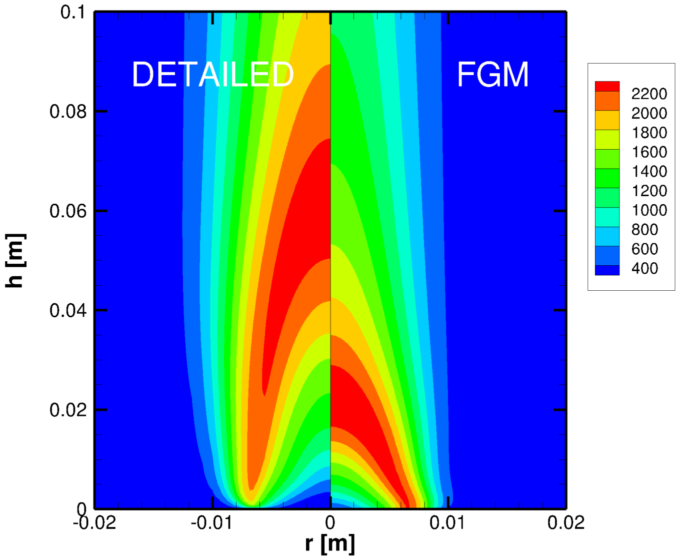

Figure 5.1: Initial comparison; Inlet area temperature $[K]$ contour; Left: detailed solution; Right: FGM solution

to solution without the soot model and assessed against a detailed solution in order to validate its implementation. In the second part soot formation is included in the FGM method and is assessed against a detailed solution which also includes the soot formation.

5.2.1 FGM validation without the soot model

In this subsection the the FGM method is applied to an ethylene diffusion flame in adiabatic condition without soot modeling. In order to verify the FGM method implementation the solution is then compared to a detailed chemistry solution.

The manifold was created by a variety of one-dimensional ethylene counterflow flames. To map all the possible conditions in the system state, the strain rate, $a = (-du/dx)_{x\rightarrow\infty}$, applied at the oxidizer side, was varied. The steady-state part of the manifold was generated from steady-state flamelets simulated from a low value of $a = 0.05\ s^{-1}$ up to the extinction limit at $a = 3154\ s^{-1}$. Additionally, the unsteady part of the manifold was generated from unsteady flamelets starting from $a = 3316\ s^{-1}$ until the mixing limit is reach. Following the principles stated in section 2.3.4.3 and through a

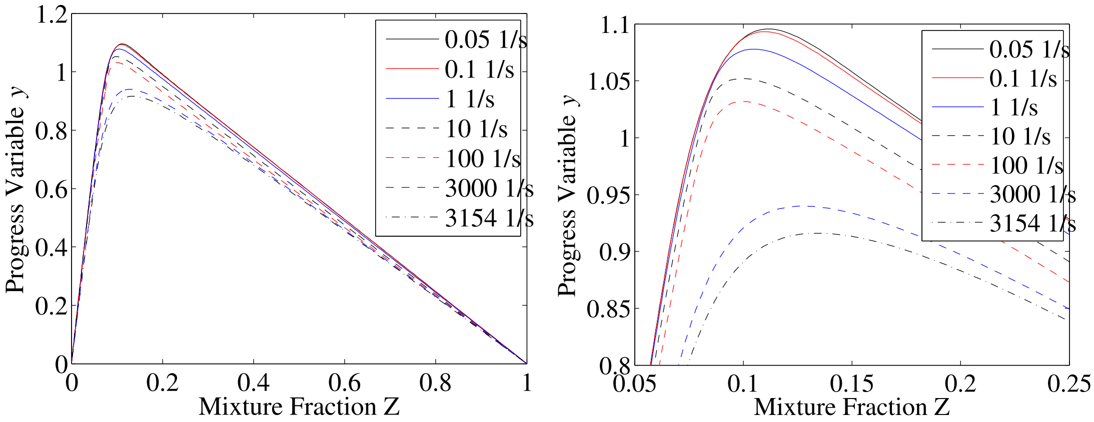

Figure 5.2: Steady flamelets in the Z and $\mathcal{Y}$ space; a) Whole domain; b) Zoom in the left corner of (a)

guess and check method an arbitrary progress variable composition was set as:

$$\mathcal{Y} = \alpha_{CO_2} Y_{CO_2} + \alpha_{H_2O} Y_{H_2O} + 0.9 \alpha_{CO} Y_{CO} \tag{5.3}$$

with $\alpha_i = 1/MW_i$. This definition leads to unique map of the dependent variables, which can be seen in Figure 5.2. It shows seven representative flamelets that cover the steady-state state part of the manifold in the domain (Z and $\mathcal{Y}$). It is possible to see that no flamelet overlap each other, making the choice of both controlling variables suitable for further use. The FGM database created in this section was discretized with a 300 X 300 (Z and $\mathcal{Y}$) equidistant grid. Figure 5.3 show the temperature, the progress variable source term, $Y_{C_2H_4}$ and $Y_{C_2H_2}$, as they are stored in the manifold, as function of Z and Progress variable $\mathcal{Y}$.

5.2.1.1 FGM Verification in one-dimensional flames:

The FGM method is applied to solve five ethylene counterflow flamelets, a =0.1, 1, 10, 100 and 1000 s^{-1}. The results are compared to the detailed solution of these flamelets. Figure 5.4 shows that the FGM solution can reproduce the solution of the detailed chemistry cases with very good agreement. Only a small deviation for the flamelet with the lowest strain rate ($a = 0.1$ s^{-1}) can be found. This small deviation on the Z and $\mathcal{Y}$ space says that if the FGM solution of a two-dimensional flame access that part of the manifold it might lead to some deviation from the detailed solution.

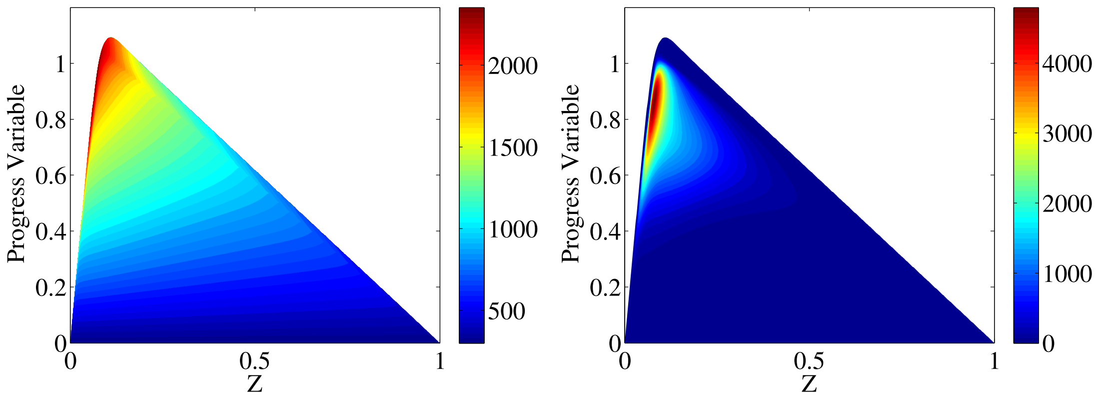

(a) Temperature contour $[K]$ (b) Progress variable source term $[kg\ m^{-3}]$

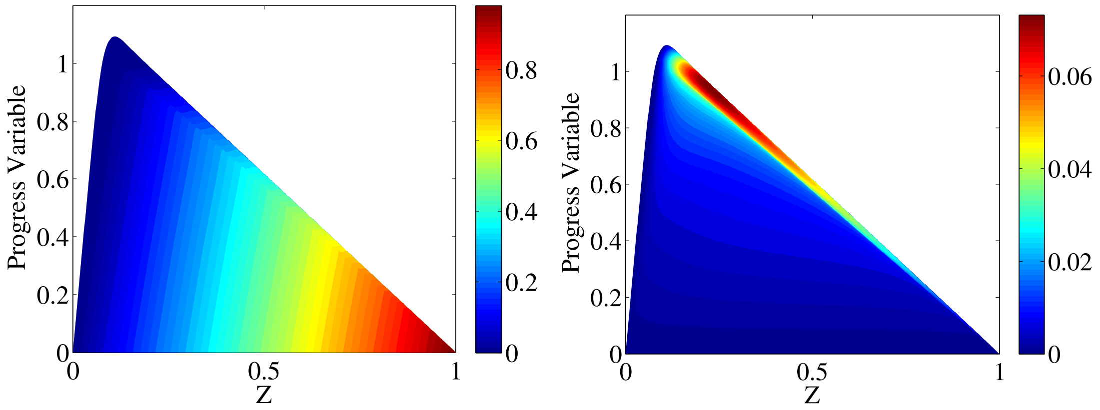

(c) $Y_{C_2H_4}$ contour (d) $Y_{C_2H_2}$ contour

Figure 5.3: Manifold visualization; Variables as function of (Z and $\mathcal{Y}$)

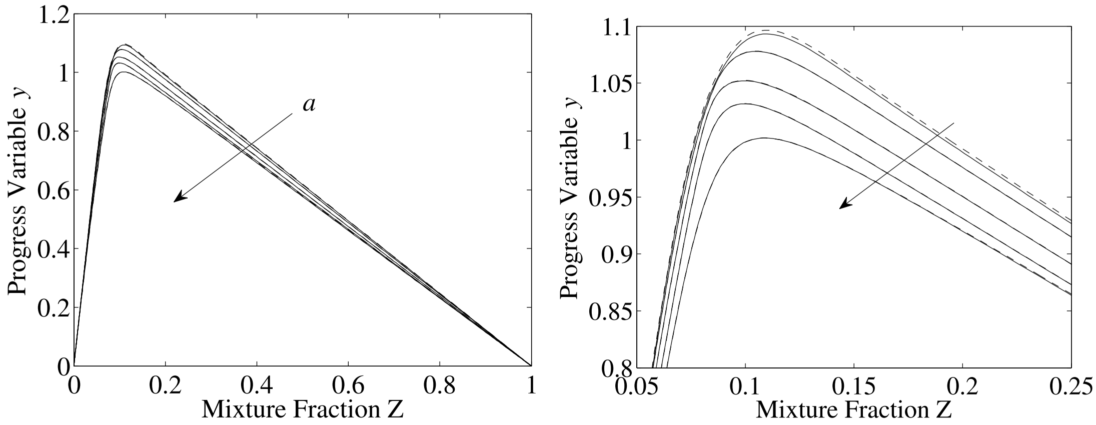

Figure 5.4: Comparison of FGM and detailed solution for flamelets at $a = 0.1$, 1, 10, 100 and 1000 s^{-1}; dash line: FGM solution; solid line: detailed solution; a) Whole domain; b) Zoom in the left upper corner

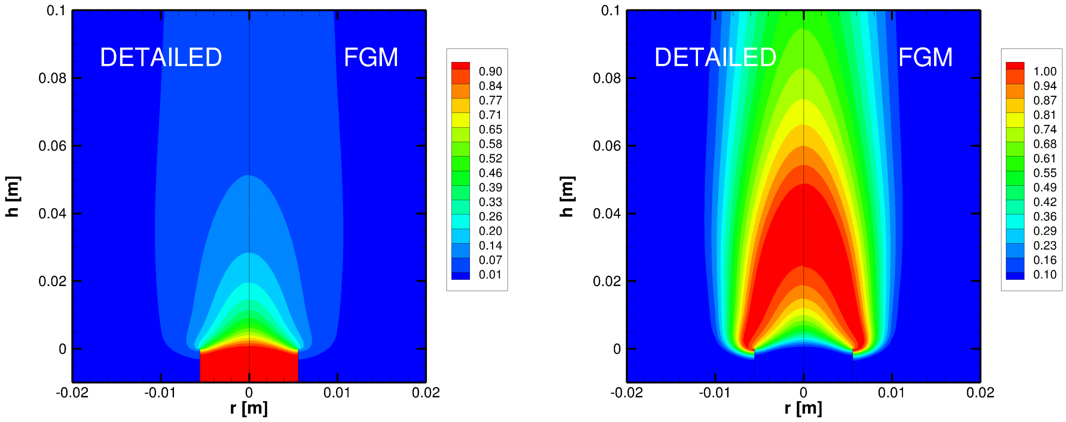

(a) Mixture fraction Z

(b) Progress variable $\mathcal{Y}$

Figure 5.5: Comparison between detailed solution and FGM solution for an adiabatic ethylene coflow flame, without soot modeling.

5.2.1.2 FGM Verification in two-dimensional flame:

The FGM method is then used to solve the two-dimensional ethylene flame. The comparison with the detailed solution is fisrt done for the mixture fraction Z and progress variable $\mathcal{Y}$ and is shown in the Figure 5.5. It is shown that the FGM method can represent the thermo-chemical space with the chosen two controlling variables with great accuracy. The second comparison is done with the retrived variables based on the fields of Z and $\mathcal{Y}$. Figure 5.6 shows the axial velocity, radial velocity, temperature, $Y_{C_2H_4}$, Y_{O_2} and $Y_{C_2H_2}$. It is possible to see that very good agreements were found between the solution of FGM method and the detailed case for most of the variables analysed. Even maximum values for temperature were very close $T_{FGM,max} = 2388\ K$ and $T_{detailed,max} = 2382\ K$. The only minor difference was found for $Y_{C_2H_2}$, in which the FGM simulation could not correctly capture the $Y_{C_2H_2}$ profile in the near the maximum value ($Y_{C_2H_2,FGM,max} = 0.068$ and $Y_{C_2H_2,detailed,max} = 0.078$). It is interesting to note that in the manifold the maximum value for the C_2H_2 mass fraction is equal to 0.075 and can be found in a very narrow area around the flamelet with $a = 0.1$, see Figure 5.3 (d). This means that there is a high gradient of acethylene in the manifold which is not being properly recover. Additionally the FGM solution could not retrieved the exact detailed solution in the one-dimensional flame (see Figure 5.4) near this maximum value for acethylene. So, for increasing accuracy

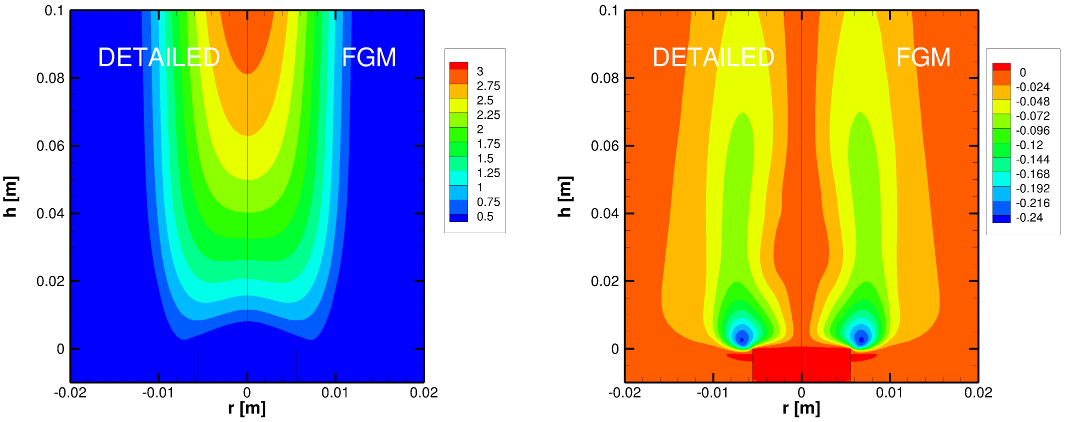

(a) Axial velocity $[m/s]$ (b) Radial velocity $[m/s]$

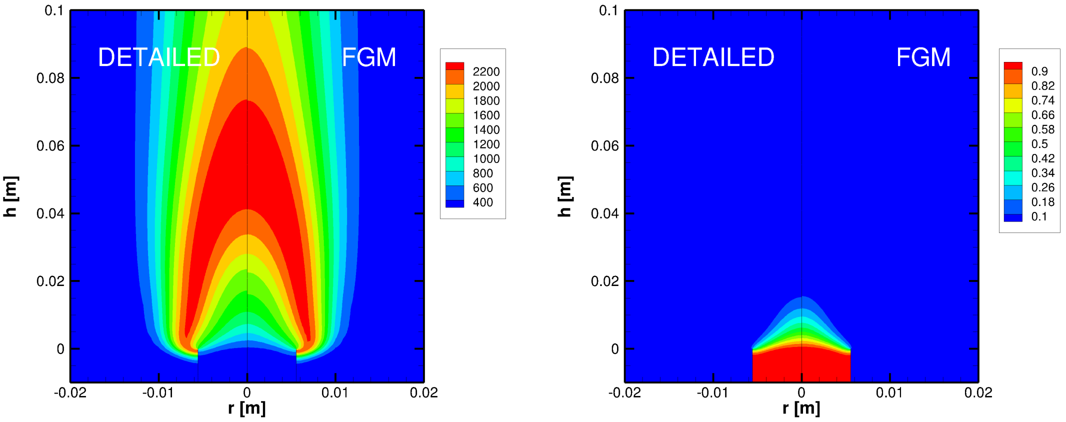

(c) Temperature $[K]$ (d) $Y_{C_2H_4}$

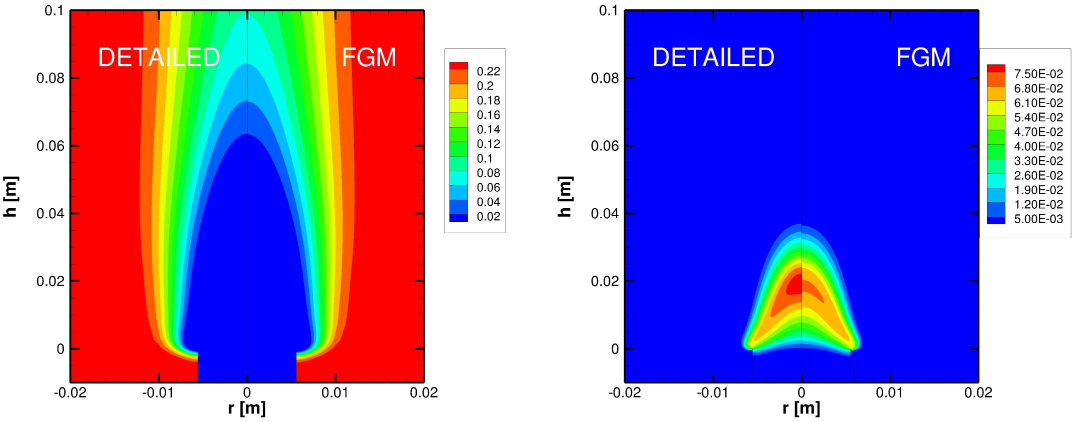

(e) Y_{O_2} (f) $Y_{C_2H_2}$

Figure 5.6: Comparison between detailed solution and FGM solution for an adiabatic ethylene coflow flame, without soot modeling.

of the FGM solution the following strategies may be applied:

- To choose a better definition of the progress variable so that the high gradients of $Y_{C_2H_2}$ could be captured. For this task methods of optimisation of the $\mathcal{Y}$, as the ones cited in the Subsection 2.3.4.3, can be used.
- To increase the degree of freedom of the system, increasing the number of progress variable $\mathcal{Y}$, as recommended by van Oijen, 2002, and van Oijen et al., 2016.

The results presented shows the potential of the FGM method for reproduting the multidimentional ethylene difussion flame. Since acetylene is the chosen soot precursor in the present model, it would be important to improve its modeling via FGM prior to evaluating the soot inclusion in the manifold. An optimization technique for $\mathcal{Y}$ is still under construction in the UFRGS research group and many ad-hoc tests could not improve the results. Thus, we decide to move forward with the present model keeping in mind that some discrepancies may arise due to this choice.

5.2.2 FGM validation with the soot model

In this section the inclusion of soot modeling in the FGM numerical solution is analysed. The soot formation is a slow process (like NO formation) and therefore it cannot be assumed in quasi-steady state. In this section three methods to include soot formation process in the FGM will be testes as follows

1. Store and retrieve the Y_S directly from the manifold,
2. Solve the two-equation soot model, storing and retrieving the source term for Y_S and N_S from the manifold,
3. Solve the two-equation soot model, storing and retrieving the soot rates for Y_S and N_S from the manifold.

The first approach is the simplest method, since only an additional variable is stored in the manifold and later retrieved after the solution is converged. As a consequence this method is expected to give greater errors than the others. The second approach is more elaborated than the first, since it is necessary to store two additional variables in the manifold and to solve two additional equations. It is expected to give reasonable results.

The last approach is an evolution of the second, where five additional variables are stored in the manifold and two additional equations are solved. This method is expected to give the best results. Each approach will be presented and discussed along the text.

Soot coupling terms

For flames that produce a high amount of soot, the inclusion of the soot in the system can change the pool of species and the termodynamic properties of the system. To account for these mass and energy coupling effects in either counterflow and coflow flames, the same approach presented in the subsection 4.1.2 is followed. This means that an additional species is added to the kinetic mechanism and its value is taken from soot mass fraction so that this additional species follows the equation and properties workflow of calculations. Also, this new species (that represents soot mass fraction) contributes to the definition and the transport of the mixture fraction Z.

Manifold

A new manifold is created for the case where soot is included in the flamelets. Similar to the manifold of gas solution only, the steady-state state part of the manifold was generated from steady-state flamelets simulated from a low value of $a = 1\ s^{-1}$ until the extinction limit at $a = 3154\ s^{-1}$. Additionally, the unsteady part of the manifold was generated from unsteady flamelets starting from $a = 3316\ s^{-1}$ until the mixing limit. Again through a guess and check method, a new progress variable was found as:

$$\mathcal{Y} = 0.5\alpha_{CO_2}Y_{CO_2} + \alpha_{H_2O}Y_{H_2O} + 0.8\alpha_{CO}Y_{CO} + \alpha_{H_2}Y_{H_2} - 0.5\alpha_{O_2}Y_{O_2} \tag{5.4}$$

This definition leads to unique map of the dependent variables, which can be seen in Figure 5.7. It is shown that there are no flamelets crossing each other and more important, it also shows that the inclusion of soot drastically altered the flamelets representation into the Z-$\mathcal{Y}$ space, specially in the lowest strain rate due to high amounts of soot. The soot rates are stored in a very narrow location of the manifold (yet to be presented) and to be able to capture all these rates the FGM database is increased in size. So in this section the database is discretized with a 400 X 400 (Z and $\mathcal{Y}$) equidistant grid.

Figure 5.8 show the temperature, the progress variable source term, $Y_{C_2H_4}$ and $Y_{C_2H_2}$, as they are stored in the manifold, as function of Z and $\mathcal{Y}$. Comparing this figure

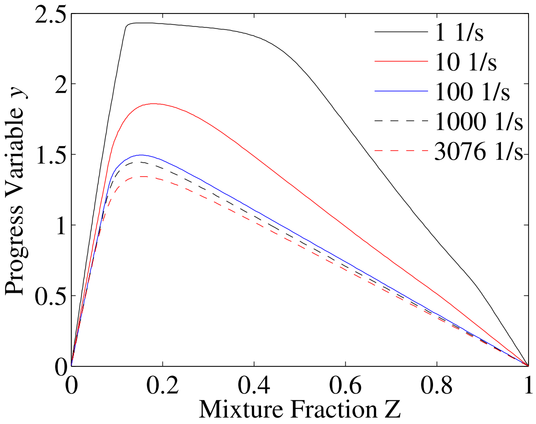

Figure 5.7: Steady flamelets in the Z and $\mathcal{Y}$ space;

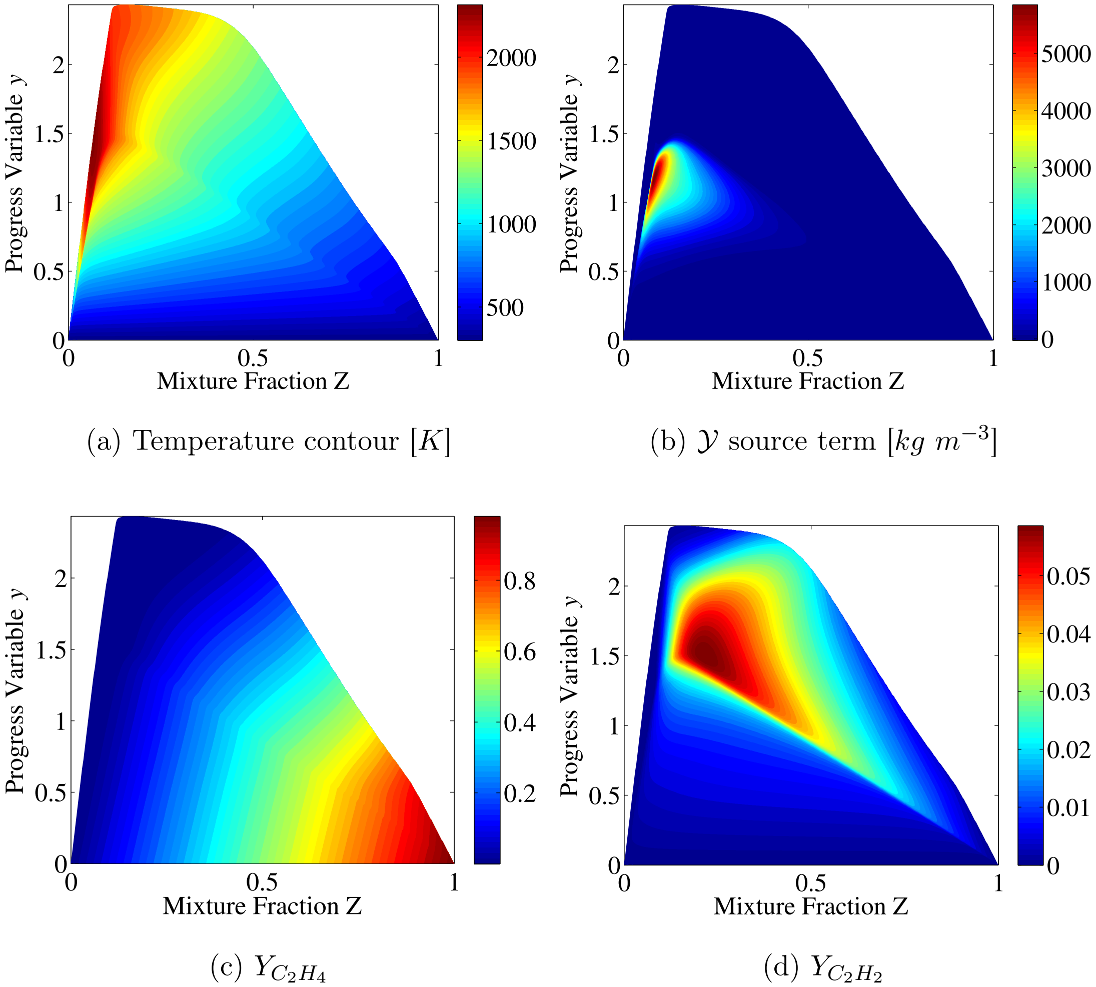

(a) Temperature contour $[K]$

(b) $\mathcal{Y}$ source term $[kg\ m^{-3}]$

(c) $Y_{C_2H_4}$

(d) $Y_{C_2H_2}$

Figure 5.8: Manifold with soot visualization; Variables as function of (Z and $\mathcal{Y}$)

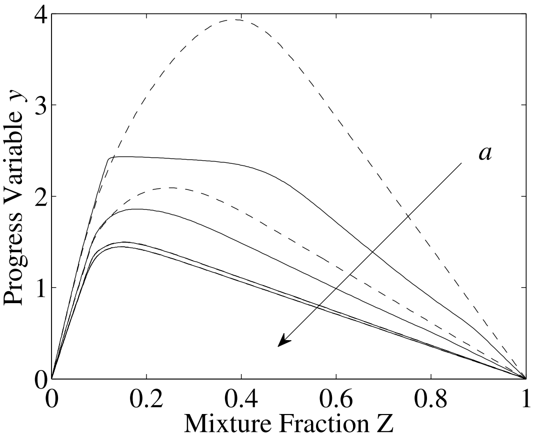

Figure 5.9: Comparison of FGM and detailed solution for flamelets at $a = 1$, 10, 100 and 1000 s^{-1}; dash line: FGM solution; solid line: detailed solution;

to the gas solution manifold (Figure 5.3) it is possible to see that the soot inclusion alters significantly the species distribution in the database.

5.2.2.1 FGM Verification in one-dimensional flames:

The FGM method is applied to solve four ethylene counterflow flamelets, $a =$ 1, 10, 100 and 1000 s^{-1}, and compared to the detailed solution. The comparison on the controlling variables space are shown in Figure 5.9. The FGM solution does not agrees with the detailed solution for the lowest strain rates, in which the soot formation is extremely high ($Y_{S,max} = 0.35$). This is probably due to the inclusion of soot in the mixture fraction definition. The transport coefficient for the Z conservation equation does not respect the unity Lewis number assumption anymore. Thus, large discrepancies are found specially when high amounts of soot are present. Despite the fact that the method disagrees with the one-dimensional detailed solution in the region with low strain rate it is expected that the two-dimensional solution of the coflow flame does not frequently access that area with high amounts of soot. Thus, this option will be further explored in two-dimensional simulations.

5.2.2.2 FGM Verification in two-dimensional flame:

The FGM method is then used to solve the two-dimensional ethylene flame. The Z and $\mathcal{Y}$ fields are compared in Figure 5.10. Similar to the results of one-dimensional flame verification, the solution of both controlling variable equations retained similar profiles of the detailed result, but it could not reproduce the correct thermo-chemical solution. It is interesting to see that the soot formation significantly alters the transport of Z in the detailed solution, which is not captured by the FGM solution. Clearly the transport of mixture fraction is not ruled by unity Lewis number approximation anymore. Another important aspect is that the FGM solution could not recreate the progress variable field of the detailed result. Many tests with different definitions of the $\mathcal{Y}$ were done, but none could improve the result. Due to current limitation of the author's knowledge on improving the $\mathcal{Y}$ definition it is decide to move forward with the present model keeping in mind that some discrepancies may arise with this choice.

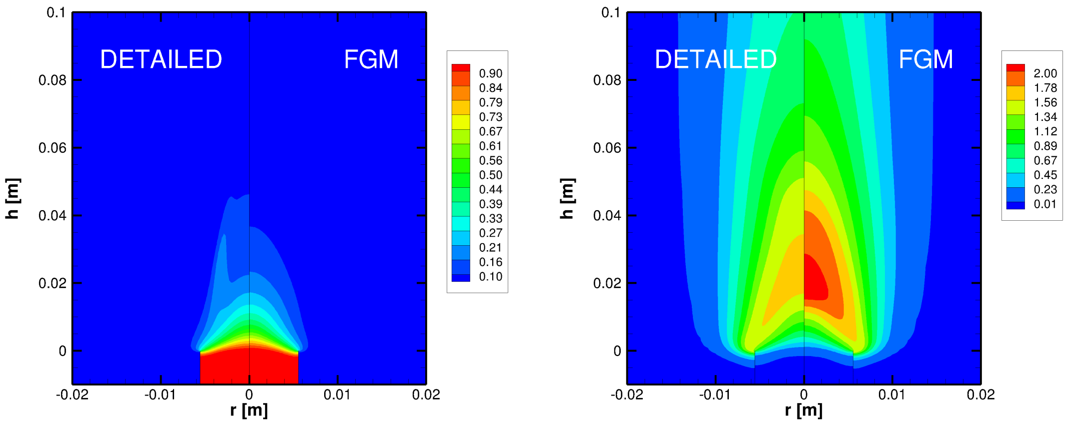

(a) Mixture fraction Z

(b) Progress variable $\mathcal{Y}$

Figure 5.10: Comparison between detailed solution and FGM solution for an adiabatic ethylene coflow flame with soot.

The verification is followed by a comparison of the axial velocity, radial velocity, temperature, $Y_{C_2H_4}$, Y_{O_2} and $Y_{C_2H_2}$, shown in the Figure 5.11.

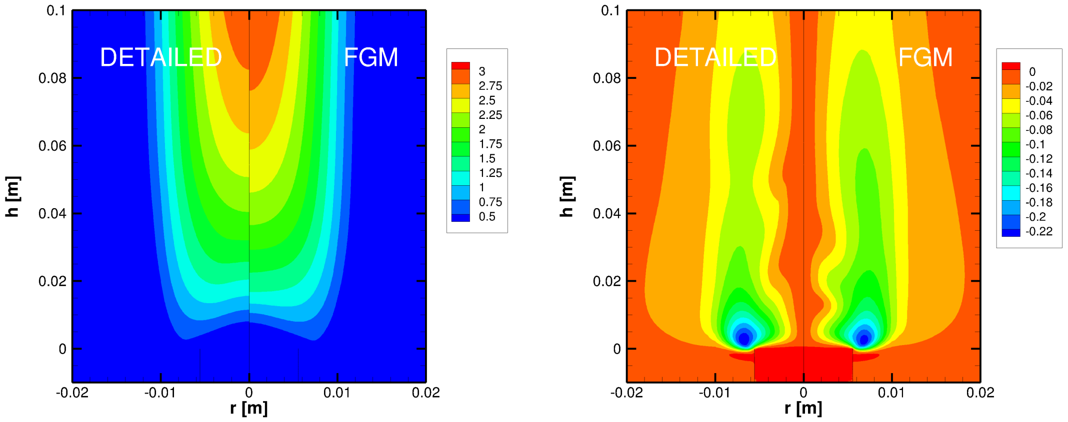

(a) Axial velocity $[m/s]$ (b) Radial velocity $[m/s]$

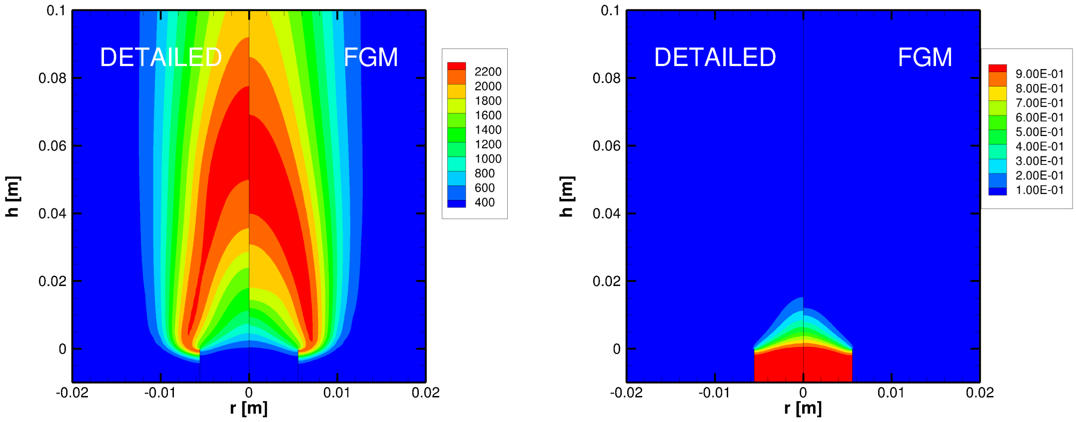

(c) Temperature $[K]$ (d) $Y_{C_2H_4}$

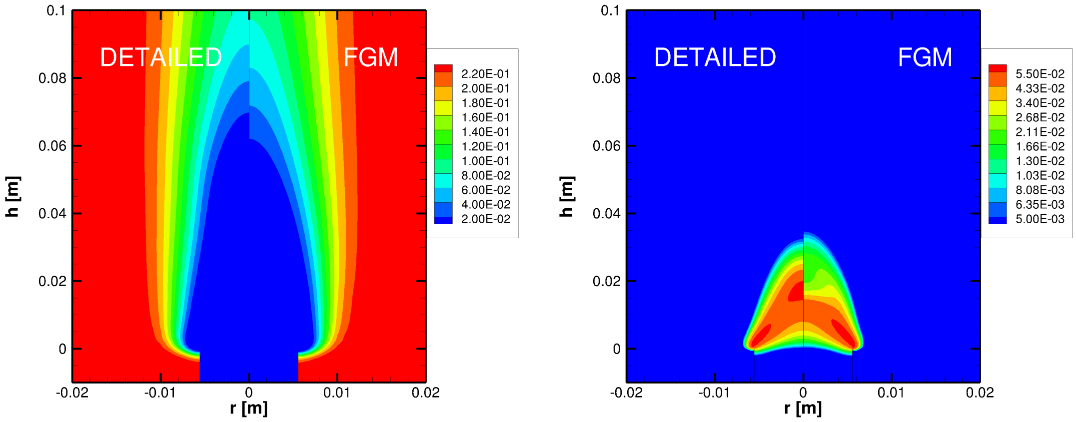

(e) Y_{O_2} (f) $Y_{C_2H_2}$

Figure 5.11: Comparison between detailed solution and FGM solution for an adiabatic ethylene coflow flame with soot

The FGM and the detailed results are qualitatively similar, but important discrepancies were found between the solutions. The maximum values for temperature are close $T_{FGM,max} = 2324\ K$ and $T_{detailed,max} = 2365\ K$, and even the maximum predicted acetylene mass fractions were almost equal, $Y_{C_2H_2,FGM,max} = 0.059$ and $Y_{C_2H_2,detailed,max} = 0.060$. However, the spatial distributions are still not in an acceptable agreement with the reference. Most of the FGM contours are being shifted downwards, what is clearly seen in the axial velocity, temperature, C_2H_4 and O_2 profiles. For the acetylene profile, the discrepancies found will certainly affect the soot production and a poor comparison with the detailed model can be anticipated. Nevertheless, the study of soot retrieval options will proceed with the present manifold. Latter an attempt to enhance the manifold performance will be explored.

Retrieving Y_S from manifold:

In this approach, the value of Y_S is stored and retrieved directly from the manifold and no additional equation must be solved. The Figure 5.12 show how the Y_S is stored in the manifold and Figure 5.13 show the comparison between detailed solution and FGM solution for Y_S contour.

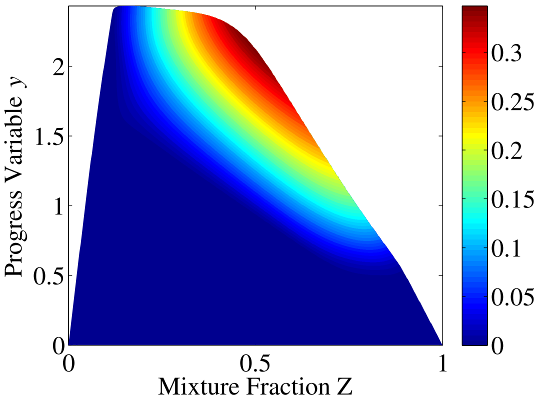

Figure 5.12: Y_S stored in the manifold

The soot mass fraction is well discretized in the database, shown in Figure 5.12, and so no problem on the access and interpolation procedure is expected. Figure 5.13 show that the method of retrieving the soot mass fraction directly from the manifold does not capture the correct formation and transport of soot mass fraction despite the fact that the maximum value is similar, $Y_{S,FGM,max} = 0.1126$ and $Y_{S,detailed,max} = 0.1189$. This

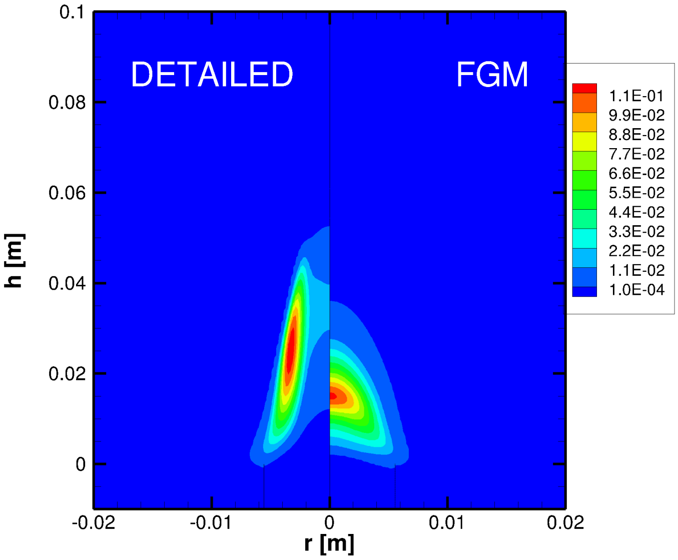

Figure 5.13: Y_S contour, when retrieving Y_S from manifold

problem is commonly found for species that evolve in a slower rate when compared to other species in the manifold. This is the case of NOx, for example van Oijen et al., 2016. In these cases the introduction of an additional transport equation for the slow species may solve the problem.

Retrieving soot source terms from manifold:

In this method, the total source terms for Y_S and N_S are stored in the database and later retrieved when solving soot transport equations. Figure 5.14 shows how the source terms are stored and Figure 5.15 shows the result for this approach.

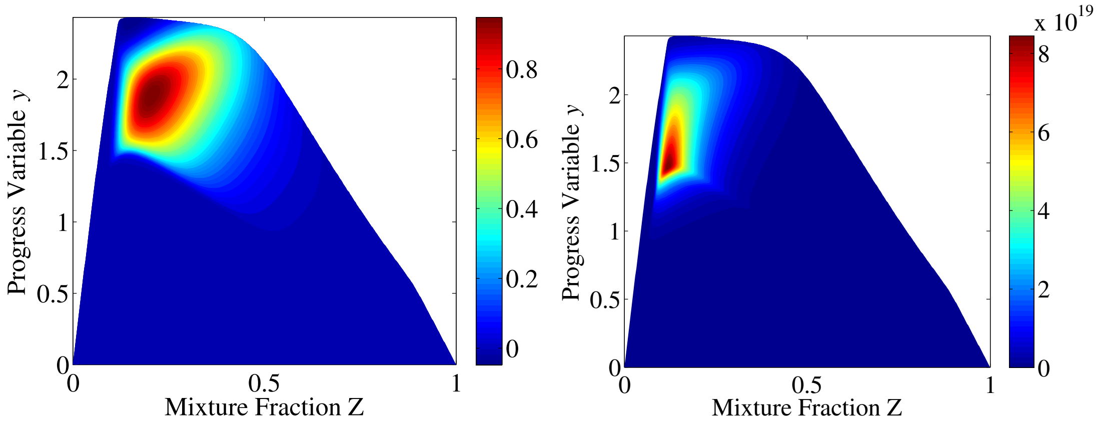

(a) Source term of Y_S $[kg\ m^{-3}s^{-1}]$ (b) Source term of N_S $[particles\ m^{-3}s^{-1}]$

Figure 5.14: Source term for Y_S and N_S stored in the manifold

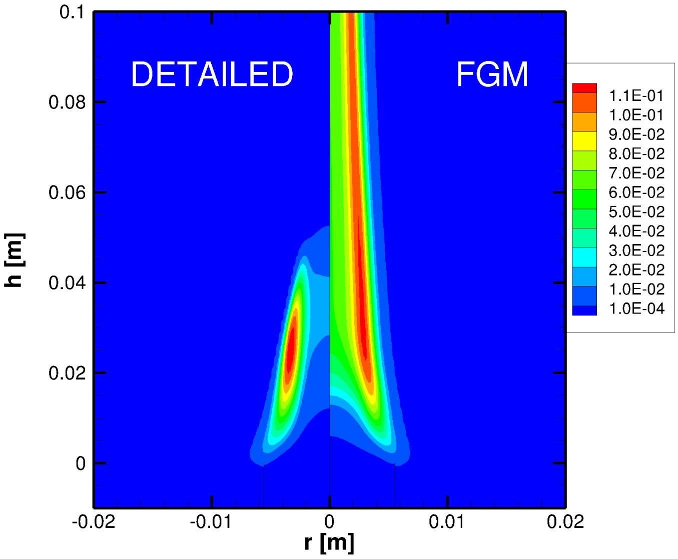

Figure 5.15: Y_S contour, when retrieving source terms for Y_S and N_S from manifold

When compared to the first approach the current method was somewhat able to capture the slow process of soot formation, as shown in the Figure 5.15. However it failed to capture the oxidation process, despite that either source terms are relatively well discretised in the manifold as shown in Figure 5.14. The maximum values for soot mass fraction found were similar $Y_{S,FGM,max} = 0.1135$ and $Y_{S,detailed,max} = 0.1189$.

Retrieving specific rates from manifold:

In this approach the soot transport equations are solved and each reaction rate is retrieved from the manifold. As the Y_S and N_S are now being solved its evolution might affect the soot rates that are based on the soot specific area. So the method suggested by Balthasar et al., 1996, and Carbonell et al., 2009, is used, where the oxidation soot rates are stored as function of the specific soot surface area, S ($m^2\ m^{-3}$) and the soot surface growth rate as function of $\sqrt{S}$. The soot rates are shown in the Table 5.1 and how they are stored is shown in Figure 5.16.

Table 5.1: Stored soot reactions in the manifold

Reaction		Stored Rates
Nucleation	$C_2H_2 \rightarrow 2C_S + H_2$	R_1
Surf. Growth	$C_2H_2 + nC_S \rightarrow (n+2)\,C_S + H_2$	$R_2/\sqrt{S}$
Oxid. by O_2	$C_S + \frac{1}{2}O_2 \rightarrow CO$	R_3/S
Oxid. by OH	$C_S + OH \rightarrow CO + H$	R_4/S
Oxid. by O	$C_S + O \rightarrow CO$	R_5/S

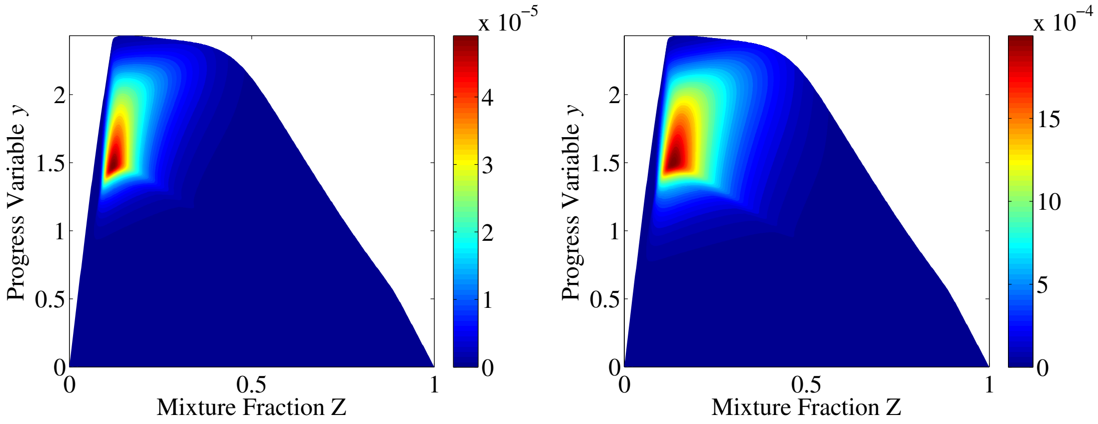

(a) R_1 (b) $R_2/\sqrt{S}$

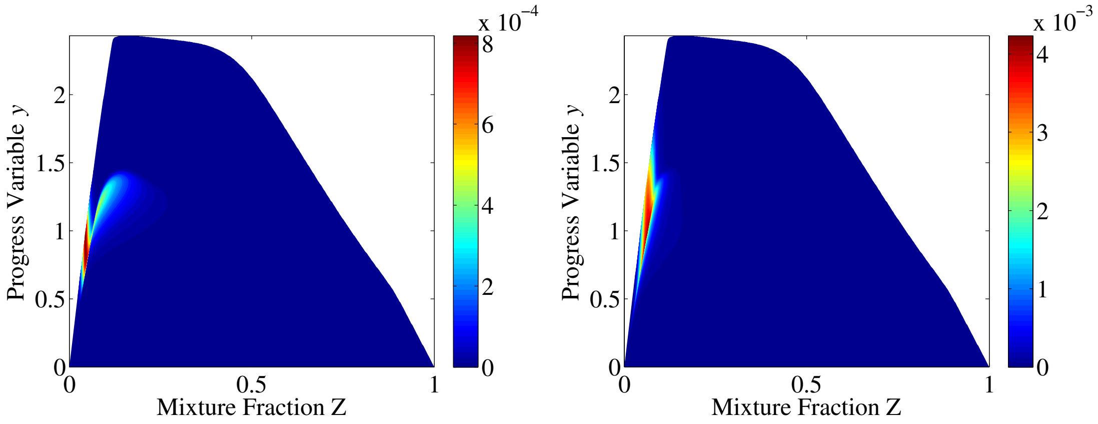

(c) R_3/S (d) R_4/S

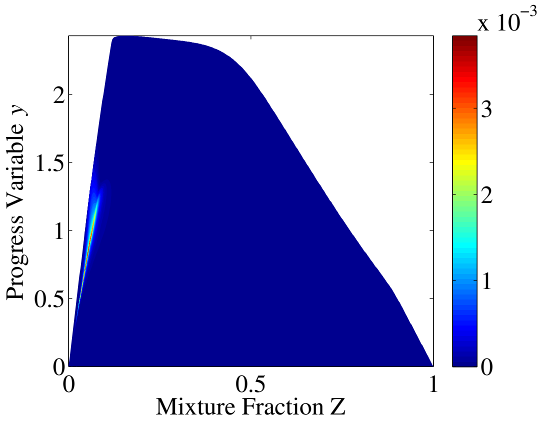

(e) R_5/S

Figure 5.16: Soot rates stored in the manifold

The rates of soot formation (nucleation and surface growth) are relative well discretized in the manifold, as shown in Figure 5.16 a) and b). However the oxidation rates are located in a very narrow portion of the database and so the retriveing procedure of those rates may be affected. The result of this approach is then presented in the Figure 5.17.

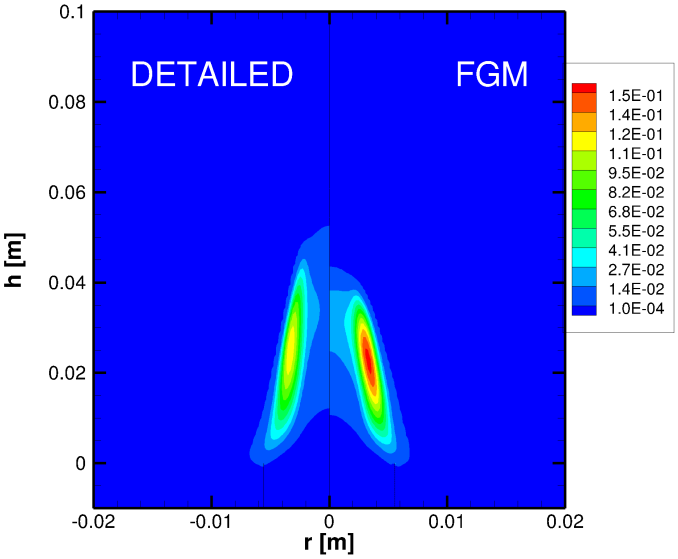

Figure 5.17: Y_S contour, when retrieving soot rates from manifold

The present method is able to capture the slow process of soot formation and oxidation. The maximum soot mass fraction are close, $Y_{S,FGM,max} = 0.1567$ and $Y_{S,detailed,max} = 0.1189$. The spatial soot distribution predicted by the FGM solution is very similar but not the same as the detailed case. The FGM solution is, as discussed earlier, still dependent to the correct transport of mixture fraction and the proper definition of $\mathcal{Y}$. Also the low level of discretisation of soot oxidation rates in the manifold might be the cause of higher production of soot.

5.2.3 Improvement of the soot description in FGM simulations

In this section, an attempt to improve the results of both controlling variables (Z and $\mathcal{Y}$) is done. Soot is not included in the species transport and properties workflow, but the conservation of mass and energy is still guaranteed. This means that the mixture fraction Z only refers to the gas-phase species. It is important to say that this approach is not totally accurate since Z is not conserved, because there is no track of the elements that pass from gas- to the solid-phase and vice-versa in the soot formation processes and in the soot oxidation processes. So this approach is still expected to give some errors, specially in the region with high soot formation. A new manifold is then created using the same limits as previous section. Also a new progress variable composition is set as:

$$\mathcal{Y} = 0.9\alpha_{CO_2}Y_{CO_2} + \alpha_{H_2O}Y_{H_2O} + 0.9\alpha_{CO}Y_{CO} + \alpha_{H_2}Y_{H_2} + \alpha_{C_2H_2}Y_{C_2H_2} \tag{5.5}$$

This progress definition lead to unique map of the dependent variables.

5.2.3.1 FGM Verification in one-dimensional flames:

The same one-dimensional validation presented in previous section is shown in Figure 5.18 for the new manifold. Now that the mixture fraction tracks only the gas-phase species and the manifold is less influenced than the previous manifold by the soot formation, as shown in 5.18. It is also possible to see that the solution of FGM equations results in a better agreement with the detailed solution. Nevertheless there are still some

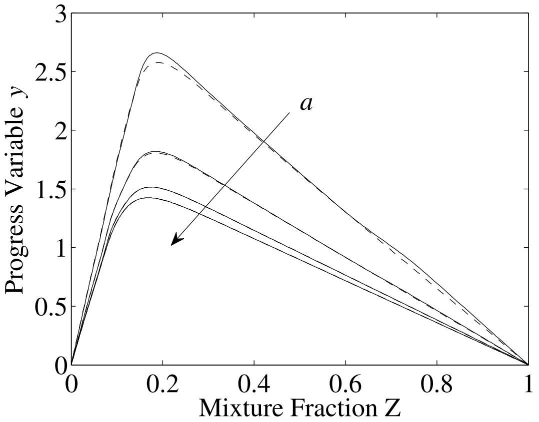

Figure 5.18: Comparison of FGM and detailed solution for flamelets at $a = 1$, 10, 100 and 1000 s^{-1}; FGM: dash line ; detailed: solid line;

deviation specially in the flamelets with the lowest strain rate.

5.2.3.2 FGM Verification in two-dimensional flame:

The new manifold is then used to solve the two-dimensional ethylene flame. The Z and $\mathcal{Y}$ fields are compared in Figure 5.19. A small improvement was achieved with the current manifold. The biggest diffence is still in the $\mathcal{Y}$ contour, which means that the current definition is inadequate to track the chemical evolution of the system when containing a great quantity of soot. The comparison with the detailed solution in the physical space for the axial velocity, radial velocity, temperature, $Y_{C_2H_4}$, Y_{O_2} and $Y_{C_2H_2}$ is shown in the Figure 5.20.

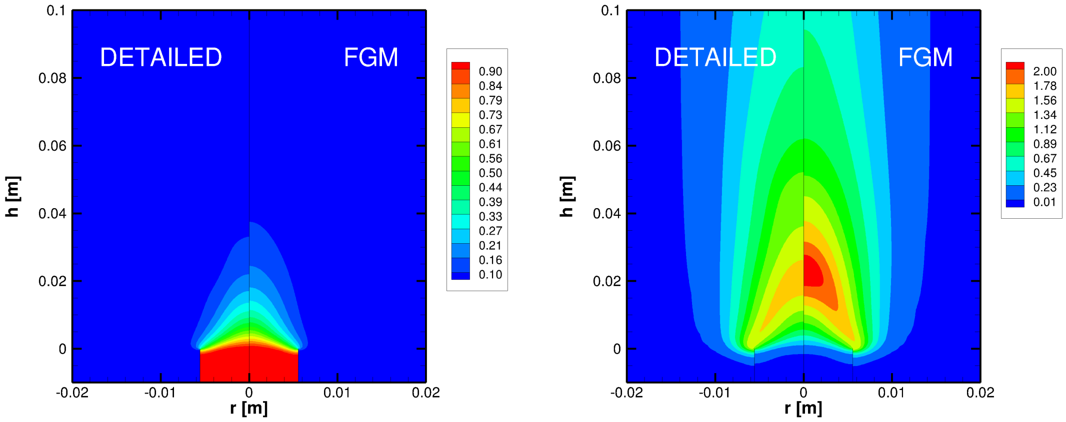

(a) Mixture fraction Z

(b) Progress variable $\mathcal{Y}$

Figure 5.19: Comparison between detailed solution and FGM solution for an adiabatic ethylene coflow flame with soot.

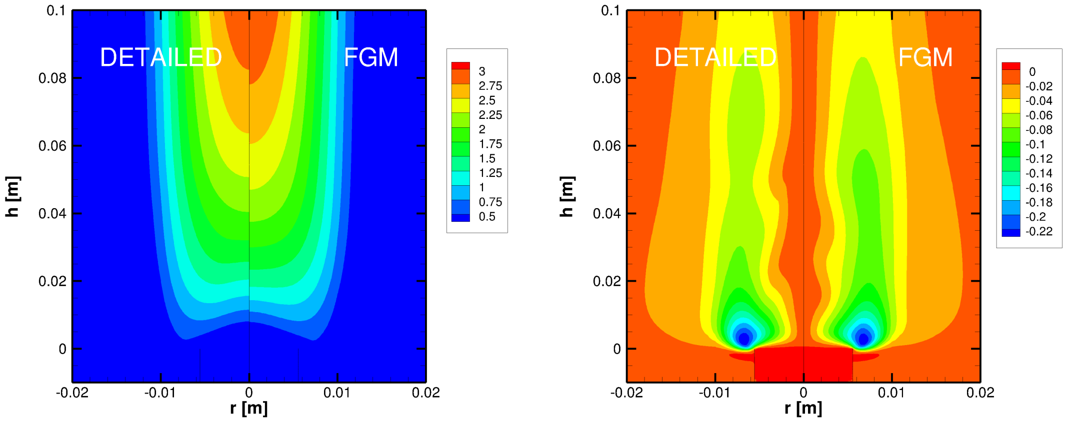

(a) Axial velocity $[m/s]$ (b) Radial velocity $[m/s]$

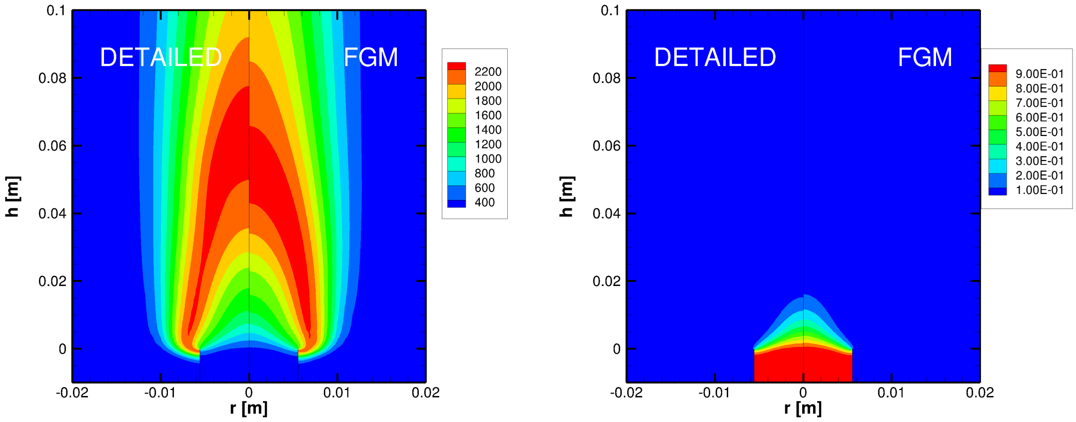

(c) Temperature $[K]$ (d) $Y_{C_2H_4}$

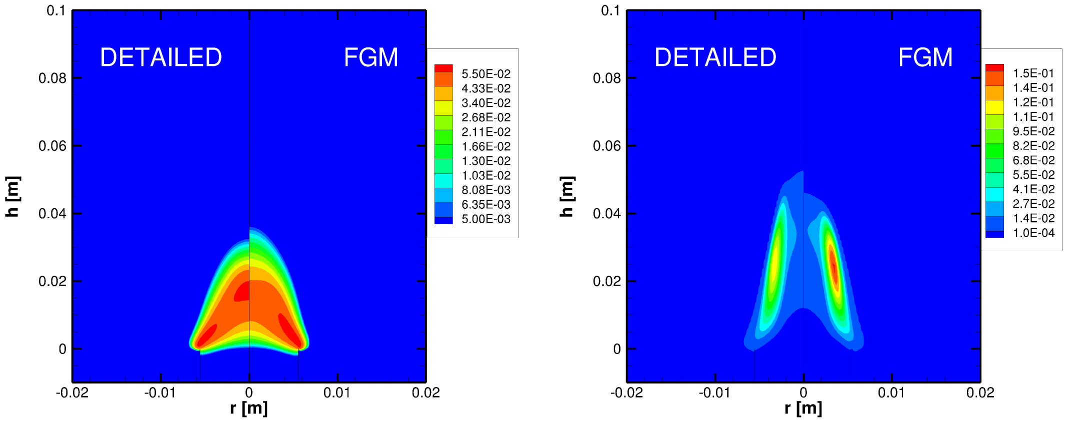

(e) $Y_{C_2H_2}$ (f) Y_S contour (retrieving soot rates)

Figure 5.20: Comparison between detailed solution and FGM solution for an adiabatic ethylene coflow flame with soot

Again a small improvement that can be seen in the improved profiles of temperature, $Y_{C_2H_4}$, $Y_{C_2H_2}$ and Y_S, specially near the fuel exit area.

Figure 5.21 show the comparison of the total amount of soot, integrated in the flame cross section, predicted by the detailed case, the previous FGM solution (FGM 1) and the current FGM solution (FGM 2).

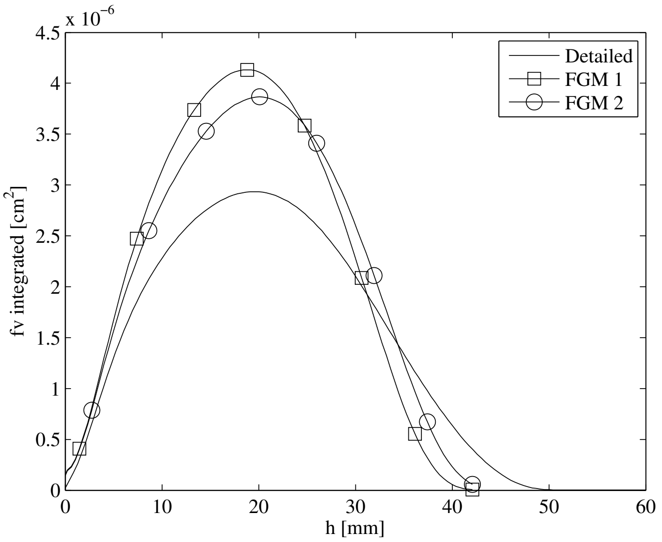

Figure 5.21: Comparison of $f_{v,integrated}$ between FGM and detailed solutions

It is possible to see that the current FGM solution (FGM 2) enhanced the soot predictions, reducing the peak of soot formation, but is still lacking of accuracy when compared to the detailed solution.

The results presented show that the method for inclusion of soot model in the FGM method may provide good results, but the current implementation still needs further improvements. Some advances can be suggested: first, in the description of the transport of Z, which could account for the two-phases or could account for the preferential diffusion due to soot transport; and second, in better discretisation of the soot rates in the manifold which can be achieved with a more suitable progress variable definition.

5.3 Conclusion:

In this chapter the reduction technique FGM was presented and applied to predict soot formation in an atmospheric ethylene coflow flame. A semi-empirical two equation model is chosen for predicting soot mass fraction and number density. The model describes particle nucleation, surface growth and oxidation. For the gas-phase a detailed kinetic mechanism is considered. Unity Lewis number approximation and simplified model for transport properties were used. The model was implemented in a commercial CFD and assessed against to a detailed chemistry solution. For simplicity no heat loss was considered.

The target flame in this chapter was similar to the atmospheric pressure, non-smoking ethylene/air coflow diffusion flame of Santoro et al., 1983, but in adiabatic conditions. In order to assess the ability of the FGM method it was first applied to a gas-phase solution, i.e. without production of soot. The results presented by the FGM method were in very good agreement with the detailed chemistry solution, apart from a minor deviation in the C_2H_2.

Regarding to soot modeling using FGM, three methods were tested. The best approach was to to solved all flamelets with soot and gas-phase species in a coupled manner, and to store the soot rates in the manifold. In the two-dimensional simulations, additional equations for soot modeling must be solve and the soot rates are retrieved from the manifold. The results presented show a good qualitative agreement with the detailed solution, but further improvements must be made. First, in the description of the transport of Z, which could account for the two-phases or could account for the preferential diffusion due to soot transport; and second, in an improvement of the $\mathcal{Y}$ definition, which lead to a better track of the chemical evolution of the system and a better discretisation of the soot rates in the manifold.

The presented methodology for modeling soot production with the FGM technique is still in development. The present results demonstrated the great potential of the method for predicting soot formation in multidimensional ethylene diffusion flames with reduced computational time.

6 CONCLUSIONS

In this thesis, a series of numerical methods were used to study soot formation in laminar flames, ranging from one-dimensional adiabatic counterflow flames with simplified transport properties to two-dimensional co-flow flames with heat loss and detailed transport properties. The Flamelet Generated Manifold reduction technique was also explored in order to reduce computational burden while keeping a good prediction of the chemical kinetics. A framework for the study of soot formation and its interaction with the gas-phase species in ethylene flames was created by implementing and comparing complex and simple models.

First, the mass and energy coupling terms between the gas and solid phases in one-dimensional ethylene counterflow flames were investigated in Chapter 3. A semi-empirical two equation model was chosen for predicting soot mass fraction and number density. The model described particle nucleation, surface growth and oxidation. It was implemented in the CHEM1D code and assessed against experimental data. For the gas-phase a detailed kinetic mechanism was considered. Additionally, the effect of considering gas and soot radiation heat losses was evaluated in the optically thin limit approximation. Simulations were done for a range of conditions that produced low to significant amounts of soot. To achieve these conditions three strategies were adopted. First, at atmospheric pressure, the strain rate, was varied from low to high values, with the lower values resulting in larger residence times and, consequently, in higher soot formation. Second, for a particular strain rate and atmospheric pressure, the oxygen content in the oxidizer stream was increased, which led to higher flame temperatures and, consequently, higher soot production. Third, for a specific strain rate, the pressure was increased, also resulting in higher soot production. Additionally, the effect of simplified transport properties model was analyzed. It was found that the gas and soot radiation terms are of primary importance for flame simulations. The importance of the radiation heat loss on soot predictions shown here was consistent with the literature, even though some works were in different configurations. The additional coupling terms (mass and thermodynamic properties) are generally a second order effect, but their importance increase as the soot amount increases. The comparison with experiments showed that the soot predictions of the model were in good qualitative agreement. As a general recommendation, the full coupling should be taken into account only when the soot mass fraction, Y_S, is equal to or larger than 0.008. However, if a higher precision is required, with errors lower than 1%, the full coupling should be taken into account when $Y_S \geq 0.002$, which is the lower threshold of the most sensitive gas species, H_2. The non-coupled model could not represent the soot mass fraction predicted by the coupled model with errors lower than 1%. For lower soot amount, the coupling through soot mass and thermodynamic properties may be neglected as a first approximation, remembering that an error in the local mass conservation will be present. The results also showed that discrepancies in choosing different transport models (detailed or simplified) are larger than those found from not fully coupling the phases.

Subsequently, in Chapter 4, the soot modeling was applied to two-dimensional ethylene co-flow flames with detailed chemical kinetics and the effect of different transport models on soot predictions was again explored. The same semi-empirical two equation model, with minor changes, was chosen for predicting soot mass fraction and number density. For the gas-phase a detailed kinetic mechanism was considered. The model was implemented in a commercial CFD and assessed against experimental data from the literature. The effect of choosing different transport models (detailed or simplified), also with considering gas and soot radiation heat losses were evaluated in the optically thin limit approximation. The comparison with experimental data showed that the model predicted the behavior of soot formation, with values in the same order as the experimental data, but the exact values of f_v were not found. Some aspects in the numerical modeling were found to have impact on soot predictions and could further investigated in future works. For example, the fuel stream preheating changes the temperature and velocity profile at the injector exit plane, the choice of the gas-phase kinetic mechanism have an impact on soot predictions and there are some intrinsic limitations of the chosen soot model (semi-empirical) and the parameters of the its soot reactions. Additionally, it was found that the gas and soot radiation terms were also of primary importance for flame simulations and that a first attempt to solve the two-dimensional ethylene co-flow flame could be done using a simplified transport model. If a more accurate solution is needed the solution can be resumed with detailed transport properties.

Finally, an implementation of the soot model with the FGM reduction technique was done and different forms for storing soot information in the flamelet table were explored in Chapter 5. The reduction technique FGM was applied to predict soot formation in same atmospheric ethylene counterflow (1D) and coflow (2D) flames presented in previous chapters, but only for the adiabatic condition. The same semi-empirical two equation model was used for predicting soot mass fraction and number density. For the gas-phase a detailed kinetic mechanism was also considered. Unity Lewis number approximation and simplified model for transport properties were used. The model was implemented in the CHEM1D code and in a commercial CFD and assessed against to a detailed chemistry solution. In order to assess the ability of the FGM method it was first applied to a gas-phase solution, i.e. without production of soot. The results presented by the FGM method were in very good agreement with the detailed chemistry solution, apart from a minor deviation in the C_2H_2. Regarding to soot modeling using FGM, three methods were tested. The first, was to store and retrieve the Y_S directly from the manifold. The second, was to solve the two-equation soot model, storing and retrieving the total source term for Y_S and N_S from the manifold. The third, was to solve the two-equation soot model, storing and retrieving the specific soot rates for Y_S and N_S from the manifold. The best option was the third, so all flamelets with soot and gas-phase species were solved in a coupled manner, and the soot rates in terms of specific surface area were stored in the manifold. The results obtained showed a good qualitative agreement with the detailed solution, but further improvements must be made. First, in the description of the transport of Z, which could account for the two-phases or could account for the preferential diffusion due to soot transport; and second, in better definition of $\mathcal{Y}$ which lead to a better track of the chemical evolution of the system and a better discretization of the soot rates in the manifold. The presented methodology for modeling soot production with the FGM technique is still in development. The presented results have demonstrated the potential of the method for predicting soot formation in multidimensional ethylene diffusion flames with lower computational cost.

In conclusion, the contributions of this thesis are:

1. It was found a condition for which a full description of the gas and solid-phase interactions is mandatory.
2. It was shown the impact of different transport models and heat losses in soot predictions.

3. It was shown the best method for storing soot information in the FGM tables to appropriately simulate high soot loads.

BIBLIOGRAPHY

Appel, J., Bockhorn, H., and Frenklach, M. Kinetic modeling of soot formation with detailed chemistry and physics: laminar premixed flames of C2 hydrocarbons, **Combustion and Flame**, vol. 121(1–2), p. 122 – 136, 2000.

Arana, C. P., Pontoni, M., Sen, S., and Puri, I. K. Field measurements of soot volume fractions in laminar partially premixed coflow ethylene/air flames, **Combustion and Flame**, vol. 138(4), p. 362 – 372, 2004.

Balthasar, M. and Frenklach, M. Monte-Carlo simulation of soot particle coagulation and aggregation: the effect of a realistic size distribution, **Proceedings of the Combustion Institute**, vol. 30(1), p. 1467 – 1475, 2005.

Balthasar, M., Heyl, A., Mauß, F., Schmitt, F., and Bockhorn, H. Flamelet modeling of soot formation in laminar ethyne/air-diffusion flames, **Symposium (International) on Combustion**, vol. 26(2), p. 2369 – 2377, 1996.

Barlow, R., Karpetis, A., Frank, J., and Chen, J.-Y. Scalar profiles and NO formation in laminar opposed-flow partially premixed methane/air flames, **Combust. Flame**, vol. 127(3), p. 2102 – 2118, 2001.

Battin-Leclerc, F., Simmie, J. M., and Blurock, E. **Cleaner Combustion**. Springer, 2013.

Bennett, B. A. V., McEnally, C. S., Pfefferle, L. D., Smooke, M. D., and Colket, M. B. Computational and experimental study of the effects of adding dimethyl ether and ethanol to nonpremixed ethylene/air flames, **Combustion and Flame**, vol. 156(6), p. 1289 – 1302, 2009.

Bilger, R. The structure of turbulent nonpremixed flames, **Symposium (International) on Combustion**, vol. 22(1), p. 475 – 488, 1989.

Bird, R., Stewart, W., and Lightfoot, E. **Transport Phenomena**. Wiley, 2002.

Blanquart, G., Pepiot-Desjardins, P., and Pitsch, H. Chemical mechanism for high temperature combustion of engine relevant fuels with emphasis on soot precursors, **Combustion and Flame**, vol. 156(3), p. 588 – 607, 2009.

Bodenstein, M. Eine theorie der photochemischen reaktionsgeschwindigkeiten, **Z. phys. Chem**, vol. 85(329), p. 0022–3654, 1913.

Bradley, D., Dixon-Lewis, G., din Habik, S. E., and Mushi, E. The oxidation of graphite powder in flame reaction zones, **Symposium (International) on Combustion**, vol. 20(1), p. 931 – 940, 1984.

Carbonell, D., Oliva, A., and Perez-Segarra, C. Implementation of two-equation soot flamelet models for laminar diffusion flames, **Combustion and Flame**, vol. 156(3), p. 621 – 632, 2009.

Chapman, S. and Cowling, T. G. **The mathematical theory of non-uniform gases: an account of the kinetic theory of viscosity, thermal conduction and diffusion in gases**. Cambridge university press, 1970.

Charest, M. R., Groth, C. P., and Gülder, Ö. L. A computational framework for predicting laminar reactive flows with soot formation, **Combustion Theory and Modelling**, vol. 14(6), p. 793–825, 2010.

Charest, M. R., Gülder, Ö. L., and Groth, C. P. Numerical and experimental study of soot formation in laminar diffusion flames burning simulated biogas fuels at elevated pressures, **Combustion and Flame**, vol. 161(10), p. 2678 – 2691, 2014.

Charest, M. R. J. **Numerical modelling of sooting laminar diffusion flames at elevated pressures and microgravity**. PhD thesis, University of Toronto, 2011.

Chase Jr., M. W. NIST-JANAF Thermochemical Tables, **Journal of Physical and Chemical Reference Data**, vol. Fourth Edition(Monograph 9), 1998.

CHEM1D. **One-dimensional laminar flame code**. Eindhoven Technological University. `http://www.combustion.tue.nl/`, 2016.

Chen, D., Zainuddin, Z., Yapp, E., Akroyd, J., Mosbach, S., and Kraft, M. A fully coupled simulation of PAH and soot growth with a population balance model, **Proceedings of the Combustion Institute**, vol. 34(1), p. 1827 – 1835, 2013.

Chen, J., Liu, Y., and Rogg, B. **CO-H2-N2/Air Diffusion Flames: Thermal Radiation and Transient Effects**. In Peters, N. and Rogg, B., editors, *Reduced Kinetic Mechanisms for Applications in Combustion Systems*, volume 15, pages 196–223. Springer, 1993.

Chernov, V., Thomson, M. J., Dworkin, S. B., Slavinskaya, N. A., and Riedel, U. Soot formation with C1 and C2 fuels using an improved chemical mechanism for PAH growth, **Combustion and Flame**, vol. 161(2), p. 592 – 601, 2014.

Coelho, P. and Costa, M. **Combustão**. Edições Orion, 2007.

Coffee, T. and Heimerl, J. Transport algorithms for premixed, laminar steady-state flames, **Combustion and Flame**, vol. 43(0), p. 273 – 289, 1981.

Crowe, C. T. **Multiphase Flow Handbook**. CRC Press, Taylor Francis Group, 2006.

D'Anna, A. and Kent, J. Modeling of particulate carbon and species formation in coflowing diffusion flames of ethylene, **Combustion and Flame**, vol. 144(1–2), p. 249 – 260, 2006.

de Goey, L. P. H. and ten Thije Boonkkamp, J. H. M. A flamelet description of premixed laminar flames and the relation with flame stretch, **Combustion and Flame**, vol. 119(3), p. 253–271, 1999.

Delhaye, S., Somers, L., van Oijen, J., and de Goey, L. Incorporating unsteady flow-effects in flamelet-generated manifolds, **Combustion and Flame**, vol. 155(1–2), p. 133 – 144, 2008.

Demarco, R., Nmira, F., and Consalvi, J. Influence of thermal radiation on soot production in Laminar axisymmetric diffusion flames, **Journal of Quantitative Spectroscopy and Radiative Transfer**, vol. 120, p. 52 – 69, 2013.

Domenico, M. D., Gerlinger, P., and Aigner, M. Development and validation of a new soot formation model for gas turbine combustor simulations, **Combustion and Flame**, vol. 157(2), p. 246 – 258, 2010.

Dworkin, S. B., Zhang, Q., Thomson, M. J., Slavinskaya, N. A., and Riedel, U. Application of an enhanced PAH growth model to soot formation in a laminar coflow ethylene/air diffusion flame, **Combustion and Flame**, vol. 158(9), p. 1682 – 1695, 2011.

Eaves, N., Dworkin, S., and Thomson, M. The importance of reversibility in modeling soot nucleation and condensation processes, **Proceedings of the Combustion Institute**, vol. 35(2), p. 1787 – 1794, 2015.

Eaves, N. A., Thomson, M. J., and Dworkin, S. B. The Effect of Conjugate Heat Transfer on Soot Formation Modeling at Elevated Pressures, **Combustion Science and Technology**, vol. 185(12), p. 1799–1819, 2013.

EPE. **Brazilian Energy Balance 2016 Year 2015,**. Technical report, Empresa de Pesquisa Energética (EPE), 2016.

Ezekoye, O. and Zhang, Z. Soot oxidation and agglomeration modeling in a microgravity diffusion flame, **Combustion and Flame**, vol. 110(1–2), p. 127 – 139, 1997.

Fairweather, M., Jones, W., and Lindstedt, R. Predictions of radiative transfer from a turbulent reacting jet in a cross-wind, **Combustion and Flame**, vol. 89(1), p. 45 – 63, 1992.

Fiorina, B., Gicquel, O., Vervisch, L., Carpentier, S., and Darabiha, N. Approximating the chemical structure of partially premixed and diffusion counterflow flames using FPI flamelet tabulation, **Combustion and Flame**, vol. 140(3), p. 147 – 160, 2005.

Fluent, A. **16.1 Theory Guide**, 2015.

Frenklach, M. Method of moments with interpolative closure, **Chemical Engineering Science**, vol. 57(12), p. 2229 – 2239, 2002.

Gicquel, O., Darabiha, N., and Thévenin, D. Liminar premixed hydrogen/air counterflow flame simulations using flame prolongation of ILDM with differential diffusion, **Proceedings of the Combustion Institute**, vol. 28(2), p. 1901 – 1908, 2000.

Giovangigli, V. Convergent iterative methods for multicomponent diffusion, **IMPACT of Computing in Science and Engineering**, vol. 3(3), p. 244 – 276, 1991.

Guo, H., Liu, F., Smallwood, G., and Gulder, O. L. The flame preheating effect on numerical modelling of soot formation in a two-dimensional laminar ethylene-air diffusion flame, **Combustion Theory and Modelling**, vol. 6(2), p. 173–187, 2002.

Hall, R. J. Radiative dissipation in planar gas-soot mixtures, **J. Quant. Spectrosc. Ra.**, vol. 51(4), p. 635–644, 1994.

Hirschfelder, J. O., Curtiss, C. F., Bird, R. B., et al. **Molecular theory of gases and liquids**. volume 26. Wiley New York, 1954.

Hwang, J. and Chung, S. Growth of soot particles in counterflow diffusion flames of ethylene, **Combust. Flame**, vol. 125(1), p. 752–762, 2001.

IEA. **Key World Energy Statistics**. Technical report, International Energy Agency, 2016.

Ihme, M., Shunn, L., and Zhang, J. Regularization of reaction progress variable for application to flamelet-based combustion models, **Journal of Computational Physics**, vol. 231(23), p. 7715 – 7721, 2012.

ISF. **International Sooting Flame (ISF) Workshop**. `http://www.adelaide.edu.au/cet/isfworkshop/data-sets/laminar/`, 2016.

Iyer, S. S., Litzinger, T. A., Lee, S.-Y., and Santoro, R. J. Determination of soot scattering coefficient from extinction and three-angle scattering in a laminar diffusion flame, **Combustion and Flame**, vol. 149(1–2), p. 206 – 216, 2007.

Jha, P. and Groth, C. **Evaluation of Flame-Prolongation of ILDM and Flamelet Tabulated Chemistry Approaches for Laminar Flames**. In *49th AIAA Aerospace Sciences Meeting including the New Horizons Forum and Aerospace Exposition*. American Institute of Aeronautics and Astronautics, 2011.

Kee, R. J., Dixon-Lewis, G., Warnatz, J., Coltrin, M. E., and Miller, J. A. A Fortran computer code package for the evaluation of gas-phase multicomponent transport properties, **Sandia National Laboratories Report SAND86-8246**, vol. 13, p. 80401–1887, 1986.

Kee, R. J., Rupley, F. M., and Miller, J. A. **The Chemkin Thermodynamic Data Base**. Technical report, ., 1990.

Kennedy, I. M. Models of soot formation and oxidation, **Progress in Energy and Combustion Science**, vol. 23(2), p. 95 – 132, 1997.

Kennedy, I. M., Kollmann, W., and Chen, J.-Y. A model for soot formation in a laminar diffusion flame, **Combustion and Flame**, vol. 81(1), p. 73 – 85, 1990.

Kennedy, I. M., Yam, C., Rapp, D. C., and Santoro, R. J. Modeling and measurements of soot and species in a laminar diffusion flame, **Combustion and Flame**, vol. 107(4), p. 368 – 382, 1996.

Khosousi, A. and Dworkin, S. B. Detailed modelling of soot oxidation by O2 and OH in laminar diffusion flames, **Proceedings of the Combustion Institute**, vol. 35(2), p. 1903 – 1910, 2015.

Kim, T. and Kim, Y. Interactive transient flamelet modeling for soot formation and oxidation processes in laminar non-premixed jet flames, **Combustion and Flame**, vol. 162(5), p. 1660 – 1678, 2015.

Law, C. K. **Combustion physics**. Cambridge University Press, 2006.

Lecocq, G., Poitou, D., Hernández, I., Duchaine, F., Riber, E., and Cuenot, B. A Methodology for Soot Prediction Including Thermal Radiation in Complex Industrial Burners, **Flow, Turbulence and Combustion**, vol. 92(4), p. 947–970, 2014.

Leung, K., Lindstedt, R., and Jones, W. A simplified reaction mechanism for soot formation in nonpremixed flames, **Combustion and Flame**, vol. 87(34), p. 289 – 305, 1991.

Liu, F., Guo, H., Smallwood, G. J., and Gulder, O. L. Effects of gas and soot radiation on soot formation in a coflow laminar ethylene diffusion flame, **Journal of Quantitative Spectroscopy and Radiative Transfer**, vol. 73(2-5), p. 409 – 421, 2002.

Liu, F., Guo, H., Smallwood, G. J., and Gülder, Ö. L. Numerical modelling of soot formation and oxidation in laminar coflow non-smoking and smoking ethylene diffusion flames, **Combustion Theory and Modelling**, vol. 7(2), p. 301–315, 2003.

Liu, F., Guo, H., Smallwood, G. J., and Hafi, M. E. Effects of gas and soot radiation on soot formation in counterflow ethylene diffusion flames, **Journal of Quantitative Spectroscopy and Radiative Transfer**, vol. 84(4), p. 501 – 511, 2004.

Luo, Z., Yoo, C. S., Richardson, E. S., Chen, J. H., Law, C. K., and Lu, T. Chemical explosive mode analysis for a turbulent lifted ethylene jet flame in highly-heated coflow, **Combustion and Flame**, vol. 159(1), p. 265 – 274, 2012.

Maas, U. and Pope, S. Simplifying chemical kinetics: Intrinsic low-dimensional manifolds in composition space, **Combustion and Flame**, vol. 88(3–4), p. 239 – 264, 1992.

Mason, E. A. and Saxena, S. C. Approximate Formula for the Thermal Conductivity of Gas Mixtures, **Physics of Fluids**, vol. 1(5), p. 361–369, 1958.

Mathur, S., Tondon, P., and Saxena, S. Thermal conductivity of binary, ternary and quaternary mixtures of rare gases, **Molecular physics**, vol. 12(6), p. 569–579, 1967.

Mehta, R., Haworth, D., and Modest, M. An assessment of gas-phase reaction mechanisms and soot models for laminar atmospheric-pressure ethylene–air flames, **Proceedings of the Combustion Institute**, vol. 32(1), p. 1327 – 1334, 2009.

Moss, J., Stewart, C., and Young, K. Modeling soot formation and burnout in a high temperature laminar diffusion flame burning under oxygen-enriched conditions, **Combustion and Flame**, vol. 101(4), p. 491 – 500, 1995.

Mueller, M. E. and Pitsch, H. LES model for sooting turbulent nonpremixed flames, **Combustion and Flame**, vol. 159(6), p. 2166 – 2180, 2012.

Nagle, J. and Strickland-Constable, R. Oxidation of carbon between 1000–2000 C, **Proceedings of the fifth conference on carbon**, vol. 1, p. 154–164, 1962.

Najafi-Yazdi, A., Cuenot, B., and Mongeau, L. Systematic definition of progress variables and Intrinsically Low-Dimensional, Flamelet Generated Manifolds for chemistry tabulation, **Combustion and Flame**, vol. 159(3), p. 1197 – 1204, 2012.

Peters, N. Laminar diffusion flamelet models in non-premixed turbulent combustion, **Progress in Energy and Combustion Science**, vol. 10(3), p. 319 – 339, 1984.

Pierce, C. D. and Moin, P. Progress-variable approach for large-eddy simulation of non-premixed turbulent combustion, **Journal of Fluid Mechanics**, vol. 504, p. 73–97, 2004.

Pitsch, H., Chen, M., and Peters, N. Unsteady flamelet modeling of turbulent hydrogen-air diffusion flames, **Symposium (International) on Combustion**, vol. 27(1), p. 1057 – 1064, 1998.

Pitsch, H., Riesmeier, E., and Peters, N. Unsteady Flamelet Modeling of Soot Formation in Turbulent Diffusion Flames, **Combustion Science and Technology**, vol. 158(1), p. 389–406, 2000.

Poinsot, T. and Veynante, D. **Theoretical and numerical combustion**. RT Edwards Incorporated, 2005.

Pope, C. J. and Howard, J. B. Simultaneous Particle and Molecule Modeling (SPAMM): An Approach for Combining Sectional Aerosol Equations and Elementary Gas-Phase Reactions, **Aerosol Science and Technology**, vol. 27(1), p. 73–94, 1997.

Prüfert, U., Hartl, S., Hunger, F., Messig, D., Eiermann, M., and Hasse, C. A Constrained Control Approach for the Automated Choice of an Optimal Progress Variable for Chemistry Tabulation, **Flow, Turbulence and Combustion**, vol. 94(3), p. 593–617, 2015.

Raj, A., Celnik, M., Shirley, R., Sander, M., Patterson, R., West, R., and Kraft, M. A statistical approach to develop a detailed soot growth model using {PAH} characteristics, **Combustion and Flame**, vol. 156(4), p. 896 – 913, 2009.

Santoro, R., Semerjian, H., and Dobbins, R. Soot particle measurements in diffusion flames, **Combustion and Flame**, vol. 51, p. 203 – 218, 1983.

Santoro, R. J., Yeh, T. T., Horvath, J. J., and Semerjian, H. G. The Transport and Growth of Soot Particles in Laminar Diffusion Flames, **Combustion Science and Technology**, vol. 53(2-3), p. 89–115, 1987.

Sivathanu, Y. and Gore, J. Coupled radiation and soot kinetics calculations in laminar acetylene/air diffusion flames, **Combustion and Flame**, vol. 97(2), p. 161 – 172, 1994.

Skjøth-Rasmussen, M., Glarborg, P., Østberg, M., Johannessen, J., Livbjerg, H., Jensen, A., and Christensen, T. Formation of polycyclic aromatic hydrocarbons and soot in fuel-rich oxidation of methane in a laminar flow reactor, **Combustion and Flame**, vol. 136, p. 91–128, 2004.

Smith, G., Frenklach, D. G. M., Moriarty, N., Eiteneer, B., Goldenberg, M., Bowman, C., Hanson, R., Song, S., Gardiner, W., Lissianski, V., and Qin, Z. **GRI-Mech 3.0**, 2000.

Smooke, M. and Giovangigli, V. Formulation of the premixed and nonpremixed test problems, **Lect. Notes Phys.**, vol. 384, p. 1–28, 1991.

Smooke, M., McEnally, C., Pfefferle, L., Hall, R., and Colket, M. Computational and experimental study of soot formation in a coflow, laminar diffusion flame, **Combustion and Flame**, vol. 117(1–2), p. 117 – 139, 1999.

Smooke, M., Puri, I., and Seshadri, K. A comparison between numerical calculations and experimental measurements of the structure of a counterflow diffusion flame burning diluted methane in diluted air, **Symposium (International) on Combustion**, vol. 21(1), p. 1783 – 1792, 1988.

Steward, C., Syed, K., and Moss, J. Modelling Soot Formation in Non-premixed Kerosine–Air Flames, **Combustion Science and Technology**, vol. 75(4-6), p. 211–226, 1991.

Strik, J. **Flamelet Generated Manifolds to Model Auto-ignition, Combustion and Pollutants in HDDI Diesel Engines**. Master's thesis, Eindhoven University of Technology (TU/e), The Netherlands, 2010.

TNF. **International Workshop on Measurement and Computation of Turbulent Nonpremixed Flames (TNF): radiation models**. `http://www.sandia.gov/TNF/radiation.html`, 2016.

Turns, S. R. **An introduction to combustion, 2000**. McGraw-Hill, New York, 2000.

van Oijen, J. **Flamelet-generated manifolds: development and application to premixed laminar flames**. Technische Universiteit Eindhoven, 2002.

van Oijen, J. and de Goey, L. Modelling of premixed laminar flames using flamelet-generated manifolds, **Combustion Science and Technology**, vol. 161, p. 113–137, 2000.

van Oijen, J., Donini, A., Bastiaans, R., ten Thije Boonkkamp, J., and de Goey, L. State-of-the-art in premixed combustion modeling using flamelet generated manifolds, **Progress in Energy and Combustion Science**, vol. 57, p. 30 – 74, 2016.

van Oijen, J., Lammers, F., and de Goey, L. Modeling of complex premixed burner systems by using flamelet-generated manifolds, **Combustion and Flame**, vol. 127(3), p. 2124 – 2134, 2001.

van Oijen, J. A. and de Goey, L. P. H. Modelling of premixed counterflow flames using the flamelet-generated manifold method, **Combustion Theory and Modelling**, vol. 6(3), p. 463–478, 2002.

van Oijen, J. A. and de Goey, L. P. H. A numerical study of confined triple flames using a flamelet-generated manifold, **Combustion Theory and Modelling**, vol. 8(1), p. 141–163, 2004.

Vandsburger, U., Kennedy, I., and Glassman, I. Sooting Counterflow Diffusion Flames with Varying Oxygen Index, **Combustion Science and Technology**, vol. 39(1-6), p. 263–285, 1984.

Verhoeven, L., Ramaekers, W., van Oijen, J., and de Goey, L. Modeling non-premixed laminar co-flow flames using flamelet-generated manifolds, **Combustion and Flame**, vol. 159(1), p. 230 – 241, 2012.

Verhoeven, L. M. **Radical tar removal : numerical modeling of tar conversion in a partial combustion reactor.** PhD thesis, Eindhoven Technological University, 2011.

Violi, A. Modeling of soot particle inception in aromatic and aliphatic premixed flames, **Combustion and Flame**, vol. 139(4), p. 279 – 287, 2004.

Wang, H. and Laskin, A. **A comprehensive kinetic model of ethylene and acetylene oxidation at high temperatures**, 1999.

Wang, H., You, X., Joshi, A. V., Davis, S. G., Laskin, A., Egolfopoulos, F., and Law, C. K. **USC Mech Version II. High-Temperature Combustion Reaction Model of H2/CO/C1-C4 Compounds**, 2007.

Wang, Y., Raj, A., and Chung, S. H. Soot modeling of counterflow diffusion flames of ethylene-based binary mixture fuels, **Combustion and Flame**, vol. 162(3), p. 586 – 596, 2015.

Wilke, C. A viscosity equation for gas mixtures, **The journal of chemical physics**, vol. 18(4), p. 517–519, 1950.

Williams, F. A. **Combustion Theory (Combustion Science and Engineering Series)**. The Benjamin/Cummings Publishing Company, Inc., 1985.

Zhang, Q., Guo, H., Liu, F., Smallwood, G., and Thomson, M. Modeling of soot aggregate formation and size distribution in a laminar ethylene/air coflow diffusion flame with detailed PAH chemistry and an advanced sectional aerosol dynamics model, **Proceedings of the Combustion Institute**, vol. 32(1), p. 761 – 768, 2009.

Zhang, Q., Guo, H., Liu, F., Smallwood, G. J., and Thomson, M. J. Implementation of an advanced fixed sectional aerosol dynamics model with soot aggregate formation in a laminar methane/air coflow diffusion flame, **Combust. Theor. Model.**, vol. 12(4), p. 621–641, 2008.

APPENDIX A – Modeling Radiation: Optically Thin Approximation (OTA)

The radiant heat losses are modelled by using the grey-gas approximation, i.e., there is no dependence on the wave number, and the optical thin limit, i.e., the medium does not scatter nor absorb radiation. Then, the heat source in the energy conservation equation because of the radiant heat losses Smooke et al., 1999, is :

$$\dot{q}_R''' = \nabla \cdot \mathbf{q_{rad}} = -4\sigma\kappa(T^4 - T_{sur}^4) - C f_v T^5, \tag{A.1}$$

$$\kappa = \sum p_i \kappa_i, \tag{A.2}$$

where σ is the Stefan-Boltzmann constant (5.669×10^{-8} $W\ m^{-2}K^{-4}$), and T_{sur} is the ambient temperature. κ denotes the Planck mean absorption coefficient of the mixture (m^{-1}), and p_i and κ_i are respectively the partial pressure (atm) and Planck mean absorption coefficient of species i ($atm^{-1}m^{-1}$). The participant gas species are H_2O, CO_2, CO and CH_4. The Plank mean absorption coefficient for H_2O and CO_2 are given in Chen et al., 1993, and for CO and CH_4 are given in TNF, 2016. The constant $C = 4.243 \times 10^{-4}$ ($W\ m^{-3}K^{-5}$) is from Smooke et al., 1999.

For the Plank mean absorption coefficient for H_2O and CO_2:

$$\log 10\left(\frac{\kappa_i}{\kappa_{ref}}\right) = \sum_{n=0}^{6} a_{i,n}\left(\frac{T}{300}\right)^n \tag{A.3}$$

with $\kappa_{ref} = 1.0$ $(matm)^{-1}$, and the following $a_{i,n}$ coefficients:

Table A.1: Polynomial coefficients for H_2O and CO_2

a_n	H_2O	CO_2
a_0	0.22317E1	0.38041E1
a_1	-0.15829E1	-0.27808E1
a_2	0.1329601E1	0.11672E1
a_3	-0.50707E0	-0.28491E0
a_4	0.93334E-1	0.38163E-1
a_5	-0.83108E-2	-0.26292E-2
a_6	0.28834E-3	0.73662E-4

For the Plank mean absorption coefficient for CO and CH_4:

$$\kappa_i = \sum_{n=0}^{4} b_{i,n} T^n \tag{A.4}$$

with the following $b_{i,n}$ coefficients:

Table A.2: Polynomial coefficients for CH_4 and CO

b_n	CH_4	CO, $T <= 750K$	CO, $T > 750K$
b_0	6.6334E0	4.7869E0	1.009E1
b_1	-3.5686E-3	-6.953E-2	-1.183E-2
b_2	1.6682E-8	2.95775E-4	4.7753E-6
b_3	2.5611E-10	-4.25732E-7	-5.87209E-10
b_4	-2.6558E-14	2.02894E-10	-2.5334E-14

APPENDIX B – Kinetic Mechanism influence in soot modeling:

For the target flame it has been used a variety of kinetic mechanism for predicting the gas-phase species. A comparison of kinetic mechanisms and its influence in soot prediction is done. Seven kinetic mechanisms were tested and are presented in the Table B.1. Simulations were done for ethylene counterflow flames at 20 $1/s$ and 100 $1/s$, for coupled and adiabatic case, using the soot model of Liu et al., 2004. Only the 20 $1/s$ are shown here since the 100 $1/s$ have the same behaviour the the 20 $1/s$, but lower values. The values for the GRI3.0 reduced (no NOx reactions) are not shown here since it gave the same results as the original mechanism.

Table B.1: Kinetic mechanisms

Mechanism	size (sp/reac)	obs.
Appel et al., 2000 (abf)	101/544	developed for ethane, ethylene, and acetylene
Blanquart et al., 2009 (blanquart)	148/928	hydrocarbon fuels from methane to iso-octane
GRI Mech v3 [Smith et al., 2000] (gri3.0)	53/325	developed natural gas combustion
GRI Mech v3 reduced	36/219	removed all NOx formation
USC Mech VII [Wang et al., 2007] (USC II)	111/784	H2/CO/C1-C4 Compounds
Wang and Laskin, 1999 (WL)	75/529	ethylene and acetylene combustion
Luo et al., 2012 (sk/WL)	32/206	skeletal based from Wang and Laskin Mech

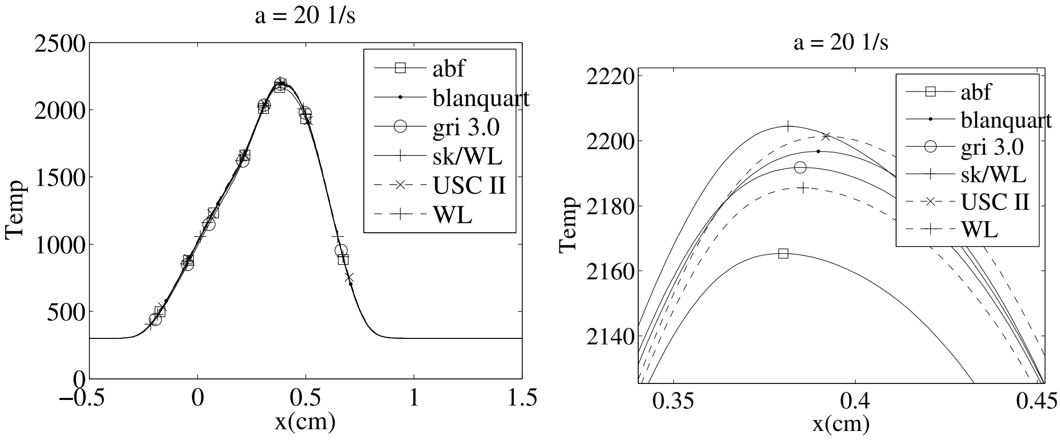

Figure B.1: Temperature profile; zoom at the peak

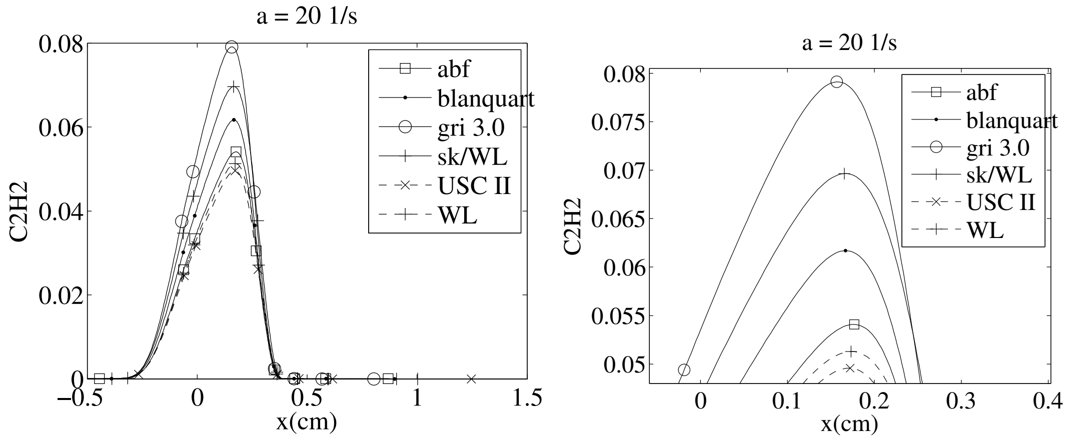

Figure B.2: C2H2 profile; zoom at the peak

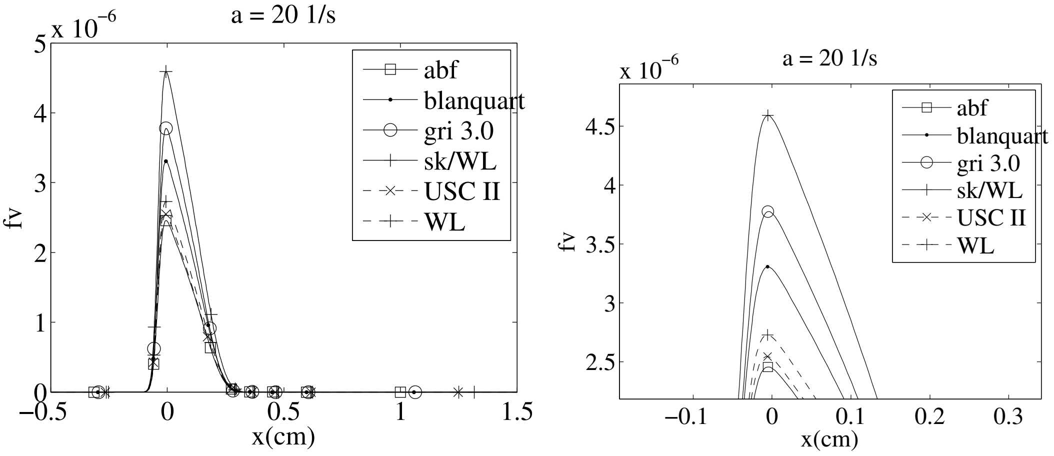

Figure B.3: f_v profile; zoom at the peak

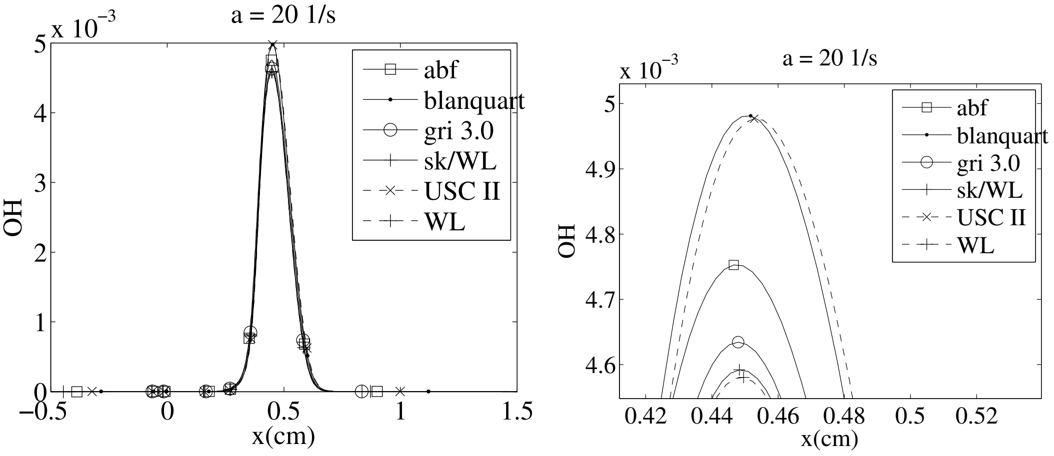

Figure B.4: OH profile; zoom at the peak

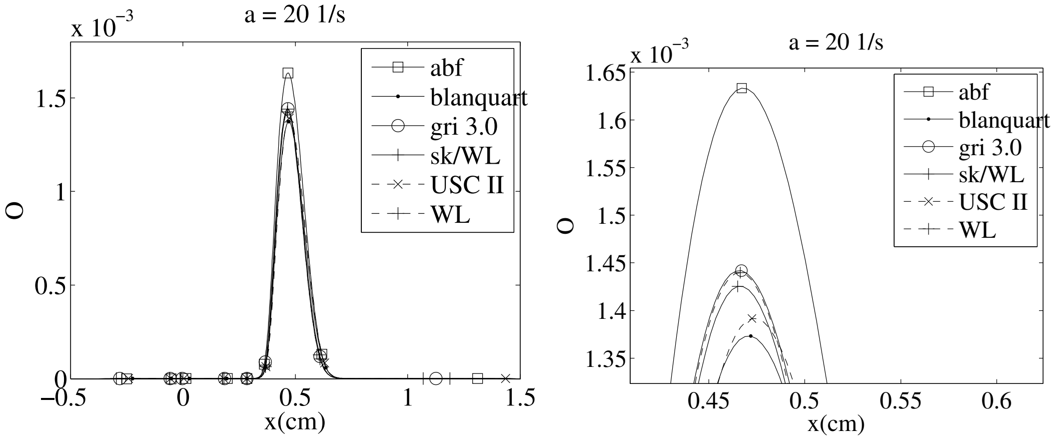

Figure B.5: O profile; zoom at the peak

APPENDIX C – Soot model influencies in soot predictions

In this section a comparison between two set of parameters for soot reactions within the same soot model is done. The first set of parameters is the one used in the present thesis, from Liu et al., 2002, and the second is from Liu et al., 2003. Liu et al., 2003 proposed a modified version of the two-equation model of Leung, with different set of reaction rate constants and a special attention on the oxidation rates. This set was developed to fit the experiments of Santoro et al., 1983 for atmospheric non-smoking and smoking ethylene/air coflow diffusion flames. The comparison between both soot model parameters in presented in the Table C.1.

Table C.1: Comparison of Soot models; only the differences are shown.

Reaction	Liu et al., 2002	Liu et al., 2003
Thermop. vel. const.	$C_i = 0.65$	$C_i = 0.67$
Nucleation	$k_1 = 1.0 \times 10^3 \exp(-16,103/T)$	$k_1 = 1.7 \exp(-7,548/T)$
Surf. Growth	$k_2 = 1.75 \times 10^3 \exp(-10,064/T)$	$k_2 = 6 \exp(-6,038/T)$
	$f(S) = \sqrt{S}$	$f(S) = S$
Oxid. by O_2	R_3	$R_3 f_{O_2}$ $f_{O_2} = (1 + \exp[-(T - 1,650)/80])^{-1}$
Oxid. by OH	R_4	$R_4 f_{OH}$ $f_{OH} = (1 + \exp[-(T - 1,675)/70])^{-1}, T \geq 1675K$ $f_{OH} = (1 + \exp[-(T - 1,675)/50])^{-1}, 1600K < T < 1675K$ $f_{OH} = 0.1824 \times (1 + \exp[-(T - 1,600)/85])^{-1}, T \leq 1600K$
Oxid. by O	R_5	Not considered

The comparison between the two set of parameters is done for the exact same conditions presented in the Chapter 4 for simulation a non-smoking ethylene coflow flame. The comparison is shown only for the soot volume integrated along the height of the burner in Figure C.1.

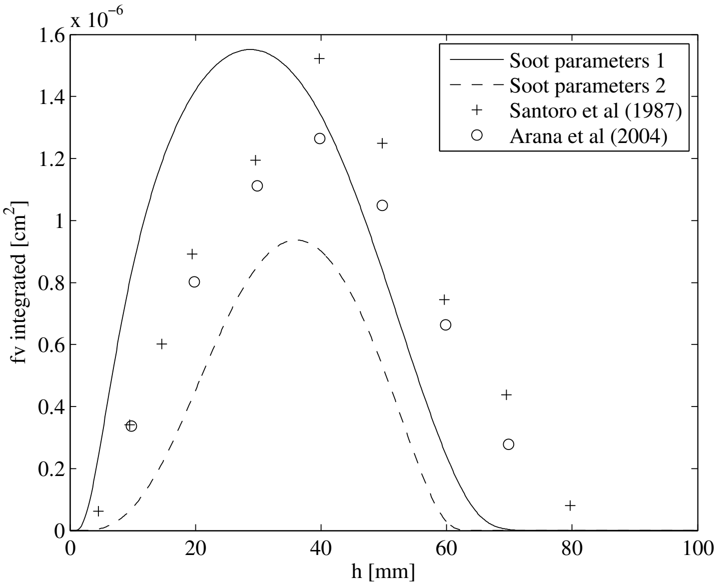

Figure C.1: f_v integrated comparison; Symbols: experimental data Santoro et al., 1987 and Arana et al., 2004; solid line: present simulation with Soot parameter 1 - Liu et al., 2002 , parameter 2 - Liu et al., 2003

As it can be seen in the Figure C.1 the choice of the soot reactions parameters can have a important impact in the soot predictions. While the first set of parameters reach the same peak of soot amount as the experiment, but at a lower height, the second set of parameter did neither reach the same amount of soot not the maximum soot prediction position, even that that set was fitted to do so. The maximum soot volume fraction were $f_{v,max} = 7.1$ ppm and $f_{v,max} = 5.3$ ppm, for Soot parameters 1 and 2, respectively.